The nature of the dissociation dynamics of hydrocarbon radicals

Habilitation Thesis

Author(s):
Bach, Andreas

Publication date:
2010

Permanent link:
https://doi.org/10.3929/ethz-a-007207584

The Nature of the Dissociation Dynamics of Hydrocarbon Radicals

Habilitationsschrift

Dr. Andreas Bach

Laboratorium für Organische Chemie
ETH Zürich

April 19, 2010

A part of this work is based on the following publications:

1. L. Castiglioni, A. Bach, and P. Chen
   Probing centrifugal barriers in unimolecular dissociation of the allyl radical
   J. Phys. Chem. A **109**, 962(2005)

2. A. Bach, J. M. Hostettler and P. Chen
   Quasiperiodic trajectories in the unimolecular dissociation of ethyl radicals by time-frequency analysis
   J. Chem. Phys. **123**, 021101(2005)

3. L. Castiglioni, A. Bach and P. Chen
   Spectroscopy and dynamics of $\widetilde{A}$ $[^2B_1]$ allyl radical
   Phys. Chem. Chem. Phys. **8**, 2591(2006)

4. A. Bach, J. M. Hostettler, and P. Chen
   Nonstatistical effects in the dissociation of ethyl radical: Finding order in chaos
   J. Chem. Phys. **125**, 024304(2006)

5. M. Gasser, A. Bach and P. Chen
   Photodissociation dynamics of 2-methylallyl radical
   Phys. Chem. Chem. Phys. **10**, 1133(2008)

6. J. M. Hostettler, A. Bach, and P. Chen
   Adiabatic and nonadiabatic dissociation of ethyl radical
   J. Chem. Phys. **130**, 034303(2009)

7. J. M. Hostettler, L. Castiglioni, A. Bach and P. Chen
   Photochemical deactivation pathways of the $\widetilde{A}$-state allyl radical
   Phys. Chem. Chem. Phys. **11**, 8262(2009)

8. M. Gasser, A. M. Schulenburg, P. M. Dietiker, A. Bach, F. Merkt, and P. Chen
   Single-photon and resonance-enhanced multiphoton threshold ionization of the allyl radical
   J. Chem. Phys. **131**, 014304(2009)

9. M. Gasser, J. A. Frey, J. M. Hostettler, A. Bach and P. Chen
   Vibronic structure of the 3s and 3p Rydberg states of the allyl radical J. Phys. Chem. A **114**, 4704(2010)

10. M. Gasser, J. A. Frey, J. M. Hostettler, A. Bach
    Probing for non-statistical effects in dissociation of the 1-methylallyl radical
    to be submitted

Contents

Chapter 1

Introduction

Understanding and predicting the motions of the atoms in molecules during chemical transformations lies at the hart of chemistry. The transition state is a special transient molecular structure corresponding to the highest energy point along the minimum energy pathway connecting reactants and products. Chemists have relied on this idea to classify different reaction types and predict the products and kinetics of chemical reactions since Eyring introduced the concept of a transition state in 1935.

More recently, a growing number of convincing experimental and theoretical studies on chemical reactions involving different reactive intermediates have shown that reaction mechanisms and pathways that bypass the conventional saddle-point transition state on the potential energy surface can occur in both thermal and photo-induced chemical reactions. In those type of reactions with dynamical non-statistical effects, the widely used statistical models of kinetics, most notably transition-state theory and its microcanonical analogue Rice-Rampsperger-Kassel-Marcus theory, are inadequate to describe the experimentally observed behavior.

Despite remarkable recent progress in the theory of unimolecular reactions, the underlying physics and origin of those dynamical non-statistical effects are often not fully understood. Modern molecular dynamics simulations do provide insight into the dynamics of a chemical reaction at an atomistic level, but the analysis and visualization of the results often challenges existing conventional mathematical methods or quantitative metrics when applied to dynamical systems of higher dimensionality. Experimentally, the challenge is to prepare a well defined ensemble of molecules and measure the kinetics and detect the products after initiating the reaction.

In this Habilitationsschrift, I will discuss the nature of the dissociation dynamics of small hydrocarbon radicals in the gas-phase based on a combined experimental and computational study of photo-induced hydrogen abstraction. Small hydrocarbon radicals of fundamental importance in combustion are an ideal test-bed to study non-statistical effects in unimolecular decomposition, as they can be readily prepared in large number densities under collision-free conditions, often have several low-lying electronically excited states allowing to use photodissociation experiments as a means to probe the dissociation dynamics, and are still amendable to computational work at the highest level of theory.

Figure 1.1 shows a graphical representation of the different processes and pathways encountered in this study of the nature of the dissociation dynamics of small hydrocarbon radicals $RH^{\bullet}$ to eventually form a closed shell ground state fragment R or excited state fragment R^* and hydrogen following initial photoexcitation. In a summary of the computational and experimen-

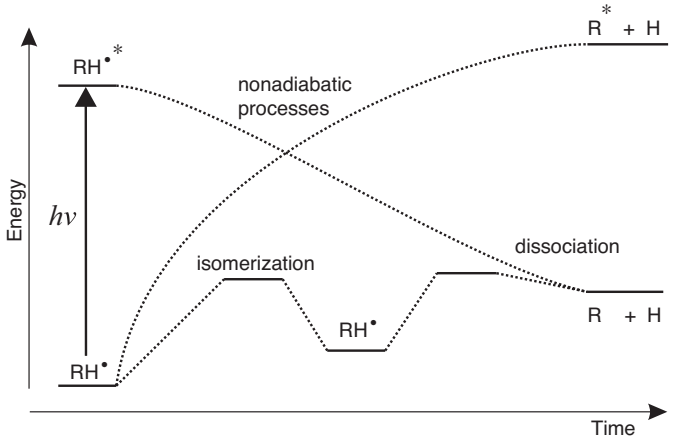

Figure 1.1: Schematic energy diagram showing the different processes and pathways relevant in our photodissociation studies of hydrocarbon radicals $RH^{\bullet}$.

tal results of the dissociation dynamics of both the ethyl radical (C_2H_5) in Chapter 3, and the allyl radical (C_3H_5) in Chapter 4 of this work, both statistical and non-statistical effects play an important role encountered on several timescales, from ultrafast electronically nonadiabatic processes on a femtosecond timescale, photo-induced isomerization on a sub-picosecond timescale, to dissociation on timescales ranging from femto- to microseconds.

The experimental tools and methods used to study the photodissociation dynamics and the supporting spectroscopic characterization of the hydrocarbon radicals are mostly well established and I will describe the experimental apparatus in Chapter 5 together with unpublished results on the photodissociation dynamics of the 1-methylallyl radical. Most of the existing methods

to analyze the results from the large scale direct molecular dynamics simulations, however, were insufficient to gain insight into the non-statistical effects encountered in this work. We have developed new methods described in Chapter 2 based on the decomposition of classical trajectories in the time-frequency domain using wavelets to not only visualize these effects, but also constructed and applied a new time-dependent scalar metric to rapidly discover and quantify the extent of nonergodic behavior in the ethyl radical.

In Chapter 6, I will discuss and compare the nature of the dissociation dynamics of the ethyl radical that shows several different kinds of *non-statistical effects* in unimolecular decomposition to that of the allyl radical, which in stark contrast displays *statistical behavior*. Classifying these non-statistical effects reveals that the experimentally observed unusually long-lived ethyl radicals with lifetimes far exceeding statistical predictions can be explained by dynamical trappings in the *reactant phase space* region that only affect the dissociation rate, but not the energy disposal in the photoproducts, even though the radicals finally dissociate by passing close to the transition state connecting reactant and products. A comparison of the dissociation dynamics of the ethyl radical and recent experimental results of substituted allyl radicals gives insight into possible structural motifs in hydrocarbon radicals that may promote non-statistical behavior in dissociation.

Chapter 2

Methods

Ab initio and DFT Methods

Computational studies of the photodissociation dynamics of small hydrocarbon radicals in the gas-phase complements our experiments and allows to obtain a comprehensive picture of the mechanisms governing the dissociation dynamics of small hydrocarbon radicals following photoexcitation.

Our method of choice is direct dynamics (semi)classical trajectory calculations using either *ab initio* or density functional methods with atom centered Gaussian basis sets to evaluate potential energies, gradients and non-adiabatic couplings "on the fly". These direct dynamics calculations for small hydrocarbon radicals such as allyl or ethyl requires a level of theory that accurately describes the global potential energy surfaces at the lowest possible computational cost. The results presented in Chapter 3 reveal that the observables obtained from the (semi)classical trajectory calculations sensitively depend on the choice and quality of the potential energy surfaces (PES). In this section, we summarize the methods used to evaluate the quality of the PES for ethyl radical, C_3H_5, and compare several single- and multi-reference wavefunction methods to density functional methods. We also briefly describe the sampling method used to generate an appropriate ensemble for the (semi)classical trajectory calculations.

Highly energized ethyl radicals produced following photoexcitation and subsequent ultrafast electronically nonadiabatic decay sample nuclear configurations during the trajectories that are far away from the ethyl equilibrium geometry even prior to dissociation. It is therefore important to not only include the relevant stationary points on the global potential energy surface

for ethyl radical dissociation, but to also include highly distorted nuclear geometries for energized ethyl radical to evaluate the quality of the PES. To select a balanced test set in nuclear configuration space, we ran 449 classical trajectories[1] at the UHF/6-31G* level of theory and sequentially selected 67 nuclear configurations of the ethyl radical most frequently visited by the classical trajectories, but far from existing data points in the data set using the $h(k)$ method reported by Collins.[2]

Figure 2.1 shows a comparison of the absolute error of the different potential energy surfaces obtained at different levels of theory for vibrationally excited ethyl radicals relative to the CCSD(T)/CBS reference calculations for the selected 67 nuclear configurations in dynamically important regions of configuration space. We compare the performance of multi-reference wavefunction methods with (MRCI and MR-AQCC) and without (MCSCF) dynamic electron correlation to a selected density functional method, HCTH147, which is based on a exchange-correlation density functional with a flexible functional form[3,4] parameterized to absorb some of the deficiencies of the small atom centered basis set.

The HCTH147 density functional[3,4] even without specific reaction parameters[1] shows very small energy differences with a near Gaussian error distribution centered at ∼0 kcal/mol compared to the "gold standard" CCSD(T)/CBS and has a mean absolute error of only 0.01 kcal/mol or 1.57 kcal/mol RMS, respectively (Fig. 2.1a). Compared to HCTH147, both MCSCF and MRCI have error distributions centered at a large positive energy difference that are clearly skewed, indicating that the anharmonicities of these potentials are rather different. Even though MRCI gives excellent reaction energies and vertical excitation energies, the part of the potential energy surface describing highly energized ground state ethyl radicals is poorly described, as shown in Fig. 2.1d. Note that even with a very large basis set [Fig. 2.1(f)], MRCI still has a skewed distribution with absolute errors as large as 20 kcal/mol. To properly describe the potential energy surface for nuclear configurations that are essential to describe the regular type intramolecular motions that give rise to the non-RRKM dynamics reported in Chapter 3, higher excitations than doubles must be included, see Fig. 2.1(e,f,g,h,i). Unfortunately, *ab initio* molecular dynamics simulating nonadiabatic photodissociation processes with wave function methods that include at least triples excitation and a large basis set are currently not feasible. Moreover, using the same calibrated functional for the nonadiabatic dynamics combined with

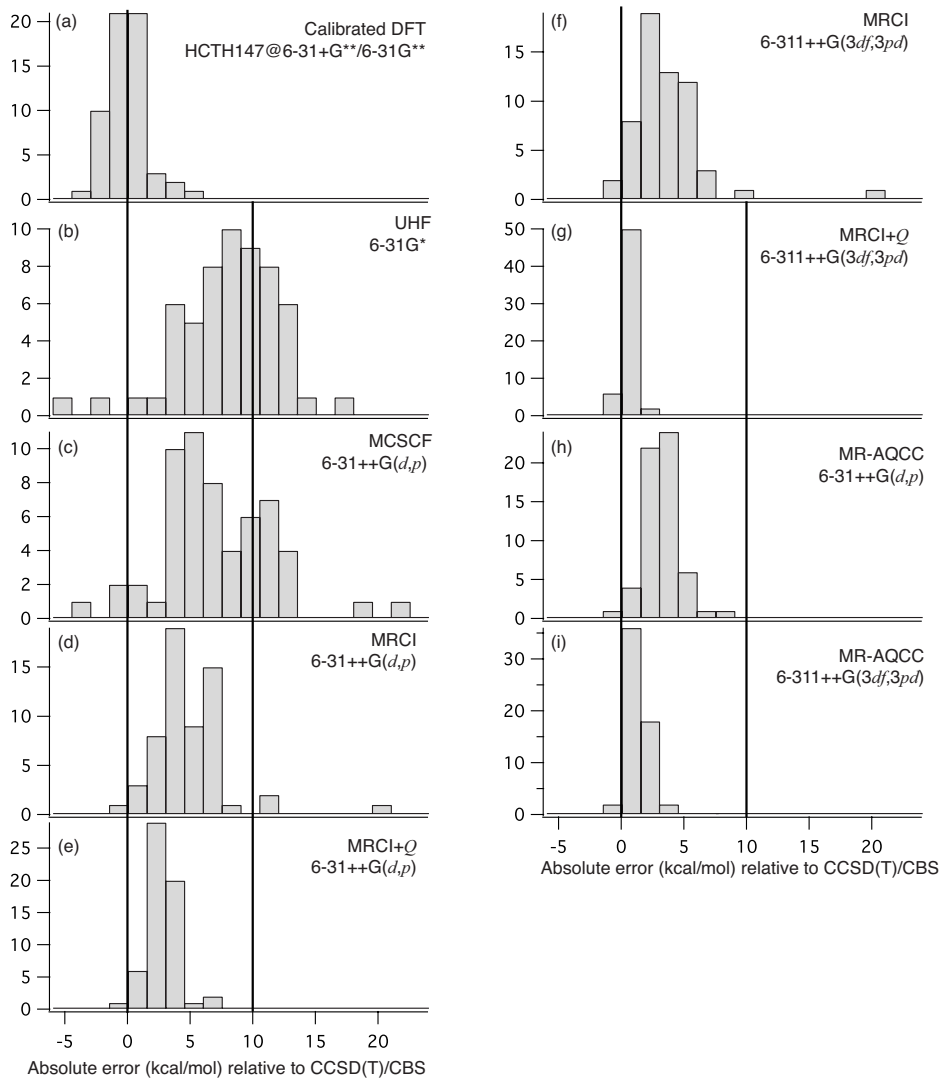

Figure 2.1: Histogram of the absolute error of the different potential energy surfaces for vibrationally excited ethyl radicals relative to the CCSD(T)/CBS reference calculations. Note that the skewed distributions for MR-CISD arise from neglecting higher excitations. These are only included in the CCSD(T) reference calculations, MRCI+Q [Davidson] (e,g) and MR-AQCC (h,i).

time-dependent density functional theory (TDDFT) is also questionable as recently pointed out by Martínez and co-workers,[5] as there are a number of qualitative deficiencies which need to be addressed before TDDFT can be applied routinely to photochemical problems.

We used direct *ab initio* molecular dynamics using the trajectory surface hopping method with Tully's fewest switches[6] to simulate the nonadiabatic photodissociation dynamics of the ethyl radical at the multireference configuration interaction with singles and doubles level of theory as discussed in the next Chapter. For the allyl radical, we explored the photochemical deactivation pathways using the state averaged multiconfiguration self-consistent field (SA–MCSCF) level of theory with different surface hopping schemes,[7–9] see Chapter 4 and Ref. 10. The details of the direct dynamics trajectory calculations are described elsewhere[1,10–12] and we only give a short summary. We generated a microcanonical ensemble of initial states including the zero-point energy and no rotational angular momentum using quasiclassical normal-mode sampling.[13] The relationship between displacements from the equilibrium geometry and the potential energy was treated with a fifth-order local polynomial fit to the potential energy surface.[14] An iterative scaling procedure then removed any vibrational angular momentum and corrected for residual anharmonicity.[13]

Time-frequency Analysis

Most of the existing conventional mathematical methods or quantitative metrics to analyze the results from the large scale direct molecular dynamics simulations are problematic when applied to dynamical systems of higher dimensionality, such as for the ethyl radical where phase space is 42 dimensional. In this section, we describe new methods based on the decomposition of classical trajectories in the time-frequency domain using wavelets.

Local frequency analysis using fast Fourier transforms of sequential segments of trajectories is a well established technique to study and analyze non-statistical behavior and dynamical bottlenecks in multimode systems.[15] Wiggins and co-workers[16] later used wavelet analysis to decompose a trajectory in the time-frequency domain and introduced the concept of an instantaneous frequency extracted numerically from the maximum modulus of the continuous wavelet transform of a trajectory for a three degrees-of-freedom Hamiltonian system. In Chapter 3 and Ref. 11, we report direct dynamics

classical trajectory calculations of the ethyl radical unimolecular dissociation and analyze the classical trajectories using a wavelet based time-frequency analysis to understand the non-statistical behavior in dissociation.

Briefly, each Cartesian component of the reduced-mass-weighted coordinates of a trajectory gives a time series x_n with N time steps δt=0.1fs. We used the Morlet wavelet[17]

$$\Psi_0(\eta) = \pi^{-1/4} e^{i\omega_0 \eta} e^{-\eta^2/2} \tag{2.1}$$

consisting of a plane wave modulated by a Gaussian, where η is a dimensionless time parameter and $\omega_0 = 6$ the non-dimensional frequency as a wavelet basis. The continuous wavelet transform of the discrete time series x_n is defined by the convolution of x_n with a scaled and translated version of $\Psi_0(\eta)$,

$$W_n(s) = \sum_{n'=0}^{N-1} x'_n \Psi^* \left[\frac{(n'-n)\delta t)}{s} \right], \tag{2.2}$$

where s is the wavelet scale which is inversely proportional to the frequency and n a localized time index. This requires N convolutions for each scale s. It is considerably faster to do all N convolutions simultaneously for a given s in Fourier space using an appropriately normalized wavelet Ψ. The wavelet transform is then the inverse Fourier transform of the product,

$$W_n(s) = \sum_{k=0}^{N-1} \hat{x}_k \hat{\Psi}^*(s\omega_k) e^{i\omega_k n \delta t}, \tag{2.3}$$

where the angular frequency is defined as

$$\omega_k = \begin{cases} \frac{2\pi k}{N\delta t}, & k \leqslant \frac{N}{2} \\ -\frac{2\pi k}{N\delta t}, & k > \frac{N}{2} \end{cases} \tag{2.4}$$

and where $\hat{x}_k$ is the discrete Fourier transform of the time series x_n,

$$\hat{x}_k = \frac{1}{N} \sum_{n=0}^{N-1} x_n e^{-2\pi i k n/N} \tag{2.5}$$

with $k = 0 \ldots N-1$ as the frequency index. To ensure that the wavelet transforms (2.3) at each scale s are directly comparable to each other and to the transforms of the other time series, the wavelet at each scale s is normalized to have unit energy

$$\hat{\Psi}(s\omega_k) = \sqrt{\frac{2\pi s}{\delta t}} \hat{\Psi}_0(s\omega_k), \tag{2.6}$$

which results in

$$\hat{\Psi}_0(s\omega) = \pi^{1/4} H(\omega) e^{-(s\omega-\omega_0)^2/2} \tag{2.7}$$

for the Morlet wavelet (2.1), where $H(\omega)$ is the Heaviside step function. We

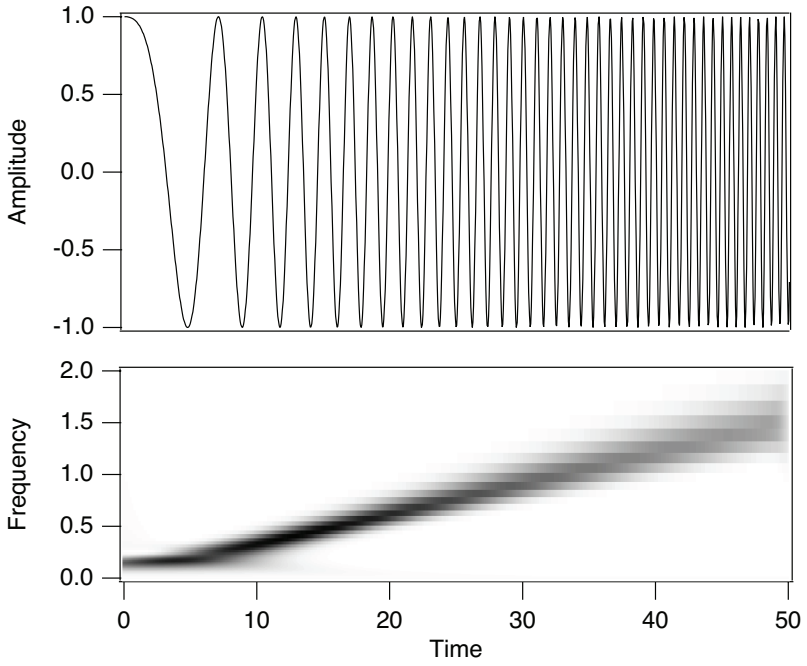

Figure 2.2: Example spectrogram $P_n(s)$ resulting from a time series described by a cosine with a linear frequency chirp.

then calculated the scale-normalized wavelet power

$$P_n(s) = \frac{1}{s}|W_n(s)|^2 \tag{2.8}$$

for each time series formed by the Cartesian components of the reduced-mass-weighted coordinates of a trajectory. The spectrogram for a single degree-of-freedom is then represented by an image plot of $P_n(s)$. Fig. 2.2 shows an example of a spectrogram obtained from the simple analytical function $f(t) = \cos(nt + mt^2)$. The absolute maximum of $P_n(s)$ in frequency at a given time t corresponds to the instantaneous frequency. Chandre *et al.*[18] showed that the relevant information is contained in the ridges of the landscape formed by the magnitude of the coefficients of the time-frequency decomposition. These ridges or instantaneous frequency curves correspond to time-frequency energy localization.

Figure 2.3 shows an example of such a spectrogram obtained form a single coordinate of a *ab initio* direct dynamics trajectory of ethyl radical.[1,11] This

spectrogram in the form of a contour plot analogous to a topographic map, shows a landscape of ridges or instantaneous frequency curves corresponding to time-frequency energy localization. Multiple, short-lived, low-intensity ridges in a time-frequency plot characterize a strongly chaotic trajectory. A quasiperiodic trajectory has typically only one high-intensity ridge with a near-constant frequency persisting for an extended stretch of time, and only small modulations from oscillations about the expected frequency. The anal-

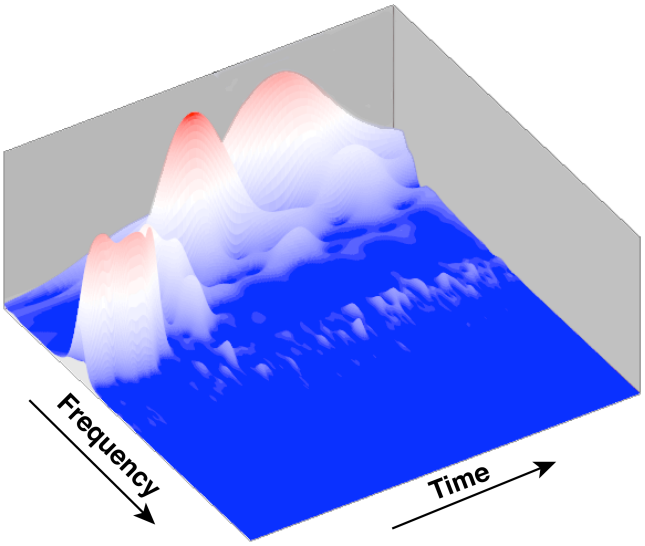

Figure 2.3: Example spectrogram $P_n(s)$ for a single degree-of-freedom of a quasiclassical trajectory of ethyl radical (see Chapter 3).

ysis of ensembles of classical trajectories requires a robust, scalable metric which can efficiently identify those trajectories, or portions of trajectories, which display chemically interesting dynamical behavior. We developed a time-dependent scalar metric, the instantaneous wavelet-based orbital complexity, which can be used to parse rapidly, and automatically, large ensembles of trajectories and correlates with the conventionally accepted, but computationally more difficult, Lyapunov exponents.[11]

The Normalized Instantaneous Orbital Complexity

Qualitatively, the orbital complexity is the number of frequency components needed to capture a set fraction k, usually 90%, of the spectral power in a spectrogram. We define the normalized instantaneous orbital complexity with a threshold k at time step n of a trajectory from the wavelet transform

of each Cartesian component x_m of the reduced-mass-weighted coordinates of a trajectory. The total scale-normalized wavelet power at time step n for one coordinate m of a trajectory is the sum of the scale-normalized wavelet power (2.8) over all S scales s_j

$$P_n^{total} = \sum_{j=1}^{S} P_n(s_j) \tag{2.9}$$

We then sort the array $P_n(s_j)$ according to decreasing P_n and determine the number J_a of scales $s_{j'}$, which are required to satisfy

$$\sum_{j'=1}^{J_a} P_n^{sorted}(s_{j'}) \leqslant k P_n^{total} \tag{2.10}$$

at time step n for one coordinate m. The instantaneous normalized orbital complexity $n(k)$ at time step n is then given by the sum of J_m over all M coordinates

$$n(k) = \frac{1}{MS} \sum_{m=1}^{M} J_m \tag{2.11}$$

This equation is the wavelet-based analog of the orbital complexity based on short time Fourier transforms introduced by Siopis *et al.*[19] We used a threshold $k = 0.9$ as suggested by Siopis. The calculated normalized instantaneous orbital complexities for all trajectories in the ensemble depend only weakly on the choice of the wavelet in the transform, at least for the trajectories described in Chapt. 3. The Morlet wavelet with a non-dimensional time parameter ω_0 between 2 and 6 and the real-valued Mexican hat (derivative of a Gaussian) wavelet gave nearly identical results.

Lyapunov Exponents

Lyapunov exponents measure the asymptotic average exponential rate of divergence of nearby trajectories in phase space as time goes to infinity.[20] In an N degree-of-freedom Hamiltonian system, there are $2N$ Lyapunov exponents that appear in matching positive/negative pairs with at least $2K$ zero exponents for K independent constants of motion. A system with at least one positive Lyapunov exponent is said to be chaotic as the exponential divergence implies that the predictive ability of a trajectory shows extreme sensitivity to the level of initial information. As an asymptotic quantity, the ordinary Lyapunov exponents are clearly unsuitable to study the transient

dynamics of unimolecular dissociation of the ethyl radical. An alternative tool is given by local Lyapunov exponents, which characterize the average exponential instability of a trajectory segment over a finite time interval. We calculate the one step exponential divergence with the standard technique by simultaneously integrating a perturbed trajectory $u'(t)$ initially at a distance δ from the original trajectory $u(t)$ in phase space and rescaling the perturbed trajectory to the original distance δ at every integration time step.[21,22] The local Lyapunov exponent $\chi(\delta)$ at time t

$$\chi(\delta) = \frac{1}{\delta t} \left\langle \ln \left(\frac{\delta u(t+\delta t)}{\delta u(t)} \right) \right\rangle_t \tag{2.12}$$

is then given by the time average of the one-step exponential divergence. Convergence to the leading local Lyapunov exponent is not guaranteed for a given finite time interval. Calculation of the sub-leading exponents with a direct dynamics approach is also not possible in general. To test for convergence in our particular case reported in Chapter 3, we varied the initial displacement δ from 10^{-8} to 6.5×10^{-6} (a.u.) with 10 different initial displacement vectors for selected 1 ps trajectories, and found no significant differences in the local Lyapunov exponents. This indicates that the initial displacement vector reorients quickly enough along the most unstable direction in phase space, which is fortunate for our study of the ethyl radical.

Bibliography

[1] A. Bach, J. Hostettler, and P. Chen, J. Chem. Phys. **123**, 021101 (2005).

[2] M. A. Collins, Theor. Chem. Acc. **108**, 313 (2002).

[3] A. D. Boese, N. L. Doltsinis, N. C. Handy, and M. Sprik, J. Chem. Phys. **112**, 1670 (2000).

[4] A. D. Boese, J. M. L. Martin, and N. C. Handy, J. Chem. Phys. **119**, 3005 (2003).

[5] B. G. Levin, C. Ko, J. Quenneville, and T. J. Martinez, Mol. Phys. **104**, 1039 (2006).

[6] J. Tully, J. Chem. Phys. **93**, 1061 (1990).

[7] G. Granucci and M. Persico, J. Chem. Phys. **126**, 134114 (2007).

[8] G. Worth, P. Hunt, and M. Robb, J. Chem. Phys. A **107**, 621 (2003).

[9] C. Zhu, S. Nangia, A. Jasper, and D. Truhlar, J. Chem. Phys. **121**, 7658 (2004).

[10] J. Hostettler, L. Castiglioni, A. Bach, and P. Chen, Phys. Chem. Chem. Phys. **11**, 8262 (2009).

[11] A. Bach, J. Hostettler, and P. Chen, J. Chem. Phys. **125**, 024304 (2006).

[12]J. Hostettler, A. Bach, and P. Chen, J. Chem. Phys. **130**, 034303 (2009).

[13]S. Chapman and D. L. Bunker, J. Chem. Phys. **62**, 2890 (1975).

[14]G. A. Jones, B. K. Carpenter, and M. N. Paddon-Row, J. Am. Chem. Soc. **121**, 11171 (1999).

[15]C. C. Martens, M. J. Davis, and G. S. Ezra, Chem. Phys. Lett. **142**, 519 (1987).

[16]L. Vela-Arevalo and S. Wiggins, Int. J. Bifurcat. Chaos **11**, 1359 (2001).

[17]P. Goupillaud, A. Grossmann, and J. Morlet, Geoexploration **23**, 85 (1984).

[18]C. Chandre, S. Wiggins, and T. Uzer, Physica D **181**, 171 (2003).

[19]C. Siopis, B. L. Eckstein, and H. E. Kandrup, Ann. Ny. Acad. Sci. **867**, 41 (1998).

[20]V. Oseledec, Trans. Moscow Math. Soc. **19**, 197 (1968).

[21]A. Wolf, J. Swift, H. Swinney, and J. Vastano, Physica D **16**, 285 (1985).

[22]E. Aurell, G. Boffetta, A. Crisanti, G. Paladin, and A. Vulpiani, J. Phys. A. **30**, 1 (1997).

Chapter 3

Dissociation Dynamics of the Ethyl Radical

I. Introduction

Ethyl radical is an important intermediate in hydrocarbon crackers and combustion processes, being the principal precursor to ethylene through loss of a hydrogen atom.[1] The central role of ethylene in the petrochemical industry confers to the ethyl to ethylene reaction a high importance, with not only the thermochemistry, but also the kinetics being of interest. Detailed experimental studies in the relevant high-energy regime had previously worked with the assumption of statistical behavior.[2,3] Anomalous lifetimes for highly energized radicals in unimolecular dissociation experiments[4–6] under collision-free conditions have significant consequences for the analogous dissociations under conditions where collisional activation and deactivation occur on a timescale not too different from chemical reactions. The microcanonical rates of dissociation of small hydrocarbon radicals are not only important parameters in the modeling of high-energy processes such as combustion or plasma chemistry; they provide a detailed test of statistical rate theories that underlie the more general understanding of reaction dynamics in all branches of chemistry.[7,8]

Accordingly, the ethyl to ethylene system has been investigated in photodissociation experiments[4,9–14] that produced both fast and slow hydrogen atoms and ethylene following electronic excitation to low-lying Rydberg excited states. Two recent studies[4,9] of the dissociation dynamics of ethyl have found that highly excited radicals can dissociate with a fast and a slow

component, with the slower component decaying four-to-five orders of magnitude more slowly than predicted by RRKM theory,[15,16] even though the $\sim$ 105 kcal/mol initial excitation to the $\widetilde{A}$-state far exceeds the 36.8 kcal/mol barrier to unimolecular dissociation.

The mechanism for C-H bond fission and nonradiative decay from low-lying excited states in hydrocarbon radicals is not well understood. Previous experimental[4,9–14] and theoretical studies[17–20] suggested that both internal conversion followed by unimolecular dissociation and nonadiabatic dissociation pathways play an important role in the ethyl radical. Following electronic excitation of the ethyl radical to the $3s$ Rydberg excited state ($\widetilde{A}\ ^2A'$), adiabatic dissociation produces H and excited state ethylene ($\widetilde{a}\ ^3B_{1u}$) and nonadiabatic dissociation forms H and ground state ethylene ($\widetilde{X}\ ^1A_g$), see Fig. 3.1. Amaral *et al.*[9] observed a site selective loss of fast hydrogen atoms from the methyl group with an anisotropic angular distribution in photodissociation of the ethyl radical consistent with nonadiabatic dissociation. In addition to this nonadiabatic mechanism, both Gilbert *et al.*[4] and Amaral *et al.*[9] suggested that the slow hydrogen atoms observed in their photodissociation experiments arise from unimolecular dissociation following fast internal conversion.

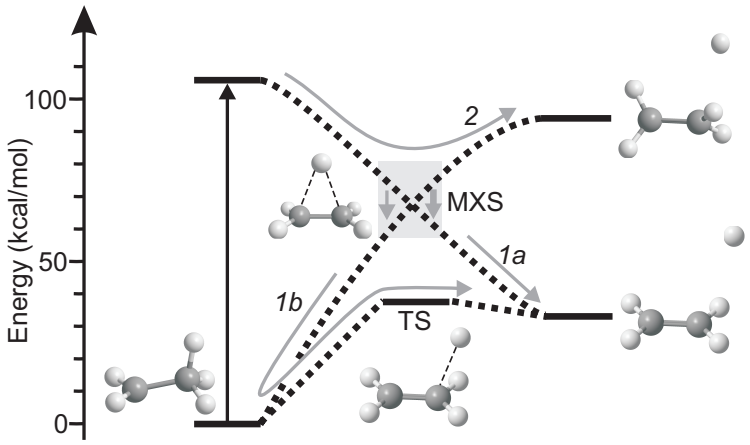

Figure 3.1: Schematic energy level diagram for the dissociation of the ethyl radical following excitation to the $\widetilde{A}$-state to C_2H_4 and H. Adiabatic dissociation (*2*) produces excited state ethylene and H in competition with nonadiabatic dissociation (*1a*). Surface hopping near the minimum on the crossing seam (MXS) can also generate hot ground state radicals followed by unimolecular dissociation (*1b*).

Here we report a semiclassical treatment of the photodissociation dynamics using direct dynamics trajectory with surface hopping calculations.

We simulate the photodissociation of the ethyl radical following electronic excitation to the $3s$ Rydberg excited electronic state using a large ensemble of nearly 5000 trajectories up to dissociation to C_2H_4 and H, even for trajectories that generate hot ground state radicals followed eventually by unimolecular dissociation. Our trajectory surface hopping study shows that the unusually slow dissociation rate of highly excited ethyl radicals cannot arise from a slow multi-step electronically excited state deactivation, but must arise from slow dissociation on the ground state surface. We also investigate the anomalous and unexpected kinetic behavior by means of classical trajectory[15,21] calculations in the ground electronic state using a full 21-dimensional potential surface for C_2H_5.

These classical trajectories show significant episodes of quasiperiodic behavior[22] in a time-frequency analysis,[23,24] which we postulate to be the origin of anomalously long lifetimes against dissociation observed in both the computational and experimental investigations[4,9] of the radical. We also quantify the extent of nonergodic behavior in the unimolecular dissociation of the ethyl radical using the normalized instantaneous orbital complexity, a time-dependent scalar metric based on the time-frequency decomposition of the classical trajectories using wavelets.[25] We show that the normalized instantaneous orbital complexity correlates not only to the more conventional Lyapunov exponents, but also to the dissociation time for an individual trajectory. The analysis of the ensemble of trajectories confirms that the long-lived trajectories are associated with a low degree of ergodicity. While the analysis of molecular dissociation dynamics is the narrow focus of the present work, the method is more general for discovery and identification of ordered regimes within large sets of chaotic data.

II. Results

A. Nonadiabatic Dynamics

Potential Energy Surfaces

The quality of the potential energy surfaces play a crucial role in the simulation of the photodissociation dynamics of the ethyl radical. A summary of the energetic results from the SA–MCSCF and the MR–CISD level of theory appear in Table 3.1. Comparing the energetic results of both levels of theory illustrates the sensitivity of the potential energy on the dissociation

rates and branching ratios between adiabatic and nonadiabatic dissociation, as discussed in the next sections. The SA–MCSCF method yields a dissociation energy of the ethyl radical forming ground state ethylene and H of only 20.2 kcal/mol, 14 kcal/mol less than the experimental value.[2] The dissociation energy for the $C_2H_4(\widetilde{a})$ + H channel at the SA–MCSCF level is also 13.3 kcal/mol too low compared to experiment. The MR–CISD level of theory still underestimates the dissociation energy to form ground state ethylene and H by about 4 kcal/mol but predicts 93.2 kcal/mol for the $C_2H_4(\widetilde{a})$ + H channel in excellent agreement with the experimental value of 93 kcal/mol.[26]

Table 3.1: Calculated reaction energies, transition state (TS) for unimolecular dissociation and minimum on the crossing seam (MXS) of the ethyl radical (in kcal/mol)

	SA–MCSCF 6-31++G(*d,p*)	MR–CISD 6-31++G(*d,p*)	QCISD(T) 6-311+G(*2df,p*)[1]
	Classical		
TS	32.85	40.67	41.58
$C_2H_4(\widetilde{X})$+H	25.84	35.87	38.07
$C_2H_4(\widetilde{a})$+H	88.94	102.15	105.96[2]
MXS	67.63	70.72	–
	Zero-point corrected		
TS	28.43	35.98	37.24
$C_2H_4(\widetilde{X})$+H	20.18	29.89	32.66
$C_2H_4(\widetilde{a})$+H	79.48	93.15	97.28[2]

[1]From Ref. 27

[2]This work calculated with the method described in Ref. 27

The SA–MCSCF level of theory predicts a zero-point corrected barrier for unimolecular dissociation of $C_2H_5 \rightarrow C_2H_4$+H of only 28.4 kcal/mol, almost 10 kcal/mol lower than MR–CISD, but overestimates the reverse barrier by ∼4 kcal/mol compared to other *ab initio* calculations.[27,28] The MR–CISD reaction energies compare favorably with the results by Hase *et al.*[27] using QCISD(T) and the larger 6-311+G(*2df,p*) basis set. The relatively poor reaction energies at the SA–MCSCF level of theory arise from the different character of the excited states of the ethyl radical compared to ethylene and H. The SA–MCSCF method averages a π and a Rydberg state in ethyl but averages two states with π character for ethylene and H. This leads to a wave function with better quality for the products than for the ethyl radical and yields a dissociation energy that is too low. This is an inherent problem of

the state averaging that neither larger basis sets nor a larger active space can solve. Furthermore, the vertical excitation energy at the SA–MCSCF level of theory is only 110.9 kcal/mol, about 5 kcal/mol too low compared to experiment. Including dynamic correlation at the MR–CISD level of theory gives a vertical excitation energy of 115.3 kcal/mol, in excellent agreement with the experimental value of 116 kcal/mol.[29] We chose the MR–CISD level of theory for our trajectory calculations because of the good agreement of the energetic results compared to experiments and use the SA–MCSCF method to illustrate how sensitively the dissociation dynamics depend on the quality of the potential energy surfaces.

Excited State Lifetime and Product Branching Ratio

The population decay of the first excited electronic state of the ethyl radical obtained from the fraction of trajectories in the excited state appears in Fig. 3.2. During the first 12 fs of the simulation the population remains nearly constant and then decays exponentially to an asymptotic value of 0.48 at the SA–MCSCF and 0.15 at the MR–CISD level of theory. An exponential fit to the population decay gives a time constant τ=18 fs for SA–MCSCF and τ=20 fs for MR–CISD. In a recent pump-probe photoionization experiment of jet-cooled ethyl, Zierhut *et al.*[30] obtained a monoexponential decay of the ion-signal following electronic excitation to 3s Rydberg excited state with a time constant $\tau = 20 \pm 3$ fs, in good agreement with our theoretical predictions.

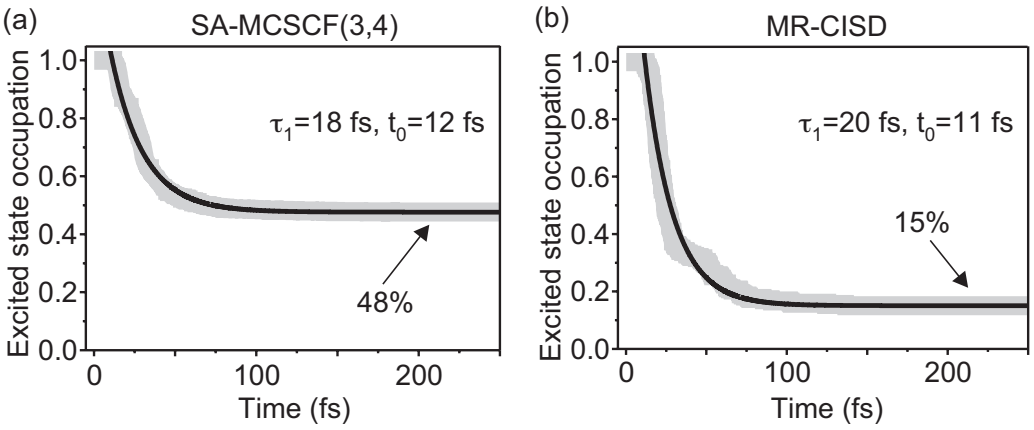

Figure 3.2: Population decay of the $\widetilde{A}$-state of ethyl radical obtained from the fraction of trajectories in the excited state.

The most interesting aspect is the change in branching ratio obtained from the asymptotic value of the population decay between adiabatic and nonadiabatic dissociation for the two levels of theory. Nearly half of the trajectories at the SA–MCSCF level of theory dissociate adiabatically, see Table 3.3 and Fig. 3.2(a). This is an unusually large fraction, as the excited state potential energy surface does not have a barrier[19] between the Franck-Condon region and the MXS that lies 43.3 kcal/mol below the vertical excitation energy of the ethyl radical. Furthermore, the MXS is ∼35 kcal/mol above the transition state that leads to the $C_2H_4(\widetilde{X})$ and H products. These energetics should lead primarily to a fast nonadiabtic dissociation to form the H + $C_2H_4(\widetilde{X})$ products.

Table 3.3: Average kinetic energy release $\langle E_T \rangle$ and distribution maximum $E_{T,max}$ of the three product channels for the ethyl radical photodissociation in kcal/mol.

Products	Channel	Branching (%)	$\langle E_T \rangle$	$E_{T,max}$
		SA–MCSCF		
$C_2H_4(\widetilde{X})$+H	*1a*	45	58.6	65.6
$C_2H_4(\widetilde{X})$+H	*1b*	6	22.4	21.4
$C_2H_4(\widetilde{a})$+H	*2*	49	10.5	10.2
		MR–CISD		
$C_2H_4(\widetilde{X})$+H	*1a*	68	43.5	52.2
$C_2H_4(\widetilde{X})$+H	*1b*	17	17.7	16.0
$C_2H_4(\widetilde{a})$+H	*2*	15	3.4	2.1

A possible explanation for the dramatic difference in the branching ratio between the two levels of theory comes from the dissociation energy for the $C_2H_4(\widetilde{a})$ + H channel that is 13.3 kcal/mol too low compared to experiment at the SA–MCSCF level, but agrees with the experimental value of 93 kcal/mol at the MR–CISD level of theory. The branching ratio is not only determined by the energetics but also by the surface hopping probability, which is proportional to the product of the nuclear velocities and the nonadiabatic coupling. We cannot completely rule out that unexpected branching ratio arises from a lower surface hopping probability at the SA–MCSCF level of theory compared to MR–CISD.

Ethyl Radical Dissociation

We calculate the lifetime of ethyl radicals with respect to C-H bond fission separately for the competing adiabatic and nonadiabatic dissociation channels. The lifetime distributions for nonadiabatic dissociation appear in Fig. 3.3(a) for SA–MCSCF and Fig. 3.4(a) for the MR–CISD level of theory. They both have a fast and a slow component that is well modeled

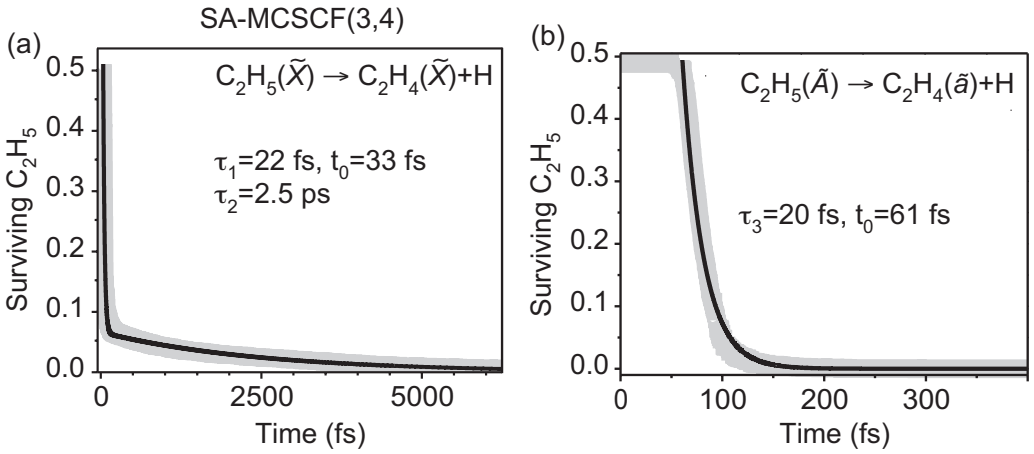

Figure 3.3: Lifetimes of C_2H_5 with respect to dissociation obtained from the SA–MCSCF(3,4) trajectories producing ground state (a) and excited state (b) ethylene and H. The solid lines show (bi)exponential fits to the lifetime distributions.

with a biexponential fit to the lifetime distribution with time constants τ_1 and τ_2. Inspecting the nuclear motions in the trajectories reveals that the ethyl radicals with the short lifetime $\tau_1 \sim 30$ fs dissociate promptly after surface hopping via pathway *1a*, see Fig. 3.1. The long-lived trajectories with $\tau_2 \sim 2$ ps follow pathway *1b* and generate highly energized ground state ethyl followed eventually by unimolecular dissociation. The major difference in the lifetime distributions for the two levels of theory is the fraction of long-lived trajectories in nonadiabatic dissociation that increases from 13% to 25% when including dynamic electron correlation at the MR–CISD level of theory, see Table 3.3. The larger fraction of long-lived trajectories at the MR–CISD level of theory most likely comes from the transition state for unimolecular dissociation that is ∼7 kcal/mol higher in energy compared to SA–MCSCF.

The ethyl radical can also dissociate adiabatically to form electronically excited state ethylene and a hydrogen atom. The lifetime distribution for dissociation to the $C_2H_4(\widetilde{a})$ + H products is well modeled by a single expo-

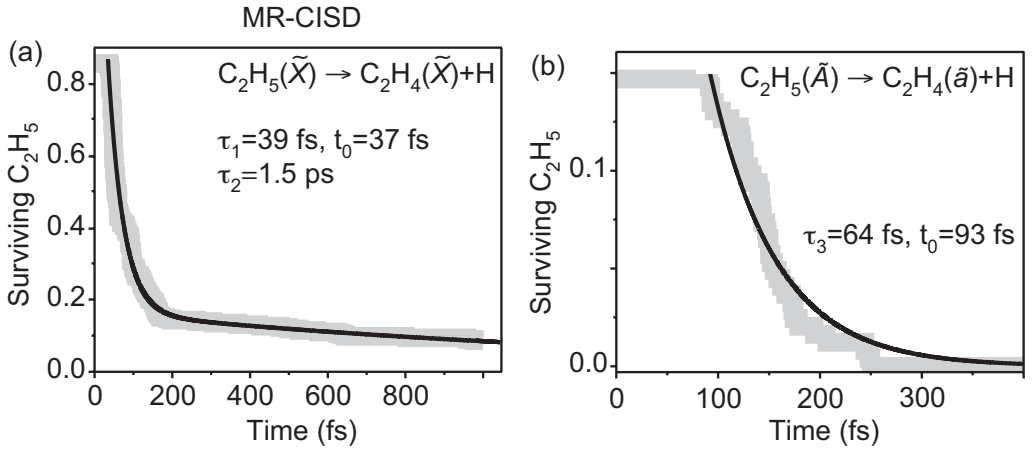

Figure 3.4: Lifetimes of C_2H_5 with respect to dissociation obtained from the MR–CISD trajectories producing ground state (a) and excited state (b) ethylene and H. The solid lines show (bi)exponential fits to the lifetime distributions.

nential, see Fig. 3.3(b) and Fig. 3.4(b). The higher dissociation energy at the MR–CISD level of theory for that channel not only reduces the energy available to the products but may also explain the slower dissociation with a time constant $\tau_3 = 64$ fs obtained from MR–CISD. The different potential energy surfaces not only lead to different branching ratios and dissociation lifetimes but also affect the energy disposal in the photofragments. To unravel these differences, we determine the recoil energy distributions of the photofragments obtained from both levels of theory for the competing dissociation pathways.

Recoil Energy Distributions

The H-atom Rydberg tagging experiments of Amaral *et al.*[9] provide high-resolution recoil energy distributions for the photodissociation of the ethyl radical that we can compare to our simulations. Figure 3.5 shows the kinetic energy release distributions that we obtain from the complete ensemble of trajectories with the individual contributions that arise from the three different dissociation pathways, a component for adiabatic dissociation and two components for nonadiabatic dissociation separated according to their dissociation lifetime τ_1 and τ_2 using the fraction of trajectories defined by the biexponential fit to the lifetime distributions. The low recoil energy fragments of the bimodal distribution arise mainly from unimolecular dissociation following surface hopping and from adiabatic dissociation

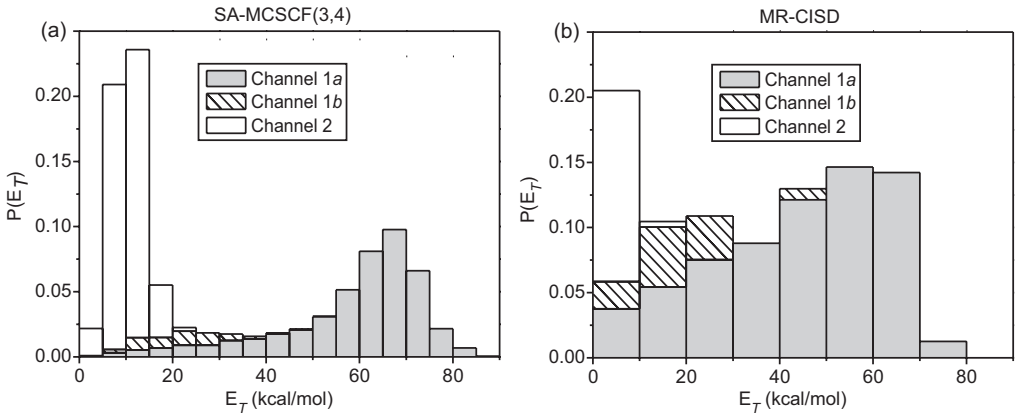

Figure 3.5: Recoil energy distributions for the three competing dissociation channels defined in Fig. 3.1.

while the high recoil energy fragments come from fast nonadiabatic dissociation to form ground state ethylene and H. The recoil energy distributions for the two levels of theory differ most noticeably at lower energy with the prominent feature arising from adiabatic dissociation clearly visible for SA–MCSCF, shown in Fig. 3.5(a). At the MR–CISD level of theory, only 15% of all trajectories pass the conical intersection and dissociate adiabatically producing very slow hydrogen atoms with $\langle E_T \rangle$ =3.4 kcal/mol, see Table 3.3. Unimolecular dissociation of highly energized ground state ethyl radicals following dissociation pathway *1b* through the conical intersection also yields low recoil energy photofragments. The average kinetic energy release for that channel is $\langle E_T \rangle$ =17.7 kcal/mol at the MR–CISD level of theory, which corresponds to 24% of the available energy using the average 105.0 kcal/mol excitation energy at the MR–CISD level of theory. The recoil energy distributions of Amaral *et al.* are also bimodal with a low energy feature peaking at $\langle E_T \rangle$ ∼12 kcal/mol that the authors tentatively assign to unimolecular dissociation. Our simulations predict that photofragments produced both by unimolecular dissociation following surface hopping and adiabatic dissociation contribute to that low energy part of the recoil energy distributions. Even though both dissociation channels produce fragments with very low recoil energies, the angular distribution of the photofragments for the two channels should be different. The experiments of Amaral *et al.* also provide the energy dependent anisotropy parameter $\beta(E_T)$ that we can use as a point of comparison for our calculated angular distributions.

We calculate the angle between the transition dipole moment μ of the initial $\widetilde{A} \leftarrow \widetilde{X}$ electronic excitation and the velocity vector of the released hydrogen atom at the SA–MCSCF level of theory and obtain the angular distributions for the different dissociation pathways. The calculated angular distribution for adiabatic dissociation appears in Fig. 3.6(c) and peaks at 18.0 ± 2.0 degrees. This dissociation channel produces an anisotropic angular distribution, as the dissociation lifetime for that channel of ~ 100 fs is much less than the rotational period of ethyl radical, even though the average kinetic energy release is only 10 kcal/mol. The long-lived ethyl radicals with a lifetime $\tau_2 = 2.5$ ps for unimolecular dissociation produce a distinctly different angular distribution shown in Fig. 3.6(b). This distribution is nearly uniform indicating an almost isotropic angular distribution with a corresponding anisotropy parameter $\beta \sim 0$. The low signal-to-noise at very low recoil energies typical for H-atom Rydberg tagging experiments unfortunately precludes identifying a contribution from adiabatic dissociation using our predictions in the experimental distribution from Amaral *et al.*[9] An ion-imaging experiment could provide a test for our prediction that both adiabatic dissociation and unimolecular dissociation following surface hopping yield fragments with low recoil energy.

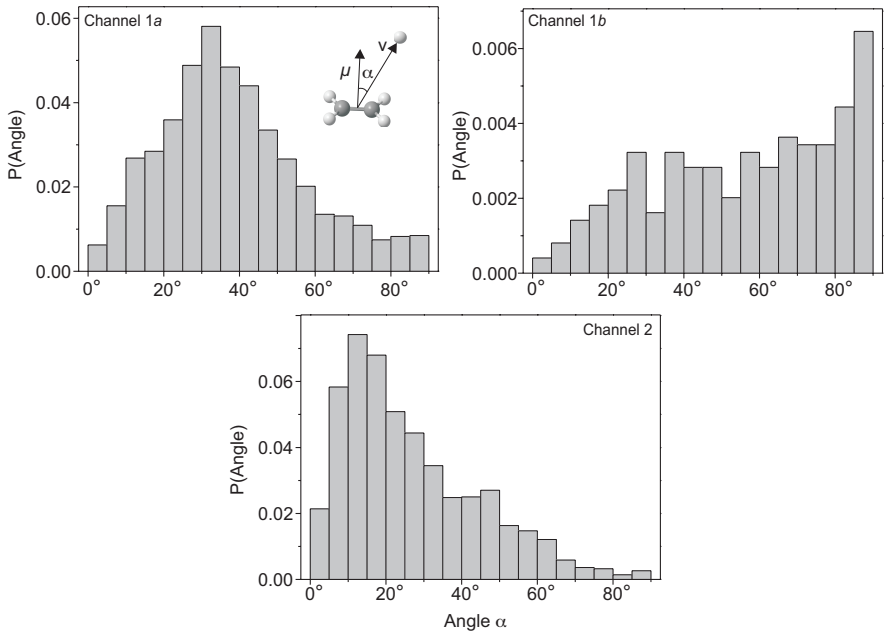

Figure 3.6: Distribution of the angle between the transition dipole μ of the initial $\widetilde{A} \leftarrow \widetilde{X}$ electronic excitation and the velocity of the departing hydrogen atom obtained from the SA–MCSCF trajectories for the three competing dissociation channels.

The major contribution in the recoil energy distributions shown in Fig. 3.5 comes from ethyl radicals with a short dissociation lifetime τ_1 that produce fragments with high recoil energies peaking at 66 kcal/mol at the SA–MCSCF level of theory. Those fragments arise from fast nonadiabatic dissociation leading to ground state ethylene and H. The calculated angular distribution for this channel appears in Fig. 3.6(a) and is also anisotropic peaking at 34.0 ± 0.8 degrees. Amaral *et al.* determine an energy dependent anisotropy parameter $\beta(E_T)$ in their experiments that peaks at $\beta \sim 0.5$ for recoil energies between $E_T = 60$ and 75 kcal/mol. This β value indicates a $\sim 45°$ angle between the transition dipole μ of the $\widetilde{A} \leftarrow \widetilde{X}$ transition and the velocity direction of the recoiling hydrogen atoms, in good agreement with our theoretical predictions.

B. Unimolecular Dissociation in the Ground Electronic State

In this section, we investigate the anomalous and unexpected kinetic behavior of the ethyl radical by means of classical trajectory calculations in the ground electronic state using a full 21-dimensional potential surface for C_2H_5, see also Chapter 2 and Ref. 28. Figure 3.7 shows the fraction of surviving ethyl radicals calculated from the lifetime against dissociation time of the 410 classical trajectories. The solid line in Figure 3.7 is a single-exponential fit with a rate constant k_1 of $1.3 \times 10^{12}\mathrm{s}^{-1}$ with ∼22% of the ethyl radicals surviving for much longer than 2 ps. The dashed line shows the best single-exponential fit constrained to decay to baseline. In comparison, RRKM calculations predict a rate constant for C-H bond fission at

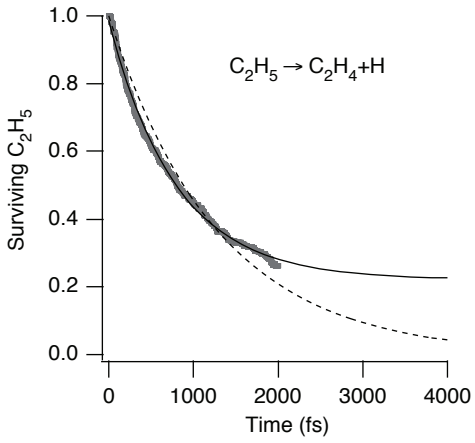

Figure 3.7: Lifetimes of C_2H_5 with respect to dissociation as determined by classical trajectories on a full 21-dimensional calibrated DFT potential surface. The solid line shows the fit to a single exponential decaying to an asymptotic value of 0.22 with a time-constant τ = 770fs. The dotted line shows the best fit exponential constrained to decay to zero.

100-120 kcal/mol total energy in the range $10^{11} - 10^{12}$ s^{-1}.[4,15] The lifetime distribution in Figure 3.7 indicates that the ethyl radical dissociation process at 120 kcal/mol excitation is intrinsically non-RRKM with a clear long-lived component.

To help identify molecular motions associated with anomalously long lifetimes, several trajectories were selected randomly from the trajectories surviving at least 2 ps. These trajectories were subjected to time-frequency analysis (see Chapter 2) by way of a wavelet transformation[31] of the reduced-mass-weighted Cartesian coordinates. Equivalent results could be obtained by analysis of the conjugate momenta. A representative density plot of the scale-normalized modulus of the continuous wavelet transform for one reduced-mass-weighted Cartesian coordinate is shown in Figure 3.8. The

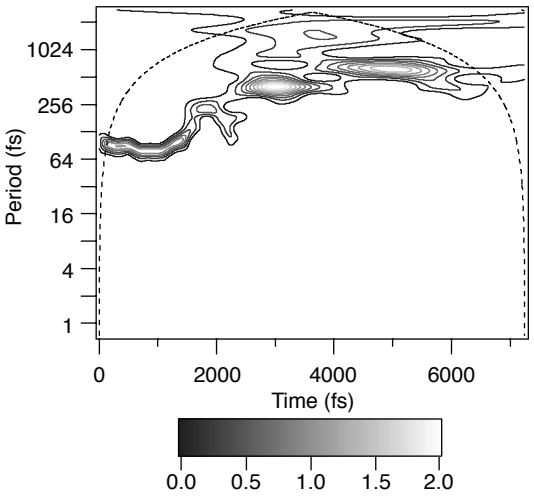

Figure 3.8: Representative spectrogram for one degree of freedom taken from one of the long-lived trajectories after the wavelet transform. The plot shows repeated episodes during which energy is localized in one quasiperiodic motion. The dotted line indicates the cone of influence, outside of which one may expect artifactual edge effects from the wavelet transform. For this particular trajectory, the quasiperiodic episodes displays primarily a counter-rotation of the CH_3 and CH_2 groups.

spectrogram, in the form of a contour plot analogous to a topographic map, shows a landscape of ridges or instantaneous frequency curves corresponding to time-frequency energy localization. Multiple, short-lived, low-intensity ridges in a time-frequency plot characterize a strongly chaotic trajectory. A quasiperiodic trajectory has typically only one high-intensity ridge with a near-constant frequency persisting for an extended stretch of time, and only small modulations from oscillations about the expected frequency, indicative of a localization of energy in a single recurring motion. Truncating the density plots for all 21 degrees of freedom at a threshold set to exclude nonperiodic motions, and then applying an inverse wavelet transform, a procedure adapted from noise-filtering and compression of digital audio signals,[31] reconstructs the motions associated with the quasiperiodic motions. Several (very) large amplitude motions can be identified that persist for extended

stretches of time; an out-of-plane methylene rock coupled to a methyl torsion, seen in high-resolution spectroscopic studies,[32–34] dominates many of the long-lived trajectories. Other large amplitude motions can also be important. A counter-rotation of the methyl and methylene groups characterizes the quasiperiodic segments of the trajectory in Figure 3.8.

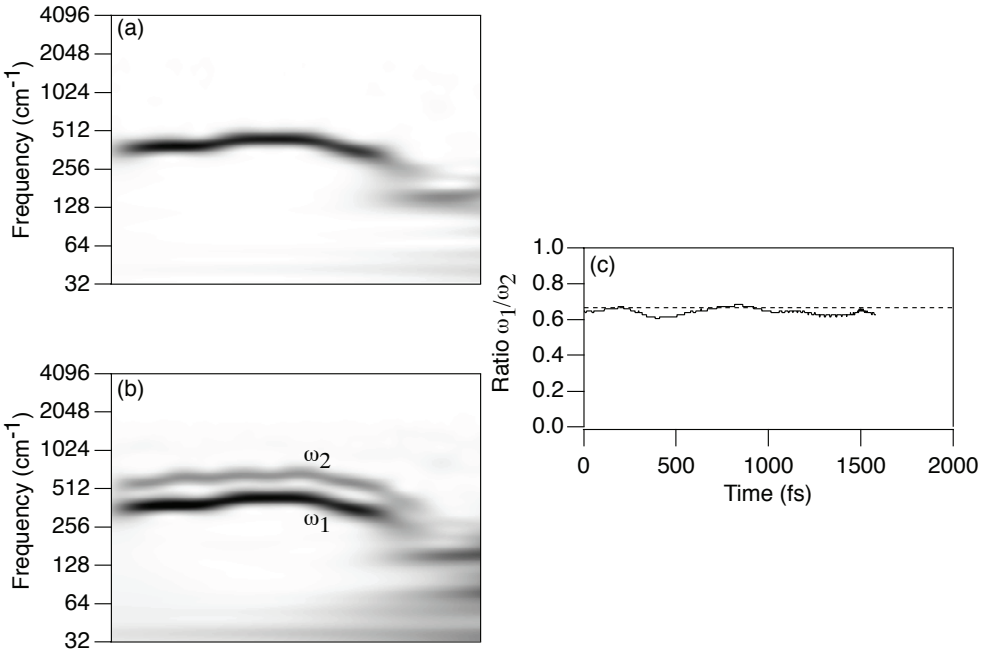

Figure 3.9: (a) Spectrogram for one degree-of-freedom taken from one of the long-lived trajectories after the wavelet transform. The sum off all 21 spectrograms (b) reveals a 3:2 resonance (c).

Figure 3.9(a) shows a different representation of the spectrogram for the time interval t=[0,2000] fs obtained from a representative degree-of-freedom from the long-lived trajectory shown in Figure 3.8. A single instantaneous frequency curve dominates this spectrogram and also the spectrograms for the other 20 degrees-of-freedom in the time interval t=[0,1570] fs. This trajectory segment corresponds to an episode of quasiperiodic motion while other trajectory segments reveal multiple short-lived ridges characterizing a chaotic trajectory segment. The trajectory segment shown in Fig. 3.9 is characterized by a counter-rotation of the methyl and methylene groups in the ethyl radical. A detailed inspection of the spectrograms also reveals a second ridge or instantaneous frequency curve not visible in the image plot in Fig. 3.9(a) because the corresponding motion is only very weakly coupled to the dominant counter-rotation of the methyl and methylene groups, at

least in the Cartesian coordinates used in the wavelet analysis. We show a better visualization of this second ridge in Fig. 3.9(b) using the sum of all 21 spectrograms. The trajectory segment in the time interval t=[0,1570] fs can be described with two instantaneous frequencies ω_1 and ω_2 with $\langle\omega_1\rangle$=378 cm^{-1} and $\langle\omega_2\rangle$ = 587cm^{-1}. Even though both frequencies drift slightly in the time interval, their ratio $\omega_1 : \omega_2$ remains very nearly constant at 3:2, as shown in Fig. 3.9(c). The trajectory is thus trapped in or near a 3:2 resonance between ω_1 and ω_2 for 1570 fs. Using wavelet filtering we also identified the motion associated with ω_2 and found that it corresponds to an out-of-plane methylene rock with some C-C stretch character.

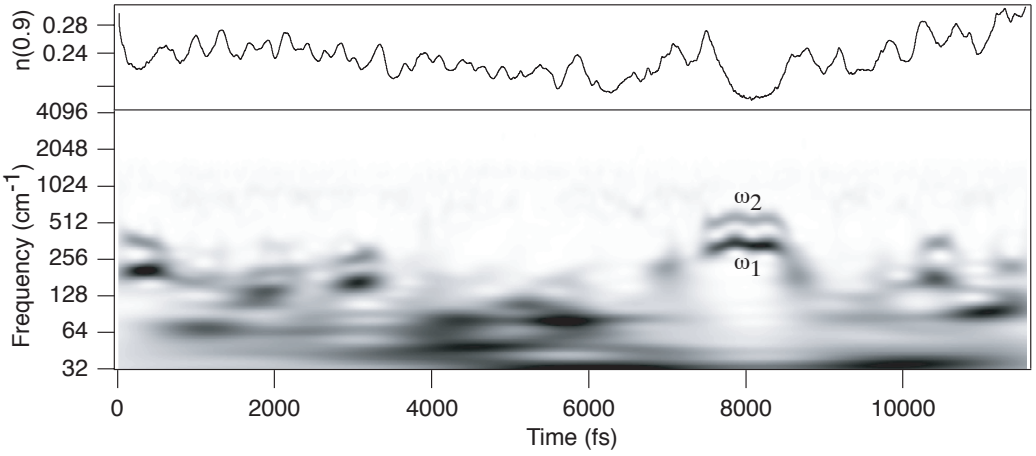

Figure 3.10: Sum of all 21 spectrograms of a long lived trajectory with a 3:2 resonance trapping between ω_1 and ω_2 during which the instantaneous orbital complexity $n(0.9)$ remains nearly constant at 0.18

Other long-lived trajectories also show resonance trappings that occur not only in the first 2 ps of a trajectory. Figure 3.10 shows the sum of all 21 spectrograms for another long-lived trajectory which is trapped in or near a 3:2 resonance between ω_1 and ω_2 in the time interval t=[7425,8483] fs. Using the same analysis technique we find that both the frequencies ω_1 and ω_2 and their corresponding motions are nearly identical in the two selected time intervals for both long-lived trajectories. Other trajectory segments in the long-lived trajectories show similar prominent resonance trappings where the instantaneous frequencies approximately satisfy the resonance equation but with different integer ratios. These episodes typically persist for 0.5 to 2 ps and the components of the large amplitude motions are best described

as a counter-rotation of the methyl and methylene groups, an out-of-plane methylene rock, and a motion with C-C stretch and CH_3 umbrella character.

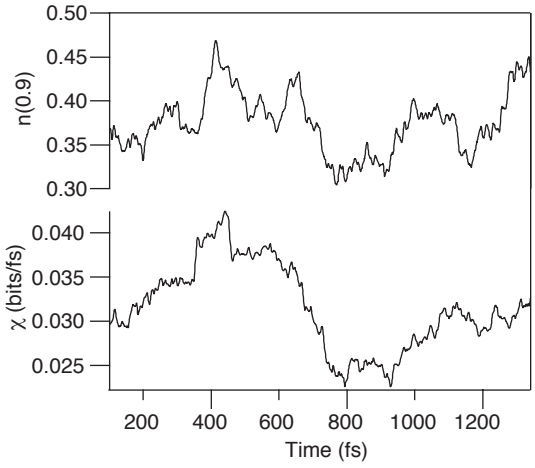

Figure 3.11: Time evolution of the normalized instantaneous orbital complexity $n(0.9)$ and the largest local Lyapunov exponent χ for a selected trajectory.

Figure 3.11 shows the strong correlation between the largest local Lyapunov exponents averaged over 100 fs and the normalized instantaneous orbital complexity for a selected trajectory of ethyl radical. The feature centered at 650 fs appears more prominently in the instantaneous orbital complexity than in the largest local Lyaponov exponents, but appears more clearly with a time average of 80 fs. For this particular trajectory we find a roughly linear correlation of the instantaneous orbital complexity and the largest local Lyapunov exponent averaged over 100 fs with a rank correlation $\mathcal{R}[n(0.9), \chi]$ of 0.88, a similar value as obtained by Siopis *et al.* in two- and three-dimensional model Hamiltonian systems using the Fourier transform based analog of the orbital complexities.[35–37] Both metrics can easily distinguish chaotic trajectory segments and episodes of quasiperiodic behavior characterized by a trajectory segment with very small and almost constant largest local Lyapunov exponent and a corresponding very small instantaneous normalized orbital complexity. The instantaneous orbital complexity for trajectory segment shown in Fig. 3.9(b) remains nearly constant at $n(0.9) = 0.16$ in the interval t=[0,1570] fs. We found a very similar value of $n(0.9) \sim 0.18$ in the episode between t=[7425,8483] fs in the long-lived trajectory shown in Fig. 3.10, which is also trapped in or near a 3:2 resonance between ω_1 and ω_2. We also calculated both the normalized instantaneous orbital complexities and the largest local Lyapunov exponent for all the other trajectories in the microcanonical ensemble and found an acceptably linear correlation with $\mathcal{R}[n(0.9), \chi]$ typically between 0.75 and 0.95.

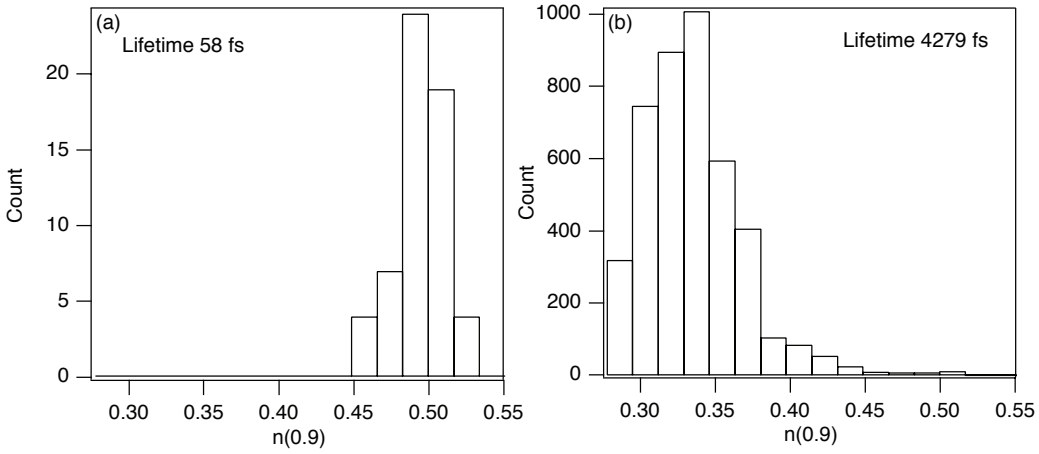

Figure 3.12: Histograms of the normalized instantaneous orbital complexity for a short-lived (a) and (b) a long-lived trajectory of the microcanonical ensemble.

To characterize the dynamics of the whole ensemble of trajectories we compute the central moments of the distribution of the normalized instantaneous orbital complexities for each trajectory. Figure 3.12 shows representative histograms of the distribution of $n(0.9)$ for a very short-lived trajectory (a) with $\langle n(0.9)\rangle = 0.49$ and a long-lived trajectory (b) with a much smaller average orbital complexity of 0.33. Both distributions are distinctly asymmetric with a positive skew for the long-lived trajectory, indicating that the selected trajectory spends more time in less chaotic regions of phase space. A similar approach using probability distributions of local Lyapunov exponents for selected trajectories has already been used by Berry and co-workers to study the nonergodic behavior of rare gas clusters.[38,39] The plots in Figure 3.13 show the average and the skew of the distribution of the individual trajectories of the microcannonical ensemble as a function of dissociation time. All the long-lived trajectories are characterized by a low average complexity and a positive skew of the distribution which both clearly correlate with the lifetime against dissociation.

III. Discussion

A. Nonadiabatic Dynamics

The excited state lifetime and the recoil energy distributions of our simulations are consistent with previous measurements,[4,9,11,12,30,40] but in ad-

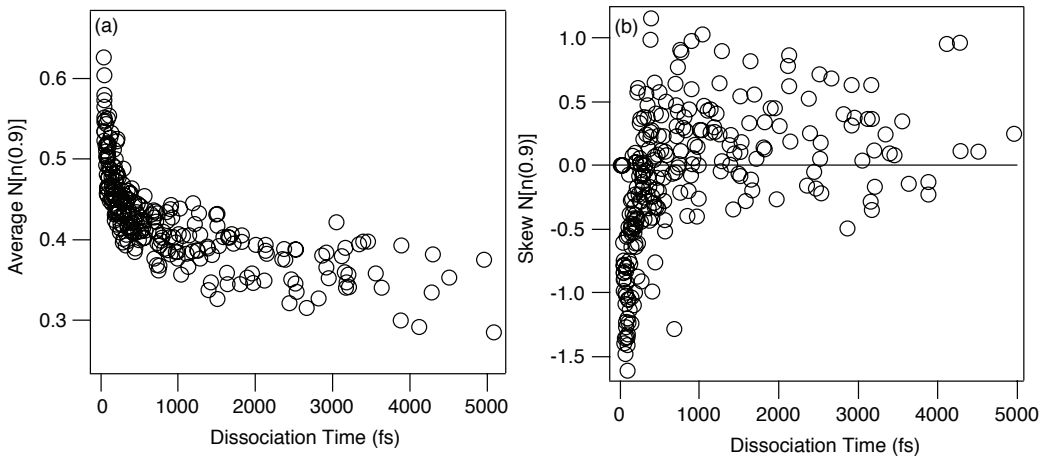

Figure 3.13: Average (a) and skew (b) of the distributions of the instantaneous orbital complexity for each trajectory of the ensemble as a function of the dissociation time of the trajectories.

dition we also observe the adiabatic dissociation pathway producing excited state ethylene and H. The mechanism for nonradiative decay from low-lying excited states in hydrocarbon radicals is not well understood. For the ethyl radical, Sevin *et al.*[17] first predicted a nonadiabatic dissociation pathway to produce ground state ethylene and H. Zyubin *et al.*[19] later calculated minimum energy pathways in the $3s$ Rydberg state of the ethyl radical for hydrogen migration from the methyl group to the minimum on the crossing seam and predicted a barrierless dissociation to ground state ethylene and H. In addition to this nonadiabatic mechanism, both Gilbert *et al.*[4] and Amaral *et al.*[9] suggested that the slow hydrogen atoms observed in their photodissociation experiments arise from unimolecular dissociation following fast internal conversion.

Our simulations reproduce the measured excited state lifetime[30] of 20 fs and the shape of the calculated recoil energy distribution at the MR–CISD level of theory shown in Fig. 3.5 is similar to the one obtained from experiment.[9] In addition to the fast anisotropic hydrogen atoms produced by the nonadiabatic dissociation channel *1a*, our simulation also yields hot ground state ethyl radicals via pathway *1b* with a lifetime $\tau_2 = 1.5$ ps with respect to unimolecular dissociation forming ground state ethylene and H. The average kinetic energy release for these slow hydrogen atoms is $\langle E_T \rangle$ =17.7 kcal/mol at the MR–CISD level of theory, which corresponds to 24% of the available energy, a typical value for unimolecular dissociation in hydrocarbon radicals.

This is nearly identical to $\langle E_T \rangle = 18.1$ kcal/mol obtained from our trajectory calculations in Sec. B on unimolecular dissociation and is in reasonable agreement with the 27% reported by Gilbert *et al.*[4] in their photodissociation experiments. Amaral *et al.*[9] use the energy dependent anisotropy parameter $\beta(E_T)$ to partition their recoil energy distributions into a slow isotropic and a fast anisotropic component and obtain a fast/slow branching ratio of ~ 0.2. We cannot directly compare our branching ratios listed in Table 3.3 with their results because the partitioning schemes for the individual contributions to the recoil energy distributions are different. We use the dissociation lifetime τ_1 and τ_2 to divide trajectories into components corresponding to nonadiabatic dissociation and unimolecular dissociation following surface hopping. A fraction of ethyl radicals with the short lifetime τ_1 partially redistribute their energy before dissociation and give rise to the flat part of the recoil energy distribution centered at $E_T = 40$ kcal/mol shown in Fig. 3.5. This leads to a larger fraction of fast hydrogen atoms compared to Amaral *et al.* because they assigned that part of the recoil energy distribution to the slow dissociation channel based on a $\beta(E_T) \sim 0$. Applying their partitioning scheme to our calculated recoil energy distribution at the MR–CISD level of theory, we obtain a fast/slow branching ratio of 0.19 and an average kinetic energy release $\langle E_T \rangle = 26.9$ kcal/mol, or 36% of the available energy, for the slow dissociation channel and $\langle E_T \rangle = 63.4$ kcal/mol for the fast channel in good agreement with their experimental results. The good overall agreement of the simulation compared to experiment suggests that a strictly nonadiabatic mechanism, passage through the conical intersection, is the major mechanism for nonradiative decay following electronic excitation to the $3s$ Rydberg excited state in the ethyl radical.

Gilbert *et al.*[4] measured dissociation rates of highly excited ethyl radicals that are four-to-five orders of magnitude slower than predicted by RRKM theory.[15,41] In our trajectory calculations of the ethyl radical unimolecular dissociation described in Sec. B with a microcanonical ensemble of initial states the lifetime distribution was intrinsically non-RRKM with a clear long-lived component at a total energy of 120 kcal/mol, which is only 5 kcal/mol more than the vertical excitation energy at the MR–CISD level of theory in this report. The unusually long-lived trajectories with lifetimes far exceeding the ~ 1 ps RRKM lifetime showed episodes of quasiperiodic behavior associated with a low degree of ergodicity compared to the short-lived trajectories that dissociated with a time constant $\tau = 770$ fs.

The trajectory surface-hopping approach used here simulates the photodissociation experiments and should generate a more realistic ensemble of initial states for dissociation on the ground state surface compared to the random initial conditions reported in Sec. B. In contrast to our trajectory studies of ethyl radical unimolecular dissociation at a total energy of 120 kcal/mol, we find that the lifetime τ_2 with respect to C-H bond fission at an average excitation energy of 105.0 kcal/mol for the MR–CISD level of theory is of the same order of magnitude as the RRKM predictions for that energy range. Hase and co-workers[15,16,41] also found RRKM kinetics for ethyl radical dissociation at lower excitation energies than 120 kcal/mol and in the thermal kinetics of the H + C_2H_4 $\leftrightarrow$$C_2H_5$ system[42,43] using classical trajectory calculations with a reduced-dimension analytic potential energy surface.[21] To unravel the apparent inconsistency in the lifetime of the highly energized ground state ethyl radicals with respect to C-H bond fission, we examine and compare the accuracy of the different simulations and their ability to predict experimental observations.

The trajectory surface hopping method with Tully's fewest switches combined with potential energy surfaces described by the MR–CISD level of theory predicts an excited state lifetime and recoil energy distributions that are consistent with previous measurements. This level of theory also gives reaction energies and a vertical excitation energy that agree well with the experimental values in contrast to SA–MCSCF. Both the SA–MCSCF and the MR–CISD levels of theory do not yield any long-lived trajectories on the ground state surface in contrast to the results in Sec. B that showed non-RRKM dynamics using a calibrated density functional theory (DFT) potential energy surface,[25,28] in which long-lived trajectories displayed resonance trappings with regular type intramolecular motions for highly vibrationally excited ethyl radicals.

Large changes in both the curvature and anharmonicity of the ground state potential energy surface are likely to destroy the near resonance of the two frequencies describing these regular type intramolecular motions. In Sec. B and Chapter 2, we found a mean absolute error of only 0.5 cm^{-1} for the anharmonic vibrational frequencies of the ethyl radical obtained from calibrated DFT compared to experiment. Perhaps even more significant is that we found a near zero mean absolute error (MAE) of the potential energy for calibrated DFT relative to CCSD(T)/CBS energies for a set of 67 nuclear geometries of highly energized ethyl radicals. The SA–MCSCF method used

here has a MAE that is 54 times larger than calibrated DFT, nearly the same as the UHF potential used in our preliminary studies that also did not reveal any non-statistical behavior. The MR–CISD potential used in this report has a MAE that is still 34 times larger than calibrated DFT, only slightly smaller than SA–MCSCF. Moreover, the distributions of the potential energy differences between CCSD(T)/CBS and both SA–MCSCF and MR–CISD are not normally distributed, but skewed and centered at a large positive energy difference, see the discussion in Chapter 2. This indicates that both the calibrated DFT and the CCSD(T) ground state potential are considerably softer, yielding lower vibrational frequencies in excellent agreement with experimental values. The skewed energy error distributions of SA–MCSCF and MR–CISD also indicate that the anharmonicities of these potentials are rather different compared to CCSD(T)/CBS. It appears that the quality of the potential energy surface is decisive to successfully predict the non-statistical effects in ethyl radical dissociation.

We cannot rule out that trajectory runs with a better potential energy surface would not produce a larger fraction of long-lived trajectories that show quasiperiodic behavior as in the unimolecular dissociation of ethyl radicals reported in Sec. B. Neither can we confirm that the nonadiabatic transition following excitation to the $3s$ Rydberg state of ethyl radicals preferentially excites regions of the ground state's phase space that consist of regular type intramolecular motions. Our trajectory surface-hopping study confirms, however, that the unusually slow dissociation rate of highly excited ethyl radicals observed by Gilbert *et al.*[4] cannot arise from a slow multi-step electronically excited state deactivation, but must arise from slow dissociation on the ground state surface. The observed dissociation rates of both 2-propyl[5] and *tert*-butyl[6] radicals following electronic excitation are also significantly slower than predicted by RRKM theory as in ethyl radical, but for those alkyl radicals the mechanism producing unusually long-lived radicals is not yet clear.

We also inspected the dynamics near the seam of conical intersection to provide a qualitative picture of the mechanism that determines the branching ratio of the competing dissociation channels. All trajectories evolve from the Franck-Condon region in the $3s$ Rydberg excited state towards the minimum on the crossing seam that resembles the nonclassical (C_{2v}) bridged structure of ethyl radical, see Fig. 3.1. We find that trajectories with geometries near the MXS that have a larger C-H distance for the migrating hydrogen atom

preferentially dissociate adiabatically. Comparing those geometries to that of the MXS, we find that distance from the center of the C-C bond along the z-axis (C_2-axis) to the migrating hydrogen atom is considerably smaller for the MXS. At longer distances along this coordinate the coupling between the two electronic states becomes smaller and the probability of a surface hop becomes negligible. All surface hops occur in the vicinity of the MXS. In an attempt to understand the branching ratio between nonadiabatic dissociation and unimolecular dissociation following surface hopping, we consider an alternative partitioning scheme of the trajectories that comes from inspecting the dynamics near the seam of conical intersection instead of their dissociation lifetime τ_1 and τ_2. We inspect the orbitals of ethyl radical and the z-axis component of the gradient of the migration hydrogen atoms at the excited state geometry where the last surface hop occurs for all trajectories at the SA–MCSCF level of theory. We find that the sign of the z-axis component of the gradient on migrating hydrogen atoms corresponds to a formally repulsive or attractive ground electronic state at the geometries where the surface hop occurs. For the fast hydrogen atoms with the short lifetime τ_1, 73% of all trajectories hop onto a repulsive ground state surface. For the slow hydrogen atoms produced by unimolecular dissociation with the longer lifetime τ_2 we find that 74% of all trajectories hop onto a repulsive ground state surface. Clearly, the lifetime with respect to C-H bond fission does not correlate with a formally repulsive or attractive ground state surface at the last surface hop before dissociation nor does it correlate with the kinetic energy release. In the fewest switches algorithm,[44] the component of the velocity in direction of the nonadiabatic coupling vector is adjusted during the hop and it is the momentum of the migrating hydrogen atom that appears to primarily determine the fate of the ethyl radical.

The hydrogen atom initially migrating from the methyl group towards the MXS in the 3sRydberg state could lead to one or more 1,2-hydrogen atom shifts on the excited state surface in ethyl before dissociation. In the ground electronic state, the barrier for 1,2-hydrogen atom shifts at the MR–CISD level of theory of 43.7 kcal/mol is only slightly higher than the transition state for C-H bond fission, which could lead to a competition between 1,2-hydrogen shifts and unimolecular dissociation for highly energized ground state radicals. For trajectories in the ensemble that dissociate on the ground state surface with the longer lifetime τ_2, we find an average of 2.46 H-atom shifts in each trajectory before dissociation, of which half occur in the ex-

cited electronic state before surface hopping. In the trajectories that dissociate promptly after surface hopping with the shorter lifetime τ_1 with respect to C-H bond fission, we find only an average of 1.37 H-atom shifts in each trajectory. Despite this competition between 1,2-hydrogen atom shifts and C-H bond fission, our simulations predict that 99% of the dissociating hydrogen atoms originate from the methyl group in agreement with the site selective loss of hydrogen atoms that was observed in photodissociation experiments[4,9,12,40] of CH_3CD_2. In our simulations, it is almost exclusively the hydrogen atom initially migrating in the $3s$ Rydberg state towards the MXS that ultimately dissociates. This appears to be a dynamical effect that our trajectory calculations of ethyl radical unimolecular dissociation starting with a microcanonical ensemble of initial states on the ground state surface could not predict.

B. Non-statistical Dissociation

Intrinsic RRKM behavior is expected if all the classical motion throughout phase space is sufficiently chaotic.[45] In classical nonlinear systems, for example, a system of oscillators with small inter-oscillator coupling, the KAM theorem[46] states that, while an increase in energy or an increase in the coupling leads to a transition from regular, periodic motion to chaotic trajectories in phase space, quasi-periodic trajectories can survive well into the chaotic regime. A quantum analog, applicable to molecular dynamics, has also been proven.[47]

Experimental support for quasiperiodic trajectories in the dynamics of molecules has been rare, with the best evidence coming from the molecular spectroscopy of several small molecules, acetylene,[48] and formyl fluoride,[49] with the discrete bands embedded in a continuum above the dissociation limit of HFCO to HF+CO being the best studied example.[49] Quasiperiodic trajectories in phase space correspond to quasi-bound resonances in the frequency domain. Hose and Taylor[50] have proposed that the quasi-bound resonances embedded in a continuum are extreme motion states for which the coupling to the remaining degrees of freedom in a molecule is weak. The vibrational wavefunction of an extreme motion state is characterized by a large number of quanta in a single degree of freedom, leading to vanishingly small overlap integrals with other vibrational states. A parallel argument by Brumer and Shapiro[51] explains the weak coupling to extreme motion states

by the adiabatic separation of fast and slow motions. Classical dynamics on a six-dimensional analytic potential surface for formyl fluoride[52–54] suggest state-specific chemistry, with trajectories corresponding to the spectroscopically observed resonances (embedded in a dissociative continuum) displaying longer lifetimes with respect to dissociation to HF+CO. Quantum dynamics calculations confirm the results from classical dynamics.[55]

While there are convincing, if not numerous, examples of the spectroscopic consequences[56] of quasiperiodic orbits or extreme motion states, experiments in which a significant impact on chemical kinetics is claimed have not been reported for strongly bound systems with more than three atoms.[57,58] It is surprising that the seven-atom radical, C_2H_5, should show any nonchaotic behavior at an energy so far above its dissociation limit. The classical trajectories nevertheless indicate that intrinsically non-RRKM behavior is plausible, although the fraction of long-lived radicals will depend on method of excitation, there being no guarantee that any particular excitation scheme in an experiment will produce the same ensemble of initial states as in the simulation. Moreover, while Bunker and Hase[45] already indicated three decades ago that intrinsically non-RRKM behavior does not necessarily affect rate constants in the high-pressure limit, they predicted that fall-off behavior would be strongly impacted. In the present case, the anomalous dissociation rates[4] for ethyl radical, $\sim 10^7$ instead of 10^{12} s^{-1}, fall in the same range as gas-phase collision frequencies, making large fall-off effects probable.

The objective of this study is to establish whether or not the dissociation rate of the ethyl radical can be correlated to the degree of ergodicity in classical trajectories. For of a given molecule, the dynamics can be either predominantly regular or predominantly chaotic, depending on, among several factors, the degree of excitation. The former regime, dynamics at low energies, at the limit of a completely integrable Hamiltonian, generates discrete, sparse vibrational spectra with narrow linewidths. The latter regime, dynamics at high energies, at its limit, produces the chaotic motion required for the equipartition underlying statistical theories of rates and equilibria.[7,59] In the frequency domain, spectra in this regime are continuous. For a given molecule there is necessarily a transition from regular to chaotic dynamics as the energy is increased. Figure 3.14 shows the spectrum obtained from the Fourier transform of the ensemble averaged velocity autocorrelation function for ethyl radical at 120 kcal/mol excitation energy. The spectrum consist of both broad an unstructured bands that arise from chaotic dynamics, while

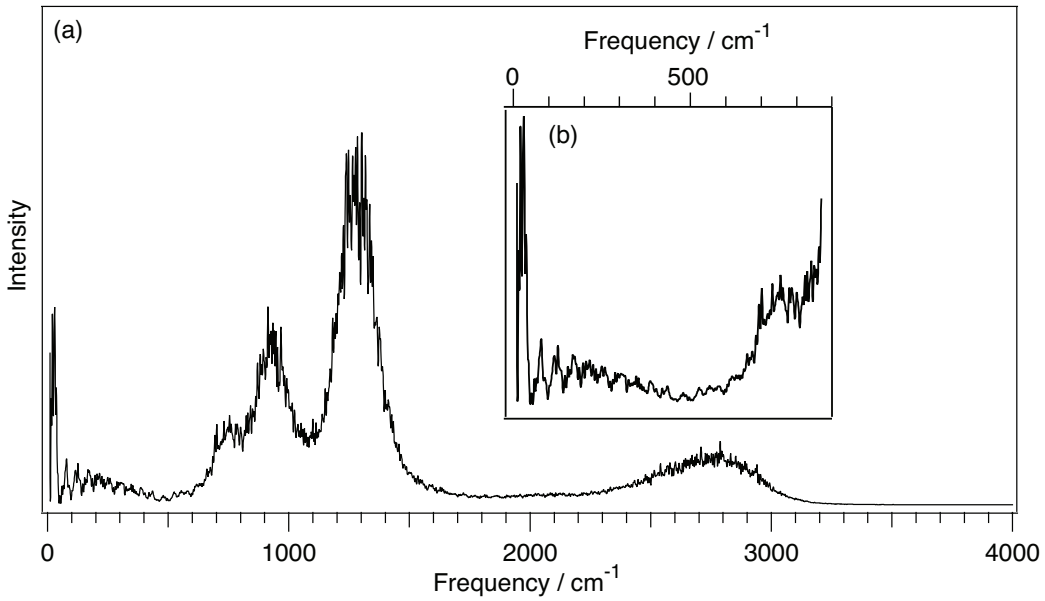

Figure 3.14: (a) Spectrum obtained from the Fourier transform of the ensemble averaged velocity autocorrelation function. (b) Low frequency part of the spectrum revealing sharp peaks arising from the resonance trappings.

at frequencies of less than 1000 cm^{-1}, sharp bands arise from the trajectories that show extended episodes of regular-type intramolecular motions, indicating ordered regions submerged in a sea of chaos.

In classical Hamiltonian mechanics, the N-dimensional invariant tori in $2N$-dimensional phase space, on whose surfaces trajectories are confined when the Hamiltonian is completely integrable, are distorted but not destroyed when small perturbations, i.e. couplings, are introduced, as shown by the Kolmogorov-Arnold-Moser (KAM) theorem.[46] Increasingly large couplings, however, do destroy the invariant tori, the last remnants[60] of which, termed cantori, have been proposed by several groups[60–65] to function as dynamical bottlenecks for flows through phase space. Numerical studies have found, at least for two- and three-dimensional Hamiltonian systems, that remnants of invariant tori can persist to very high excitation energies.[61,62] Karney[66] in a numerical study first found trajectories that are sticky in the vicinity of invariant tori, meaning that trajectories tended to stay in that vicinity for longer than expected times, a result which was later justified by Perry and Wiggins[67] with perturbation theory. Figure 3.15 shows the sum of the spectrograms taken from one of the long-lived trajectories. This trajectory "sticks" in or near a 3:2 resonance for a time t_{lock} that sensitively

changes as a function of a small initial random displacement δ in phase-space, a result also found for other invariant sets in phase space, not only tori.[68–73] Importantly, the stickiness justified by perturbation theory can even occur in systems with high dimensionality.[67]

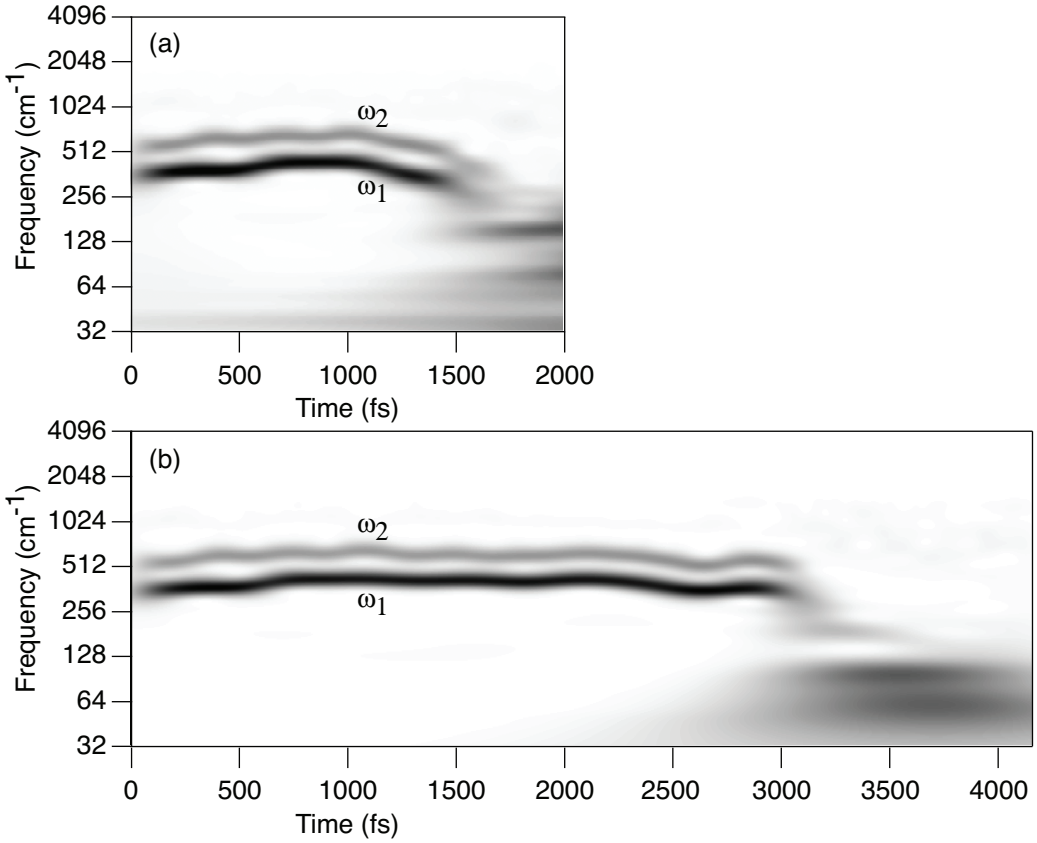

Figure 3.15: (a) Sum of the spectrograms from a trajectory in that is trapped in or near a 3:2 resonance for $t_{\text{lock}} = 1570$ fs. (b) Sum of the spectrograms obtained from the trajectory shown in (a) with an small initial displacement of $||\delta|| = 10^{-5}$ a.u. revealing an extended resonance trapping for $t_{\text{lock}} = 2935$ fs.

The challenge for this study is two-fold, physical and methodological. Physically, it is not at all clear whether or not C_2H_5, a seven-atomic molecule with 21 Cartesian degrees-of-freedom, can show any non-statistical behavior at 120 kcal/mol excitation energy. Even if it were to display non-statistical behavior, the methodological problem arises that the visualization and analysis methods[74] used in two- and three-dimensional Hamiltonian systems scale up to higher dimensions poorly or not at all. Experimentally, Gilbert *et al.*[4] observed anomalously long lifetimes for dissociation of C_2H_5 to C_2H_4+H,

which has driven a search for solutions to both the physical and methodological challenges.

Classical trajectory methods on the full-dimensional Born-Oppenheimer surface of C_2H_5 were chosen for this study in part for practical reasons, but nevertheless justified by previous reports[75] which indicated that the onset of stochasticity was not significantly different in classical versus quantum dynamics[76–78] studies on the Hénon-Heiles[79] potential. Perhaps more significantly, quasibound resonances in the continuum, experimentally observed for formyl fluoride above its dissociation limit to CO and HF,[49] were examined subsequently by both classical[52–54] and quantum dynamics simulations[55,80] whose results turned out to be similar. These quasibound resonances have been seen in several other tri- and tetra-atomic molecules,[48,81] as well as weakly-bound atom-diatom complexes,[82] but their correlation to dissociation lifetime has not been investigated. The quasibound resonances would be the spectroscopic analog to trajectories with quasiperiodic behavior, so their observation in other, albeit smaller, molecules above their dissociation limits, and their simulation in both classical and quantum dynamics studies suggest that classical trajectories may be adequate for the C_2H_5 problem at hand.

Accordingly, we postulate that the anomalously long (up to 10^5 times longer than RRKM estimates) dissociation lifetime of ethyl radical, observed independently by Gilbert *et al.*,[4] can be explained by dynamical trapping in phase space.[8,83–85] The hypothesis necessarily implies the long-time persistence or recurrence of periodic or quasiperiodic motion during the time evolution of the energized molecule. Having run a set of trajectories on a high-quality potential energy surface, we were faced with the question as to how one finds and quantifies nonergodicity in a trajectory.

The standard tools for visual identification[74] of nonergodicity, Poincaré surfaces of section and return maps, for example, become problematic at more than three degrees-of-freedom. The accepted quantitative metrics for the presence (or absence) of chaos are the Kolmogorov-Sinai (KS) entropy and the largest Lyapunov exponent. The KS entropy can be defined as the time derivative of the Shannon information entropy[86] (formally equivalent to the thermodynamic entropy except for multiplication by Boltzmanns constant) along a particular path through phase space.[87] Trajectories are classified in two regimes: KS entropy is positive for chaotic and zero for regular systems. Similarly, the Lyapunov exponent represents the average exponential diver-

gence of two trajectories that start out infinitesimally displaced from each other. While these two metrics theoretically provide a quantitative basis for classification of the trajectories generated in the study of ethyl dissociations, they suffer from practical limitations.

Accessible algorithms compute the KS entropy from the Lyapunov exponents, according to Pesins theorem.[88] In turn, the computation of Lyapunov exponents suffers from both practical and theoretical problems. Practically, there are as many Lyapunov exponents as there are dimensions in phase space, and one must test the degree and direction of displacement of initial conditions. Our fortunate case, in which the displacement vector reorients itself quickly along the most unstable direction, cannot be assumed generally. While the tests can be done for one trajectory at a time, the systematic search for large numbers of trajectories is inconvenient. In theory, a further problem with Lyapunov exponents comes because they are asymptotic quantities. For short time segments and high dimensionality, there is no guarantee that they are converged or that one has found the leading (largest) exponent. The local (or finite time) Lyapunov exponents were nevertheless used by Rice[89] as an indicator for intramolecular vibrational energy flow in a two-dimensional model potential, and by Kandrup *et al.*[35–37] as an indicator correlating to dissociation, termed escape in their papers, on model two- and three-dimensional potential surfaces.

In Sec. II.B, we reported that a significant fraction within an ensemble of trajectories simulating the ethyl radical dissociation displayed dissociation lifetimes far exceeding the ~ 1 ps RRKM lifetime. A faster, more automatic, metric is needed to scan through large ensembles of data for indications of nonergodic dynamical behavior. Siopis *et al.*[35] propose the orbital complexity, defined in Eq. 2.11, as just such a metric. Their formulation is based on a short-time Fourier transform instead of the wavelet transform used in the present work, and therefore can suffer from high frequency artifacts generated by what amounts to a suboptimal apodization. Nevertheless, the orbital complexity was shown to correlate well to the largest local Lyapunov exponents for trajectories on a model three-dimensional potential.

Qualitatively, the orbital complexity is the number of frequency components in a Fourier analysis needed to capture a set fraction, usually 90%, of the spectral power in a time-frequency plot. The correlation of the instantaneous wavelet-based orbital complexity to the largest local Lyapunov exponents, depicted for one trajectory in Fig. 3.11, was checked. As is evident

from the comparison, the two metrics track each other quite well. Given the methodological limitations on the Lyapunov exponents, one may venture to presume that the small deviations between the two metrics are due to deficiencies in the Lyapunov exponents and not the orbital complexities. Moreover, the relationship between Lyapunov exponents and the KS entropy ensures that the orbital complexities can be taken as a surrogate for that latter quantity as well. As a matter of computational convenience, it should be noted that the computation of the orbital complexity for a given trajectory requires only that trajectory itself and no further replicate runs. As one would expect from the definition of the orbital complexity, the visually identified episodes of quasiperiodic motion in the selected trajectories correspond to time segments in which the orbital complexity is low.

Lastly, a histogram can be constructed from the distribution of orbital complexities along the trajectory up until, but not including, dissociation. The moments of the distribution of orbital complexities along a given trajectory can be plotted against the time for dissociation for that same trajectory. The plots in Fig. 3.13 of the first moment (the mean) and the third moment (the skew) of the distributions against the dissociation time, both show clear correlations. Those trajectories for which the average orbital complexity is low are also the trajectories with the longest time for dissociation. Similarly, those trajectories for which the distribution of orbital complexities is asymmetrically skewed towards low complexity are also the ones with the longest lifetimes. In principle, the orbital complexity, can be used either as a time-dependent scalar metric, or through the moments of its distribution, to classify trajectories in a fully automated fashion. The method is fast, and conveniently flags those trajectories or portions of trajectories that show chemically interesting dynamical behavior. The direct connection to the visualization provides then a tool to identify the collective molecular motions of the atoms associated with dynamical bottlenecks which may be otherwise difficult to recognize directly from the individual Cartesian displacements when the system has high dimensionality.

IV. Summary

Direct *ab initio* molecular dynamics using the trajectory surface hopping method with Tully's fewest switches simulates the photodissociation dynamics of the ethyl radical following electronic excitation to the $\widetilde{A}$-state. From

an ensemble of trajectories we obtain a short excited state lifetime of the ethyl radical of ~ 20 fs. Analysis of the dissociation lifetime distribution allows separation of the calculated recoil energy distribution into components that arise from fast nonadiabatic dissociation and unimolecular dissociation of hot ground state ethyl radicals following surface hopping. The dominant dissociation channel is nonadiabatic dissociation accounting for 68% of all trajectories at the MR–CISD level of theory, which produce ground state ethylene and fast hydrogen atoms with an anisotropic angular distribution. These dissociation channels are in competition with adiabatic dissociation resulting in electronically excited state ethylene and H, a dissociation channel that has not yet been experimentally observed. The branching ratio between adiabatic and nonadiabatic dissociation pathways depends strongly on the quality of the potential energy surfaces with only 15% of all trajectories dissociating adiabatically at the MR–CISD level of theory.

The calculated excited state lifetime and the energy disposal in the photofragments is consistent with previous experiments and we propose that a strictly nonadiabatic mechanism accounts for nonradiative decay in the ethyl radical. Our trajectory surface hopping study also confirms that the unusually slow dissociation rate of highly excited ethyl radicals cannot arise from a slow multi-step electronically excited state deactivation, but must arise from slow dissociation on the ground state surface.

We introduced the normalized instantaneous orbital complexity, a time-dependent scalar metric based on the time-frequency decomposition of classical trajectories using wavelets, which we use to quantify the extent of nonergodic behavior in the unimolecular dissociation of the ethyl radical. This orbital complexity correlates linearly to the conventionally accepted, but computationally more difficult, largest local Lyapunov exponent. The episodes of quasiperiodic behavior in trajectories of highly energized ethyl radicals with lifetimes far exceeding the ~ 1 ps RRKM lifetime correspond to resonance trappings displaying large-amplitude low-frequency excursions of the atoms, predominantly a counter-rotation of the methyl and methylene group revealed using wavelet filtering. The unusually long lifetime can be explained by dynamical trapping of trajectories in phase space, during which the normalized instantaneous orbital complexity is very small and remains nearly constant indicating quasiperiodic behavior of those trajectories. Moreover, the moments of the distribution of instantaneous orbital complexities correlate well enough to dissociation lifetime in the ethyl radical to serve

as a predictive tool for classification of trajectories even before they end in dissociation and confirm the hypothesis that the long-lived trajectories are less ergodic.

Further theoretical studies on the photodissociation of other alkyl radicals that also show unusually slow dissociation rates are potentially a key complement to our simulations and could provide more insight into these unusual photofragmentation dynamics.

Bibliography

[1]J. Warnatz, in *Combustion Chemistry*, edited by W. G. Jr., Springer, New York, 1984.

[2]M. Hanning-Lee, N. Green, M. Pilling, and S. Robertson, J. Phys. Chem. **97**, 860 (1993).

[3]Y. Feng, J. Niiranen, A. Bencsura, V. Knyazev, D. Gutmann, and W. Tsang, J. Phys. Chem. **97**, 871 (1993).

[4]T. Gilbert, T. L. Grebner, I. Fischer, and P. Chen, J. Chem. Phys. **110**, 5485 (1999).

[5]B. Noller and I. Fischer, J. Chem. Phys. **126**, 144302 (2007).

[6]M. Zierhut, W. Roth, and I. Fischer, J. Phys. Chem. A **108**, 8125 (2004).

[7]T. Baer and W. L. Hase, *Unimolecular Reaction Dynamics*, Oxford University Press, New York, 1996.

[8]M. Toda, T. Komatsuzaki, T. Konishi, R. Berry, and S. Rice, *Geometrical Structures of Phase Space in Multidimensional Chaos: Applications to Chemical Reaction Dynamics in Complex Systems*, volume 130 of *Advances in Chemical Physics*, John Wiley & Sons, Hoboken, New Jersey, 2005.

[9]G. Amaral, K. Xu, and J. Zhang, J. Chem. Phys. **114**, 5164 (2001).

[10]Z. Min, R. Quandt, and R. Bersohn, Chem. Phys. Lett. **296**, 372 (1998).

[11]J. L. Brum, S. Deshmukh, and B. Koplitz, J. Chem. Phys. **93**, 7504 (1990).

[12]J. Brum, S. Deshmukh, and B. Koplitz, J. Chem. Phys. **95**, 2200 (1991).

[13]R. Quandt, X. Wang, Z. Min, H. Kim, and R. Bersohn, J. Chem. Phys. A. **102**, 6063 (1998).

[14]G. Johnston, S. Satyapal, R. Bersohn, and B. Katz, J. Chem. Phys. **92**, 206 (1990).

[15]W. L. Hase, R. J. Wolf, and C. S. Sloane, J. Chem. Phys. **71**, 2911 (1979).

[16]W. L. Hase and D. G. Buckowski, J. Comput. Chem. **3**, 335 (1982).

[17]A. Sevin, H. T. Yu, and E. M. Evleth, J. Mol. Struct.: THEOCHEM **104**, 163 (1983).

[18]E. M. Evleth, H. Z. Cao, E. Kassab, and A. Sevin, Chem. Phys. Lett. **109**, 45 (1984).

[19]A. S. Zyubin, A. M. Mebel, and S. H. Lin, Chem. Phys. Letters **323**, 441 (2000).

[20]S. Matsika and D. R. Yarkony, J. Chem. Phys. **117**, 6907 (2002).

[21]W. L. Hase, G. Mrowka, R. Brudzynski, and C. Sloane, J. Chem. Phys. **69**, 3548 (1978).

[22]H. S. Taylor, Phys. Scripta **40**, 373 (1989).

[23]C. Chandre, S. Wiggins, and T. Uzer, Physica D **181**, 171 (2003).

[24]L. Vela-Arevalo and S. Wiggins, Int. J. Bifurcat. Chaos **11**, 1359 (2001).

[25]A. Bach, J. Hostettler, and P. Chen, J. Chem. Phys. **125**, 024304 (2006).

[26]F. Qi, O. Sorkhabi, and A. Suits, J. Chem. Phys. **112**, 10707 (2000).

[27]W. L. Hase, H. B. Schlegel, V. Balbyshev, and M. Page, J. Phys. Chem. **100**, 5354 (1996).

[28]A. Bach, J. Hostettler, and P. Chen, J. Chem. Phys. **123**, 021101 (2005).

[29]J. Munk, P. Pagsberg, E. Ratajczak, and A. Sillesen, J. Phys. Chem. **90**, 2752 (1986).

[30]M. Zierhut, B. Noller, T. Schultz, and I. Fischer, J. Chem. Phys. **122**, 094302 (2005).

[31]W. Lang and K. Forinash, Am. J. Phys. **66**, 794 (1998).

[32]S. Davis, D. Uy, and D. J. Nesbitt, J. Chem. Phys. **112**, 1823 (2000).

[33]T. Sears, P. Johnson, P. Lin, and S. Oatis, J. Chem. Phys. **104**, 781 (1996).

[34]T. Sears, P. Johnson, and J. Wang, J. Chem. Phys. **111**, 9213 (1999).

[35]C. Siopis, B. L. Eckstein, and H. E. Kandrup, Ann. Ny. Acad. Sci. **867**, 41 (1998).

[36]H. E. Kandrup, Phys. Rev. E. **56**, 2722 (1997).

[37]H. E. Kandrup, C. Siopis, G. Contopoulos, and R. Dvorak, Chaos **9**, 381 (1999).

[38]C. Amitrano and R. Berry, Phys. Rev. E. **47**, 3158 (1993).

[39]R. Hinde and R. Berry, J. Chem. Phys. **99**, 2942 (1993).

[40]J. L. Brum, S. Deshmukh, Z. Wang, and B. Koplitz, J. Chem. Phys. **98**, 1178 (1993).

[41]W. L. Hase, R. J. Wolf, and C. S. Sloane, J. Chem. Phys. **76**, 2771 (1982).

[42]K. Swamy and W. L. Hase, J. Phys. Chem. **87**, 4715 (1983).

[43]W. L. Hase, D. Ludlow, R. Wolf, and T. Schlick, J. Phys. Chem. **85**, 958 (1981).

[44]J. Tully, J. Chem. Phys. **93**, 1061 (1990).

[45]D. Bunker and W. L. Hase, J. Phys. Chem. **59**, 4621 (1973).

[46]J. Moser, *Stable and Random Motions in Dynamical Systems*, Princeton University Press, Princeton NJ, 1973.

[47]G. Hose, H. Taylor, and Y. Bai, J. Chem. Phys. **80**, 4363 (1984).

[48]M. Jacobson, J. O'Brien, and R. Field, J. Chem. Phys. **109**, 3831 (1998).

[49]Y. Choi and C. Moore, J. Chem. Phys. **94**, 5414 (1991).

[50]G. Hose and H. Taylor, Chem. Phys. **84**, 375 (1984).

[51]P. Brumer and M. Shapiro, Adv. Chem. Phys. **70**, 365 (1988).

[52]T. Yamamoto and S. Kato, J. Chem. Phys. **107**, 6114 (1997).

[53]F. Budenholzer and T. Yu, J. Phys. Chem. A. **102**, 947 (1998).

[54]S. Anand and H. B. Schlegel, J. Chem. Phys. A. **106**, 11623 (2002).

[55]T. Yamamoto and S. Kato, J. Chem. Phys. **112**, 8006 (2000).

[56]H. S. Taylor, Adv. Ser. Phys. Chem. **4**, 1073 (1995).

[57]R. Schinke, H. Keller, H. Flöthmann, M. Stumpf, C. Beck, D. Mordaunt, and A. Dobbyn, Adv. Chem. Phys. **101**, 745 (1997).

[58]J. Troe and V. Ushakov, J. Chem. Phys. **115**, 3621 (2001).

[59]B. Widom, *Statistical Mechanics, A Concise Introduction for Chemists*, Cambridge University Press, Cambridge, |2002|.

[60]R. B. Shirts and W. P. Reinhardt, J. Chem. Phys. **77**, 5204 (1982).

[61]J. D. Davis and S. Gray, J. Chem. Phys. **84**, 5389 (1986).

[62]J. D. Davis, J. Chem. Phys. **83**, 1016 (1985).

[63]M. Zhao and S. Rice, J. Chem. Phys. **96**, 6654 (1992).

[64]R. MacKay, J. Meiss, and I. Percival, Physica D **13**, 55 (1984).

[65]D. Bensimon and L. Kadanoff, Physica D **13**, 82 (1984).

[66]C. Karney, Physica D **8**, 360 (1983).

[67]A. Perry and S. Wiggins, Physica D **71**, 102 (1994).

[68]J. Zhou, L. Zhou, and Y. Sun, Chin. Phys. Lett. **19**, 1254 (2002).

[69]Y. Sun, L. Zhou, and J. Zhou, Celest. Mech. Dyn. Astron. **92**, 257 (2005).

[70]J. Meiss and E. Ott, Phys. Rev. Lett. **55**, 2741 (1985).

[71]G. Contopoulos, N. Voglis, C. Efthymiopoulos, C. Froeschlé, R. Gonczi, E. Lega, R. Dvorak, and E. Lohinger, Celest. Mech. Dyn. Astron. **67**, 293 (1997).

[72]K. Tsiganis, A. Anastasiadis, and H. Varvoglis, Chaos, Solitons and Fractals **11**, 2281 (2000).

[73]K. Tsiganis, H. Varvoglis, and J. Hadjidemetriou, Icarus **146**, 240 (2000).

[74]T. Denton and G. Diamond, Comput. Biol. Med. **21**, 243 (1991).

[75]D. Oxtoby and S. Rice, J. Chem. Phys. **65**, 1676 (1976).

[76]S. Nordholm and S. Rice, J. Chem. Phys. **61**, 203 (1974).

[77]S. Nordholm and S. Rice, J. Chem. Phys. **61**, 768 (1974).

[78]S. Nordholm and S. Rice, J. Chem. Phys. **62**, 157 (1975).

[79]M. Hénon and C. Heiles, Astron. J. **69**, 73 (1964).

[80]G. Pasin, F. Gatti, C. Iung, and H. Meyer, J. Chem. Phys. **124**, 194304 (2006).

[81]A. Geers, J. Kappert, F. Temps, and J. Wiebrecht, J. Chem. Phys. **101**, 3634 (1994).

[82]S. Farantos and J. Tennyson, J. Chem. Phys. **84**, 6210 (1986).

[83]T. Uzer, C. Jaffé, J. Palacián, P. Yanguas, and S. Wiggins, Nonlinearity **15**, 957 (2002).

[84]H. Waalkens, A. Burbanks, and S. Wiggins, Phys. Rev. Lett. **95**, 084301 (2005).

[85]R. Skodje and X. Yang, Int. Rev. Phys. Chem. **23**, 253 (2004).

[86]C. Shannon, The Bell Systems Technical Journal **27**, 379 (1948).

[87]R. Frigg, Brit. J. Phil. Soc. **55**, 411 (2004).

[88]Y. Pesin, Russ. Math. Surveys **32**, 55 (1977).

[89]H. Tang, S. Jang, M. Zhao, and S. Rice, Chem. Phys. Lett. **285**, 143 (1998).

Chapter 4

The Allyl Radical

I. Introduction

The allyl radical, C_3H_5, is at the moment one of the best understood polyatomic radicals. It is the simplest π-conjugated hydrocarbon radical and servers as a model system for a whole class of molecules. Small hydrocarbon radicals play a key role in combustion chemistry, in hydrocarbon crackers and in certain regions of the atmosphere as well as in interstellar space. All hydrocarbons with a framework of three carbon atoms are assumed to be precursors in the formation of polycyclic aromatic hydrocarbons and soot.[1] Allyl is also an important intermediate in propane-, butane- and acetylene-rich flames.[2] Kinetic modeling of combustion processes is very sensitive to the rates of reactions that produce or consume hydrogen atoms[3] and therefore information about the nature of the dissociation dynamics of the allyl radical is important.

A prerequisite to energize allyl in photodissociation dynamics experiments is the presence of an electronically excited state and a detailed understanding of the vibronic structure in the energy range of interest. Currie and Ramsay[4] first observed a weak and diffuse band system of the allyl radical in the near ultraviolet assigned to a transition between the ground and the first excited ($\widetilde{A}\ ^2B_1$) state,[5–7] which was predicted theoretically by Longuet-Higgins and Pople already in 1955.[8] Callear and Lee later found an intense band system in the ultraviolet with sharp bands and an underlying continuous absorption after flash photolysis of allylic compounds in the gas phase,[9,10] which we recently partially reassigned to transitions to the $3s$ ($\widetilde{B}\ ^2A_1$) and $3p$ Rydberg excited states.[11,12] We probed the vibronic structure of jet-cooled allyl radi-

cals using a range of spectroscopic methods including photofragment action spectroscopy to reveal the band system of the first excited ($\widetilde{A}\ ^2B_1$) state.[7] Analysis of the vibronic structure in the ultraviolet obtained by resonant multiphoton ionization combined with high level *ab initio* calculations and results and simulations of pulsed-field-ionization zero-kinetic-energy photoelectron spectra allowed for the first time to experimentally derive the energetic ordering of the $3p$ Rydberg states of the allyl radical.[11,12]

The dissociation dynamics of the allyl radical has been studied extensively.[6,13–21] Allyl is stable in the electronic ground state but becomes reactive upon electronic excitation to the first valence excited state[4–7] and the manifold of the $3s$ and $3p$ Rydberg states[12] with excited state lifetimes ranging from < 5 to 22 ps.[6,18] The most favorable reaction channel[16] in unimolecular dissociation dynamics of allyl is hydrogen loss forming predominantly allene over a barrier of 60 kcal/mol,[22] while cyclopropene or propyne appear only as minor product channels.[15,23]

The allyl radical is a model system in many respects, but the consequences of ultrafast dynamics enabled by conical intersections[7,24,25] following photoexcitation in allyl are not well known. Here, we report a simulation of the ultrafast photochemical deactivation pathways of the $\widetilde{A}$-state allyl radical using direct *ab initio* semiclassical molecular dynamics.[26] Analysis of the electronically nonadiabatic dynamics provides not only branching ratios for the different deactivation pathways producing hot ground state radicals, but also reveals the nuclear motions near the conical intersections giving mechanistic insight into the photo-induced cyclization of the allyl radical to the cyclopropyl radical. Time-resolved photoionization on the nanosecond timescale of the hydrogen atom photoproduct provides information on the rate of unimolecular decomposition of allyl in the ground electronic state.

We also exploit the partially rotationally resolved spectrum of the allyl $\widetilde{B}$-state to investigate the angular-momentum-selected dissociation dynamics.[27] The measured rate constants and kinetic energy release remain essentially unchanged for dissociation of rotationally cold versus warm allyl radicals and are consistent with allene and hydrogen atoms as primary photoproducts suggesting that the nature of the unimolecular dissociation dynamics does not change with increasing excitation energy.

II. Results and Discussion

A. The $\widetilde{A}$-State Photochemical Deactivation Pathways

Currie and Ramsay first found a weak band system of the allyl radical in the spectral range between 370-410 nm, which they assigned to a transition between the ground and the first excited ($\widetilde{A}\ ^2B_1$) state.[4] The diffuse character of the band system was attributed to lifetime broadening arising from predissociation or fast electrocyclization to the cyclopropyl radical.[4–7] Experimental data on this reaction is scarce because of the transient nature of the species involved. Upon irradiation of allyl radicals in an Ar-matrix at 409 nm, Holtzhauer *et al.* detected new infrared bands, which they assigned to cyclopropyl.[28] The photo-induced cyclization of the allyl radical to the cyclopropyl radical is the smallest possible electrocyclic reaction. Longuet-Higgins[29] used a state correlation diagram in 1965 to demonstrate that both conrotatory and disrotatory cyclization are photochemically allowed but thermally forbidden, whereas Woodward and Hoffmann[30] predicted the conrotatory cyclization to be thermally allowed using their frontier orbitals approach. The stereochemical outcome of the electrocyclic reaction, however, has not yet been experimentally determined.

The fundamental nature of this reaction and the role of the allyl radical as a model system for π-conjugation raised interest in the theoretical community. In particular, the excited states served as a benchmark in numerous electronic structure calculations.[7,8,31–35] The ground state transformation of allyl to cyclopropyl has been examined in several theoretical studies and a highly non-symmetric transition state was found.[36–38] A recent CASSCF direct dynamics simulation of the thermal cyclopropyl ring opening found a small preference for the disrotatory pathway,[39] which has been confirmed in a DFT study in He and Ar condensed phase.[40] Among the little information about the photochemistry of allyl is a CASSCF study by Yamaguchi.[41] He explored the $\widetilde{A}$-state potential energy surface (PES) topology and concluded that a near barrier-less transformation to cyclopropyl would be feasible in both disrotatory and conrotatory fashion.

The allyl radical is a model system in many respects, but the consequences of ultrafast dynamics enabled by conical intersections[7,24,25] following photoexcitation in allyl are not well known. Two conical intersections between the first electronically excited state and the ground state have been

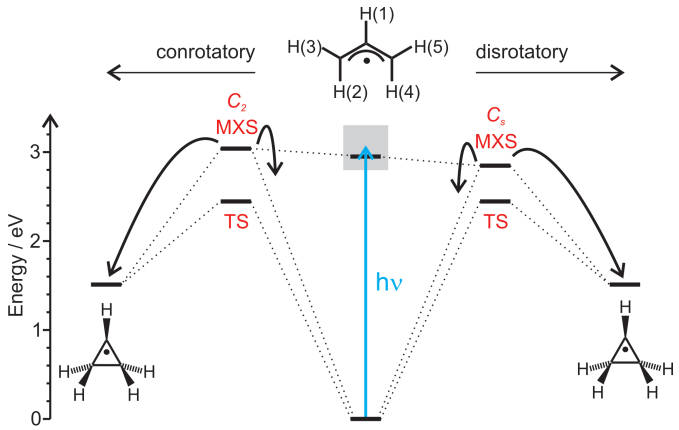

Figure 4.1: Schematic energy level diagram illustrating the photochemical deactivation pathways following electronic excitation of the allyl radical to the $\widetilde{A}$-state. Surface hopping indicated with arrows near the conical intersections generates hot ground state C_3H_5 along the conrotatory and disrotatory pathway.

located,[7,25] one along the disrotatory (C_s) and the other along the conrotatory (C_2) pathway, see Fig. 4.1.

Here, we report the first high-level simulation of the $\widetilde{A}$-state dynamics of the allyl radical focusing on the photochemical deactivation pathways using direct *ab initio* semiclassical molecular dynamics as described in Chapter 2 and Ref. 26. Our trajectory calculations result in an ensemble averaged ex-

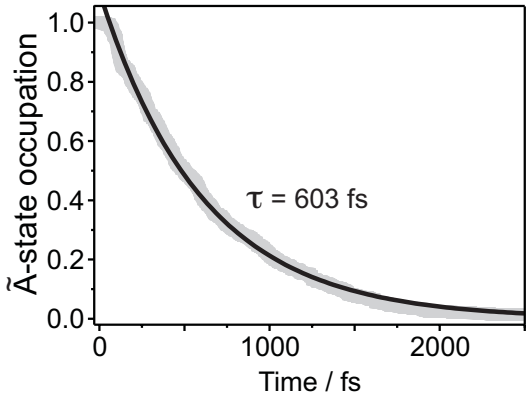

Figure 4.2: Population decay of the $\widetilde{A}$-state allyl radicals obtained from the fraction of trajectories in the excited state using the TFS–DC surface hopping method. See text for details.

citation energy of 3.04 eV for the $\widetilde{A}$-state allyl radical, in good agreement with experiments.[5,7] The SA-2-MCSCF level of theory predicts that the minimum energy structure on the crossing seam (MXS) along the conrotatory pathway lies 0.02 eV above the adiabatic excitation energy of $\widetilde{A}$-state allyl of 2.95 eV, see Fig. 4.1. The MXS along the disrotatory pathway in contrast is located 0.17 eV below the $\widetilde{A}$-state, in agreement with previous calculations.[7,25] From the Franck-Condon region on the $\widetilde{A}$-state PES, the trajectories rapidly evolve towards the conical intersections along either the disrotatory or the conrotatory pathway populating the ground state of C_3H_5 following surface hopping.

The population decay of the $\widetilde{A}$-state allyl radical obtained from an ensemble of 515 trajectories using Tully's fewest-switches[42] method corrected for decoherence effects[43] (TFS–DC) appears in Fig. 4.2. An exponential fit to the population decay gives a time constant $\tau = 603$ fs. The deactivation to ground state allyl radicals occurs with the same time constants for both the conrotatory and the disrotatory pathway, but the trajectories that form cyclopropyl convert slightly slower into the ground state with $\tau = 771$ fs. A time-resolved photoelectron spectroscopy experiment[6] found an instrument response function limited lifetime of less than 5 ps and a lifetime of 1 ps was used to fit the rotational contour in the photodissociation experiment,[7] which is slightly longer than our theoretical prediction. The similar lifetimes observed experimentally and predicted by our trajectory calculations suggests that a nonadiabatic mechanism is important in the nonradiative decay of $\widetilde{A}$-state allyl.

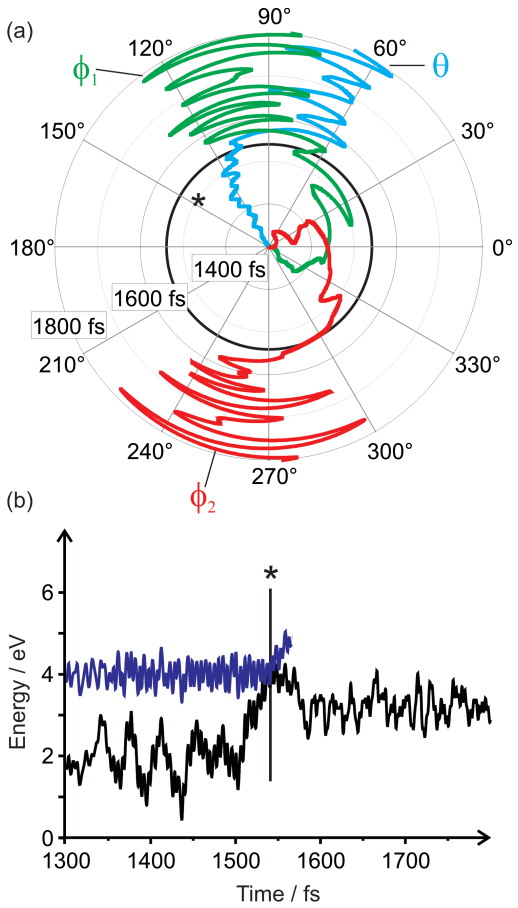

Figure 4.3: Time evolution of a representative trajectory forming the cyclopropyl radical along the disrotatory pathway with surface hops (*). (a) Plot of the CCC-bond angle θ, the H(2)–CCC (ϕ_1) and the H(4)–CCC (ϕ_2) dihedral angles in the allyl radical. (b) Adiabatic potential energy profiles of the $\widetilde{X}$ and $\widetilde{A}$-states relative to ground state allyl.

Our analysis of the trajectories focuses on two key features of the electronically nonadiabatic dynamics. We calculate the branching ratio between disrotatory and conrotatory deactivation pathways by monitoring the rota-

tion of the two methylene groups in each trajectory as a function of time in the vicinity of the surface hops using the H–CCC dihedral angles in allyl. We also determine the yield of the cyclopropyl radical formation by monitoring the CCC bond angle in each trajectory.

Figure 4.3 shows the time evolution of these geometric parameters for a randomly selected trajectory visualizing the nuclear motions near the conical intersection. In this trajectory, the CCC bond angle θ rapidly decreases to $\sim 60°$ following surface hopping indicating ring closure to the cyclopropyl radical. This trajectory follows the disrotatory pathway as determined by the values of the two HCCC dihedral angles at the time of the surface hop. The terminal methylene groups rotate near synchronously in this trajectory, in contrast to the nonconcerted ring opening mechanism of cyclopropyl predicted on the ground state surface[39] that proceeds via a highly asymmetric transition state located 2.46 eV above ground state allyl. Other trajectories produce hot ground state allyl radicals, as shown in Fig. 4.4. The time evolution of the dihedral angles indicates that this trajectory follows the conrotatory pathway producing a hot ground state allyl radical. The branch-

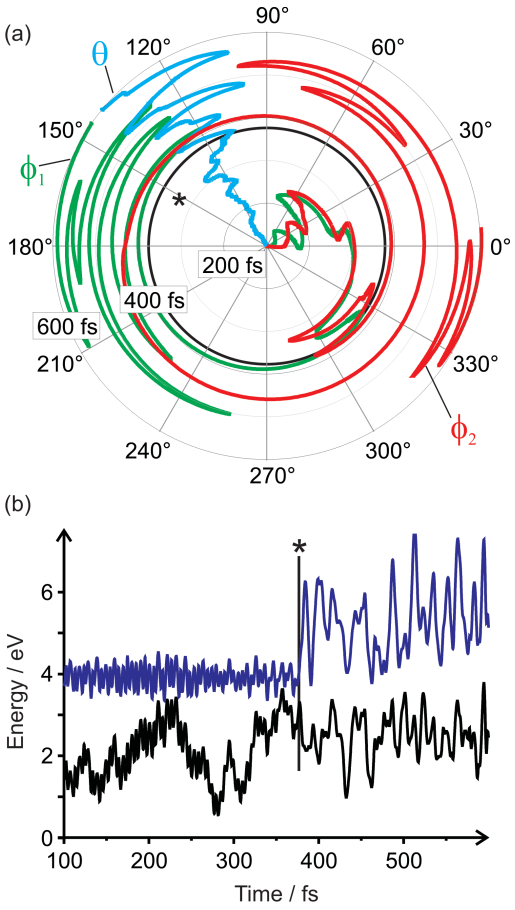

Figure 4.4: Time evolution of a representative trajectory forming allyl along the conrotatory pathway with surface hops (*). (a) Plot of the CCC-bond angle θ, the H(2)–CCC (ϕ_1) and the H(4)–CCC (ϕ_2) dihedral angles in the allyl radical. (b) Adiabatic potential energy profiles of the $\widetilde{X}$ and $\widetilde{A}$-states relative to ground state allyl.

ing ratios for the different deactivation pathways appear in Table 4.1. We find only a very slight preference for the disrotatory pathway accounting for 50.4% of all trajectories. About 8% of all trajectories lead to the cyclopropyl

Table 4.1: Branching ratios (%) of the photochemical deactivation pathways of $\widetilde{A}$-state allyl radicals.

Product	Pathway	Branching (%)
Allyl	Disrotatory	42.6
Allyl	Conrotatory	49.4
Cyclopropyl	Disrotatory	7.8
Cyclopropyl	Conrotatory	0.2

radical, following almost exclusively the disrotatory pathway, see Table 4.1. This selected pathway can be rationalized by the smaller CCC bond angle at nuclear geometries in vicinity of the surface hop along the disrotatory pathway where the MXS has a CCC bond angle of only 97.8° compared to that of 108.7° along the conrotatory pathway, see Fig. 4.5. Furthermore, Yamaguchis results indicate that the topology of the PES is more favorable for cyclopropyl formation along the disrotatory reaction pathway. Subsequent ground state ring opening of the nascent cyclopropyl is feasible too.

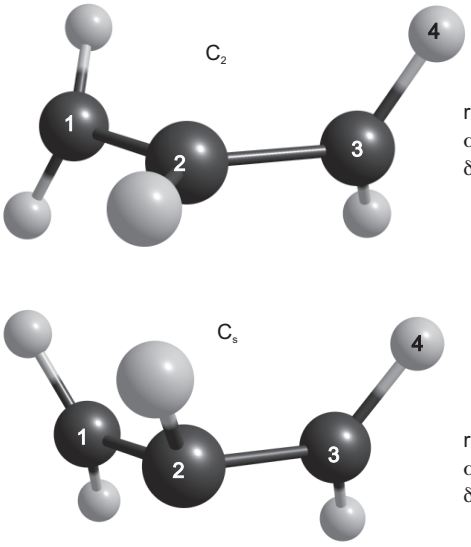

Figure 4.5: Minimum energy structure on the two crossing seams between the $\widetilde{A}$-state and the electronic ground state of the allyl radical.[7]

The remaining 92% of all trajectories produce ground state allyl radicals with vibrational excitation not only in the CCC-bending and CH_2-twisting modes. These hot ground state allyl radicals have sufficient internal energy

to undergo secondary reactions, mainly dissociation to allene and a hydrogen atom, as described in the next section.

B. Unimolecular Dissociation in the Ground Electronic State

The *ab initio* molecular dynamics simulation of the photochemical deactivation pathways described in the previous section predicted a short excited state lifetime for the $\widetilde{A}$-state allyl radical in good agreement with experiment[6,7] and revealed that preferentially highly energized ground state allyl radicals are produced. In a photodissociation study of $\widetilde{A}$-state allyl,[7] we monitored the appearance time of the hydrogen atoms following photoexcitation by time-delayed photoionization of the hydrogen atoms, as depicted in Fig. 4.6. The hydrogen atom photoproducts appear on the nanosecond time

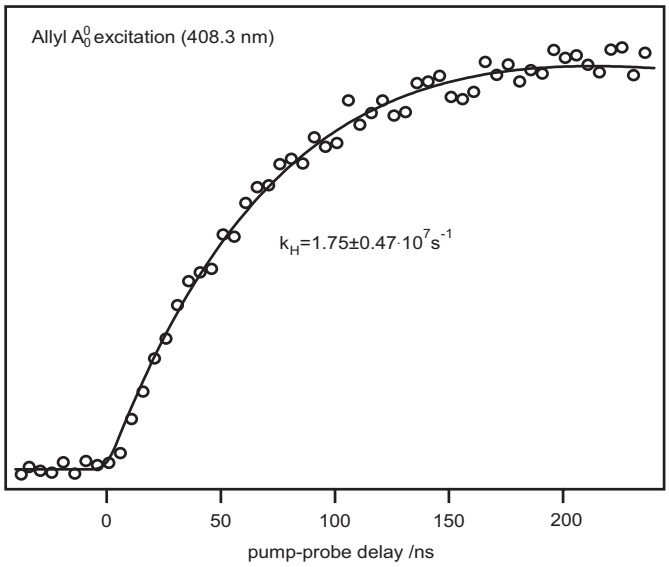

Figure 4.6: Appearance of the hydrogen atom signal as a function of the time delay between pump and probe laser for initial excitation to the $\widetilde{A}$-state origin of the allyl radical.[7]

scale, which together with the results of the molecular dynamics simulation indicates that unimolecular dissociation occurs in the ground electronic state.

In principle, several reaction channels for C–H bond fission in allyl could be open for highly energized allyl radicals. Figure 4.7 shows the calculated reaction channels for allyl unimolecular dissociation. The lowest barrier is for cyclization to the cyclopropyl radical via transition state TS 5. At 70 kcal/mol there is not enough energy available for allyl to dissociate to cyclopropene and a hydrogen atom. As TS 1 is more than 2 kcal/mol lower in energy than TS 2, we expect mainly allene and hydrogen as products. The

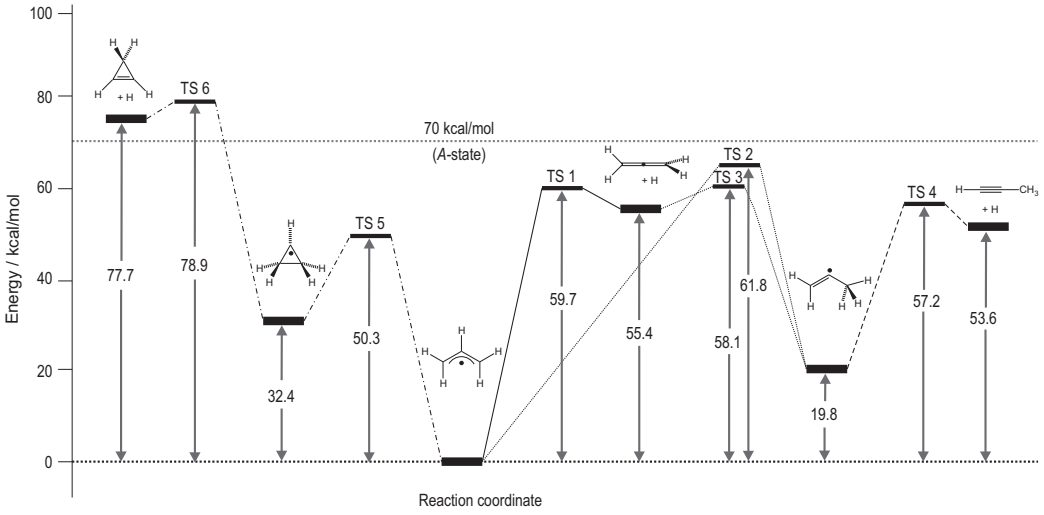

Figure 4.7: Possible reaction pathways for allyl unimolecular dissociation. Cyclization to cyclopropyl and subsequent dissociation to cyclopropene is depicted on the left-hand side. Direct loss of hydrogen to form allene via TS 1 or 1,2-H-shift leading to 2-propenyl, which can dissociate to either allene or propyne are shown on the right-hand side. The energies are zero-point energy corrected and calculated at CSSD(T)/cc-pVXZ (X=D,T,Q, extrapolated to basis set limit) level of theory with geometries optimized using CSSD/cc-pVTZ.

substitution of a selected hydrogen atom with deuterium allows an investigation of the site selectivity of the reaction. For the dissociation forming allene via TS 1, one would expect loss of the hydrogen connected to the central carbon atom in allyl. Upon cyclization to cyclopropyl on the other hand, one of the terminal C–H bonds should be cleaved. Finally, 2-propenyl formed by a 1,2 hydrogen shift can either dissociate to propyne or allene, giving rise to isotopic scrambling. In order to identify the dominant channel, we synthesized 2-deuterioallyliodide as a radical precursor.[7] We performed Doppler spectroscopy of the hydrogen and deuterium atom photofragments and obtained the spectrum depicted in Fig. 4.8. From the ratio between H- and D-signal obtained from the Doppler profiles, we conclude that direct dissociation to allene from loss of the central deuterium atom is the dominant reaction channel.

Having identified allene and a hydrogen atom as the primary photoproducts of allyl, we can compare the experimental dissociation rate constant obtained form the appearance time of the hydrogen atom photoproduct to predictions from statistical rate theories (RRKM). RRKM theory assumes that a microcanonical ensemble is maintained during unimolecular decompo-

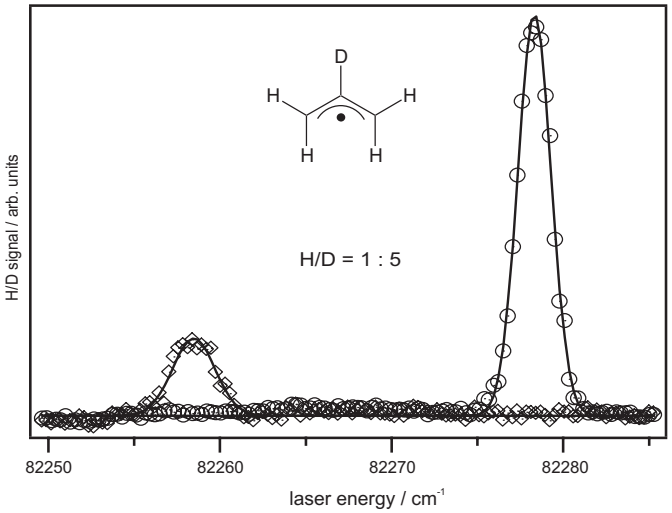

Figure 4.8: Doppler profiles for 2-deuterioallyl obtained from the $\widetilde{A}$-state origin at a time delay of 100 ns between excitation and probe laser. The ratio between hydrogen (diamonds) and deuterium (circles) is $\sim 1:5$.

sition, implying that internal vibrational energy redistribution is rapid and complete among the degrees of freedom of the energized molecule or radical prior to dissociation. In the previous section we demonstrated that the non-radiative decay of $\widetilde{A}$-state allyl occurs on a sub-picosecond timescale, while the measured dissociation rate to allene and a hydrogen atom is about four orders of magnitude slower, see Fig. 4.6. Given the different time-scales for the two processes, one would thus expect that the highly energized allyl radicals redistribute their internal vibrational energy sufficiently prior to dissociation and that RRKM theory should be suitable to predict the dissociation rate. RRKM calculations for direct allene formation yielded a microcanon-

Table 4.3: Unimolecular dissociation rate constants (10^7 s^{-1}) of the allyl radical.

		Experiment		RRKM[1]	
Energy (kcal/mol)	Band	$k_H(E)$	$k_D(E)$	$k_H(E)$	$k_D(E)$
70.0	$\widetilde{A}\ 0_0^0$	1.75	1.09	1.96	1.08
71.6	$\widetilde{A}\ 7_0^1$	3.49	2.04	3.90	2.13
73.5	$\widetilde{A}\ 14_0^1$	6.58	3.89	7.78	4.24

[1]based on anharmonic vibrational frequencies at the HCTH147/TZ2P level of theory.[7]

ical rate constant of $1.96 \times 10^7 \mathrm{s}^{-1}$, which is in good agreement with our experimental unimolecular dissociation rate $k_H(E) = (1.75 \pm 0.47) \times 10^7 \mathrm{s}^{-1}$. We also measured the rates for the isotopically labeled species and obtained $k_D(E) = (1.09 \pm 0.43) \times 10^7 \mathrm{s}^{-1}$, which is roughly two times slower as a consequence of the kinetic isotope effect. More dissociation rate constants obtained

after excitation of allyl to different energies are listed in Table 4.3 together with the calculated RRKM values. The measured dissociation constants are in good agreement with the calculated RRKM values and as expected the reaction becomes faster with increasing excitation energy.

From frequency resolved photoionization of the hydrogen atom photoproduct we obtained the Doppler profile shown in Fig. 4.9. The profile is broadened by the VUV laser linewidth of 0.5 cm^{-1} and a Gaussian FWHM of 2.67 cm^{-1} resulted after proper deconvolution. From our measured Doppler profiles, we derive a translational temperature of 2100 K and an expectation value for the translational energy of 6.2 ± 0.5 kcal/mol.[7] Assuming allene as reaction product, 42% of the excess energy of 14.6 kcal/mol would be released as translation. For hydrogen loss from unsaturated hydrocarbons, typical translational energy releases between 10% and 25% have been reported.[44–46] Obviously, the kinetic energy release of this reaction is much higher.

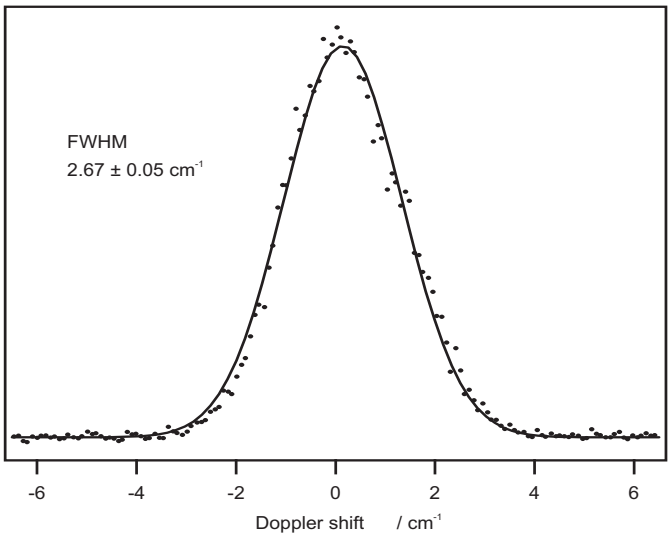

Figure 4.9: H-atom Doppler profile obtained following excitation into the $\widetilde{A}$-state origin of the allyl radical at 100 ns pump-probe delay.

Simple statistical models like the prior distribution approach[47] or RRKM calculations,[48] however, do not take into account the energy of a reverse barrier and are thus restricted to reactions with a loose transition state. The more recent statistical adiabatic impulsive model[49] is more suitable for unimolecular dissociations with a reverse barrier. The total energy available to the products is divided into two reservoirs, the statistical reservoir containing the energy difference between total energy and zero point energy of the transition state and the impulsive reservoir defined as the difference between zero point energies of the transition state and the products, which is the

reverse activation barrier. This model predicts that most of the energy in the impulsive reservoir (60-80%) goes into translation whereas the product energy distribution of the statistical reservoir depends on the transition state geometry.

Our *ab initio* calculations predict a reverse barrier for direct allene formation of 4.3 kcal/mol.[7] If we assume that 70% of the impulsive reservoir (4.3 kcal/mol) goes into translation, 28% of the statistical reservoir (11.3 kcal/mol) must contribute to translation to get the measured expectation value of 6.2 kcal/mol for the translational energy release. In the $\widetilde{A}$-state with small excess energy, the reverse barrier is expected to have a larger influence on the kinetic energy release than in photodissociation at higher excess energy because the impulsive reservoir is independent of excitation energy, as the energy of this reservoir is defined by the constant energy of the transition state. The ratio of energy going from the statistical reservoir into translation corresponds well to values obtained for similar reactions.[15,23,27,44–46]

In summary, the unimolecular dissociation rate in the ground electronic state of the allyl radical to the primary photoproducts allene and hydrogen is well described by statistical rate theories, at least at $\sim$ 70 kcal/mol excitation energy, in stark contrast to the unusually slow dissociation of the ethyl radical described in Chapter 3 and other alkyl radicals.[50,51] To better understand the role of the statistical and impulsive reservoir and the excess energy partitioning in photodissociation of allyl, we also performed photodissociation studies of allyl at $\sim$ 115 kcal/mol excitation energy. A prerequisite to energize allyl in our photodissociation experiments is the presence of an electronically excited state in that energy range and a detailed understanding of the vibronic structure.

C. Dissociation Dynamics from the $\widetilde{B}$-State

The second electronic excited state of the allyl radical is the $\widetilde{B}$ ($^2A_1$) $3s$ Rydberg state first observed and assigned by Hudgens and Dulcey in two-photon excitation.[52] *Ab initio* calculations[24,31,53] predicted that the $3s$ and $3p$ Rydberg character of the allyl radical have a planar (C_{2v}) geometry,[24] similar to that of the allyl cation. The energetic ordering of the close lying $3s$ and $3p$ states, however, could not be established unambiguously from these calculations.

In recent spectroscopic studies,[11,12] we probed the vibronic structure of jet-cooled allyl radicals in the spectral region of the $3s$ and $3p$ Rydberg states using REMPI and UV depletion spectroscopy[54] combined with REMPI detection. Analyzing the vibronic structure of the REMPI spectra of rovibrationally cold (T_{rot} = 5.5 K) allyl allowed for the first time observation of transitions to the $3p_z$ ($\widetilde{D}\ ^2A_1$) Rydberg state, see Fig. 4.10. A mass and partially rotational state-selected UV depletion spectrum also permitted identification of the transition to the short-lived $3p_x$ ($\widetilde{E}\ ^2B_1$) Rydberg state in a molecular beam that carries most of the oscillator strength of these coupled electronically excited states. These experiments allowed for the first time to experimentally derive the energetic ordering of the $3p$ Rydberg states of the allyl radical and provided new assignments for the partially overlapping vibronic band structure of the $3s$ ($\widetilde{B}\ ^2A_1$) and $3p_y$ ($\widetilde{C}\ ^2B_2$) Rydberg states, see Fig. 4.10.

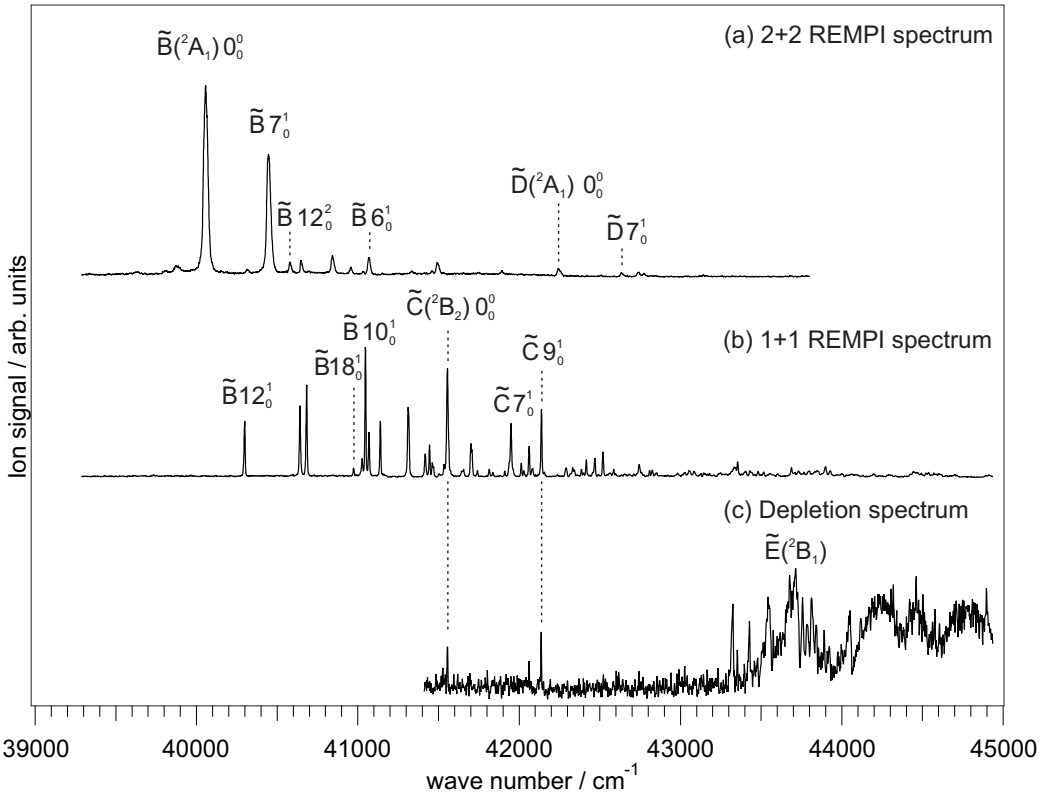

Figure 4.10: The 1+1 REMPI (a) and the 2+2 REMPI (b) overview spectra of the allyl radical. The depletion spectrum (c) of the allyl radical obtained by monitoring the UV-laser depletion of the ion signal intensity produced with 1+1 REMPI via the $\widetilde{B}\ 12^1$ state. The vertical scale has been chosen so that the maxima of the spectra have similar amplitudes and does not reflect the relative photoionization signals.

Understanding the vibronic structure of the allyl radical in the ultraviolet paves the way to perform photodissociation studies of allyl at higher excitation energies than the $\sim$ 70 kcal/mol for our $\widetilde{A}$-state study. The first strong band in one-photon excitation of allyl in the ultraviolet appears at 40 300 cm^{-1} ($\sim$ 115 kcal/mol), which we recently reassigned to the $\widetilde{B}$ 12^1 state,[11,12] see Fig. 4.10. This band has a pronounced partial rotationally resolved structure, especially at higher rotational temperatures and is shown in Fig. 4.11 for $T_{rot} \sim 260$ K. We analyzed the rovibronic band envelopes of allyl[12,55] to obtain the assignments of the spectra summarized in Figure 4.11. The allyl radical is a near prolate top with a large change in the A rotational constant upon electronic excitation leading to a long series of K-sub-band heads in the ${}^{Q}P$ branch. The spectra in Figure 4.11 show that the type A, ${}^{Q}P$-branch sub-band heads are well resolved for K'_a quantum numbers up to at least 14.

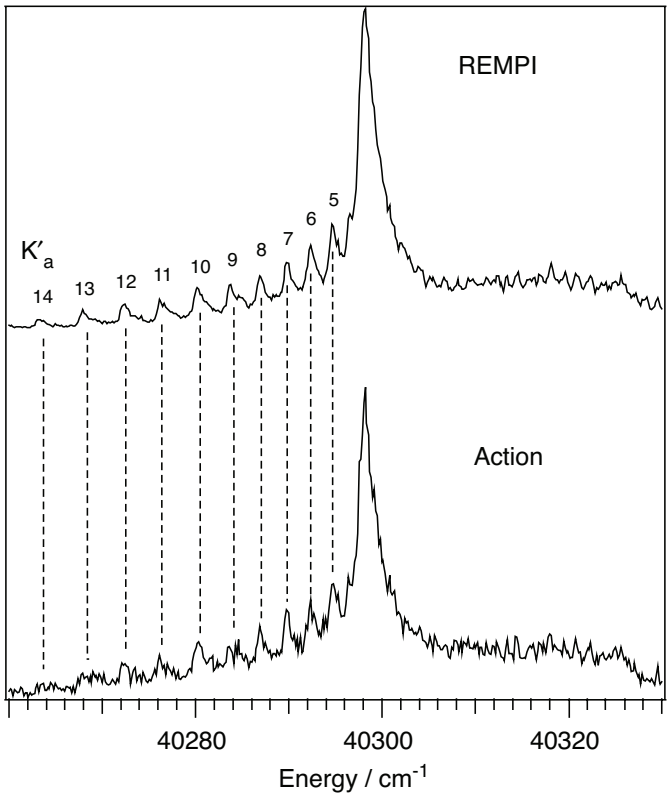

Figure 4.11: REMPI spectrum of the allyl radical and action spectrum recorded simultaneously at a time delay $\Delta t = 50$ ns in the $m/z = 41$ and $m/z = 1$ mass channel. The ${}^{Q}P$-branch of the $\widetilde{B}$ 12^1_0 band is rotationally resolved in K_a (see Refs. 12, 55).

While the spectrum is not resolved in J, the requirement that $J \geqslant K_a$ provides a measure of J-selection in the electronic excitation. This partially rotationally resolved spectrum allows us to prepare allyl radicals that following nonradiative decay to the ground electronic state are vibrationally

hot with ∼115 kcal/mol total energy but with selected *low* or *high* angular momentum.[27]

An investigation of J-dependent dissociation dynamics of the allyl radical was of interest since Szpunar *et al.* reported allyl radicals unusually stable towards dissociation in an experimental study.[13,14] They used photofragment translational spectroscopy to disperse highly vibrationally and rotationally energized allyl radicals produced by secondary photolysis of allyl iodide by their internal energy and found a considerable fraction of allyl radicals with internal energies up to 15 kcal/mol above the barrier that did not dissociate to allene and hydrogen.[13,14] Based on the conjecture from Szpunar *et al.* that the dissociation probability for allyl radical in low J-states is highest, we would expect a reduced dissociation rate for allyl prepared in high J-states.

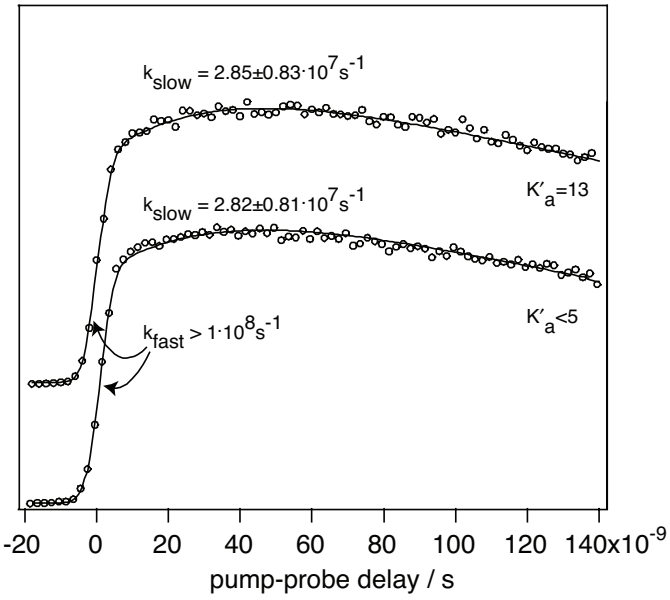

Figure 4.12: Appearance of the hydrogen atom signal following excitation to the $K'_a < 5$ and $K'_a = 13$ sub-band heads of $\widetilde{B}$ 12^1 state allyl.

As in our photodissociation studies for $\widetilde{A}$-state allyl described in the previous section, monitoring the total flux of hydrogen atoms as a function of the time delay between excitation and probe lasers gives the appearance time of the hydrogen atom following electronic excitation. From these transients the unimolecular dissociation rate $k(E, J)$ is obtained. Figure 4.12 shows the time-delayed scans obtained following excitation to the $K'_a < 5$ and $K'_a = 13$ sub-band heads of the $\widetilde{B}$ 12^1 state. Excitation to $K'_a = 13$ compared to $K'_a < 5$ increases J by at least 9. The signal curve has a fast instrument-limited rise up to a time delay of ∼6 ns followed by a slow increase in signal amplitude up to a maximum at ∼45 ns pump-probe delay. At longer delay

times the signal decays as the hydrogen atom leaves the detection volume. We fitted the data with three exponentials convoluted with a 6 ns-FWHM Gaussian corresponding to the cross-correlation of the two laser pulses. We obtain a rate constant $k_{\rm fast} > 1 \times 10^8 {\rm s}^{-1}$ for the initial fast rise of the signal and a rate constant $k_{\rm slow} = (2.82 \pm 0.81) \times 10^7 {\rm s}^{-1}$ for excitation to the $K_a' < 5$ sub-band. The $k_{\rm fast}$ obtained from fitting the $K_a' = 13$ scan is still instrument limited $> 1 \times 10^8 {\rm s}^{-1}$ and $k_{\rm slow} = (2.85 \pm 0.83) \times 10^7 {\rm s}^{-1}$ remains essentially unchanged compared to the $K_a' < 5$ scan.

The two rate constants were previously assigned to competing pathways in the unimolecular dissociation of allyl at 115 kcal/mol on the basis of isotopic labeling experiments.[15,23] Direct cleavage of the central C–H bond in allyl leads to allene formation while a hydrogen shift from allyl to 1-propenyl or 2-propenyl followed by hydrogen loss produces allene or propyne. Based on RRKM modeling, $k_{\rm fast}$ was assigned to direct dissociation forming allene with a calculated rate constant of $4 \times 10^8 {\rm s}^{-1}$. We cannot exclude a small change in the $k_{\rm fast}$ rate constant for $K_a' < 5$ compared to $K_a' = 13$ excitation because the signal rise is instrument limited. Nevertheless, the short lifetime, even for high-J radicals, stands in sharp contrast to the conjecture of Szpunar *et al.*,[13] that these radicals could be long-lived, although the experiments are not completely comparable. They observed allyl radicals that are stable $48 \mu s$ after primary dissociation of allyl-d_2 iodide and concluded that both the barrier to allyl radical direct dissociation and the barrier to isomerization are increased by centrifugal effects. We suggest that centrifugal barriers do not play an important role in the unimolecular dissociation of energized allyl radical with 115 kcal/mol excess energy as the measured rate constants remain essentially unchanged for dissociation of rotationally cold and warm allyl radical.

We also obtained Doppler profiles by scanning the probe laser while detecting the total H-atom photofragment flux at a pump-probe delay $\Delta t = 50$ns that corresponds to maximum signal intensity. For excitation to both the $K_a' < 5$ and $K_a' = 13$ levels of $\widetilde{B}$ 12^1 state allyl the measured Doppler profiles have a near Gaussian shape with a fitted FWHM of 3.98 ± 0.05 cm^{-1}. A large centrifugal barrier for direct dissociation of allyl to produce allene and hydrogen would be expected to lead to a change in the translational energy distribution for high versus low-J radicals. Most of the parent rotational energy should appear in allene angular momentum and not orbital angular momentum $\mu |v_{\rm rel}| b$ because of the near-zero impact parameter

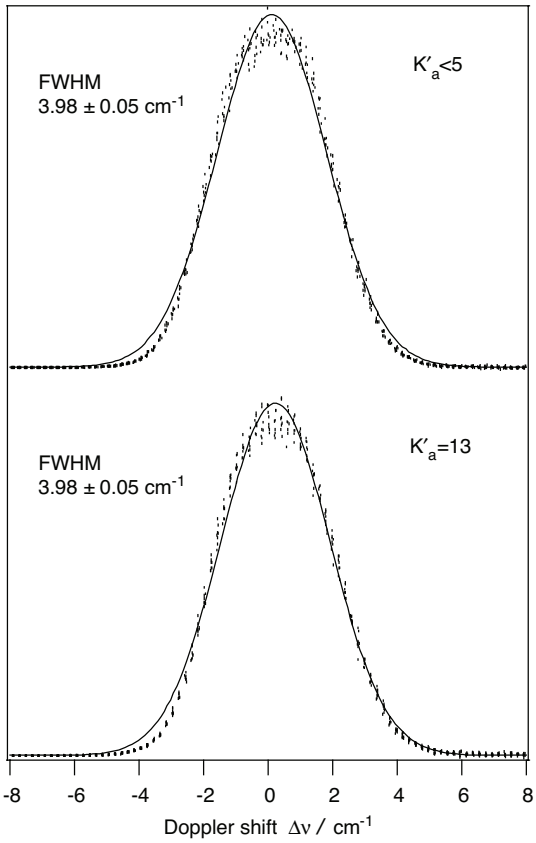

Figure 4.13: Doppler profiles obtained following excitation to the $\widetilde{B}$ 12^1 state $K'_a < 5$ levels (top) and $K'_a = 13$ subband head (bottom) of the allyl radical.

b and the small reduced mass μ for the C-H bond fission. Thus $|v_{\mathrm{rel}}|$ should increase to form rotationally colder allene product and the translational energy distribution should peak at higher energies for $K'_a < 5$ excitation than for $K'_a = 13$. The Doppler profiles obtained for $K'_a < 5$ and for $K'_a = 13$ excitation, however, are identical. This observation is consistent with the unchanged dissociation rates and suggests that centrifugal effects are unimportant for allyl radical unimolecular dissociation at 115 kcal/mol. While we cannot exclude that species with J substantially higher than was accessible in this experiment could show different behavior, we consider it unlikely that a centrifugal barrier is the principal explanation for the long-lived population of radicals reported by Szpunar *et al.*[13]

In summary, the dissociation dynamics of allyl at 115 kcal/mol excitation energy also does not show any evidence for non-statistical effects in dissociation, even at $\sim$ 45 kcal/mol higher excitation energy than following excitation to the $\widetilde{A}$-state. The dissociation rate for decomposition of allyl to the primary photoproducts allene and hydrogen is again well described by RRKM theory. More energy becomes available to the photoproducts because of the higher excitation energy of $\widetilde{B}$-state allyl, which is similar to the exci-

tation energy in the ethyl radical that did show non-statistical behavior in dissociation. Following excitation to the $\widetilde{B}$ 12^1 state of allyl, 24% of the available energy appears in translational energy, a typical value for hydrocarbon radicals.[44–46] Compared to the photodissociation study in the $\widetilde{A}$-state, the percentage of the available energy appearing in translation is reduced from 42% to 24%, which is excepted in the framework of the statistical adiabatic impulsive model because it is primarily the energy in the statistical reservoir that contributes to the kinetic energy release at higher excitation energies.

Bibliography

[1]N. M. Marinov, M. J. Castaldi, C. F. Melius, and W. Tsang, Combuct. Sci. Technol. **128**, 295 (1997).

[2]K. M. Leung and R. P. Lindstedt, Combust. Flame **102**, 129 (1995).

[3]J. A. Miller, R. J. Kee, and C. K. Westbrook, Annu. Rev. Phys. Chem. **41**, 345 (1990).

[4]C. L. Currie and D. A. Ramsay, J. Chem. Phys. **45**, 488 (1966).

[5]K. Tonokura and M. Koshi, J. Phys. Chem. A **104**, 8456 (2000).

[6]T. Schultz, J. S. Clarke, H. Deyerl, T. Gilbert, and I. Fischer, Faraday Discuss. **115**, 17 (2000).

[7]L. Castiglioni, A. Bach, and P. Chen, Phys. Chem. Chem. Phys. **8**, 2591 (2006).

[8]H. C. Longuet-Higgins and J. A. Pople, Proc. Phys. Soc. A (London) **68**, 591 (1955).

[9]A. B. Callear and H. K. Lee, Nature **213**, 693 (1967).

[10]A. B. Callear and H. K. Lee, Trans. Faraday Soc. **64**, 308 (1968).

[11]M. Gasser, A. M. Schulenburg, P. M. Dietiker, F. Merkt, A. Bach, and P. Chen, J. Chem. Phys. **131**, 014304 (2009).

[12]M. Gasser, J. A. Frey, J. M. Hostettler, A. Bach, and P. Chen, J. Phys. Chem. A **114**, 4704 (2010).

[13]D. E. Szpunar, Y. Liu, M. J. McCullagh, L. J. Butler, and J. Shu, J. Chem. Phys. **119**, 5078 (2003).

[14]D. E. Szpunar, M. L. Morton, L. J. Butler, and P. M. Regan, J. Phys. Chem. B **106**, 8086 (2002).

[15]H. Deyerl, T. Gilbert, I. Fischer, and P. Chen, J. Chem. Phys. **107**, 3329 (1997).

[16]D. Stranges, M. Stemmler, X. Yang, J. D. Chesko, A. G. Suits, and Y. T. Lee, J. Chem. Phys. **109**, 5372 (1998).

[17]T. Schultz and I. Fischer, J. Chem. Phys. **107**, 8197 (1997).

[18]T. Schultz and I. Fischer, J. Chem. Phys. **109**, 5812 (1998).

[19]M. L. Morton, L. J. Butler, T. A. Stephenson, and F. Qi, J. Chem. Phys. **116**, 2763 (2002).

[20]J. A. Mueller, J. L. Miller, L. J. Butler, F. Qi, O. Sorkhabi, and A. G. Suits, J. Phys. Chem. A **104**, 11261 (2000).

[21]I. Fischer and P. Chen, J. Phys. Chem. A **106**, 4291 (2002).

[22]S. G. Davis, C. K. Law, and H. Wang, J. Phys. Chem. A **103**, 5889 (1999).

[23]H. Deyerl, I. Fischer, and P. Chen, J. Chem. Phys. **110**, 1450 (1999).

[24]S. Matsika and D. R. Yarkony, J. Am. Chem. Soc. **125**, 10672 (2003).

[25]M. Shahu, Int. J. Quant. Chem. **106**, 501 (2006).

[26]J. Hostettler, L. Castiglioni, A. Bach, and P. Chen, Phys. Chem. Chem. Phys. **11**, 8262 (2009).

[27]L. Castiglioni, A. Bach, and P. Chen, J. Phys. Chem. A **109**, 962 (2005).

[28]K. Holtzhauer, C. Cometta-Morini, and J. F. M. Oth, J. Phys. Org. Chem. **3**, 219 (1990).

[29]H. C. Longuet-Higgins and E. W. Abrahamson, J. Am. Chem. Soc. **87**, 2045 (1965).

[30]R. B. Woodward and R. Hoffmann, J. Am. Chem. Soc. **87**, 395 (1965).

[31]F. Aquilante, K. P. Jensen, and B. O. Roos, Chem. Phys. Lett. **380**, 689 (2003).

[32]C. E. Smith, R. A. King, and T. D. Crawford, J. Chem. Phys. **122**, 054110 (2005).

[33]P. Carsky and R. Zhradnik, J. Phys. Chem. **74**, 1249 (1970).

[34]T. K. Ha, H. Baumann, and J. F. M. Oth, J. Chem. Phys. **85**, 1438 (1986).

[35]G. Levin and W. A. Goddard III, J. Am. Chem. Soc. **97** (1975).

[36]P. A. Arnold and B. K. Carpenter, Chem. Phys. Lett. **328**, 90 (2000).

[37]S. Olivella, A. Sole, and J. M. Bofill, J. Am. Chem. Soc. **112**, 2160 (1990).

[38]S. D. Peyerimhoff and R. J. Buenker, J. Chem. Phys. **51**, 2528 (1969).

[39]D. J. Mann and W. L. Hase, J. Am. Chem. Soc. **124**, 3208 (2002).

[40]D. J. Mann and M. D. Halls, Phys. Chem. Chem. Phys. , 5066 (2002).

[41]M. Yamaguchi, J. Mol. Struct.: THEOCHEM **365**, 143 (1996).

[42]J. Tully, J. Chem. Phys. **93**, 1061 (1990).

[43]G. Granucci and M. Persico, J. Chem. Phys. **126**, 134114 (2007).

[44]K. Tsukiyama and R. Bersohn, J. Chem. Phys. **86**, 745 (1987).

[45]S. Satyapal, G. W. Johnston, R. Bersohn, and I. Oref, J. Chem. Phys. **93**, 6398 (1990).

[46]J. Park and R. Bersohn, J. Chem. Phys. **93**, 5700 (1990).

[47]R. D. Levine and R. B. Bernstein, *Molecular Reaction Dynamics and Chemical Reactivity*, Oxford University Press, New York, 1987.

[48]A. S. Sudbo, P. A. Schulz, E. R. Grant, Y. R. Shen, and Y. T. Lee, J. Chem. Phys. **70**, 912 (1979).

[49]D. H. Mordaunt, D. L. Osborn, and D. M. Neumark, J. Chem. Phys. **108**, 2448 (1998).

[50]B. Noller and I. Fischer, J. Chem. Phys. **126**, 144302 (2007).

[51]M. Zierhut, W. Roth, and I. Fischer, J. Phys. Chem. A **108**, 8125 (2004).

[52]J. W. Hudgens and C. S. Dulcey, J. Phys. Chem. **89**, 1505 (1985).

[53]J. M. Oliva, J. Gerratt, D. L. Cooper, P. B. Karadakov, and M. Raimondi, J. Chem. Phys. **106**, 3663 (1997).

[54]L. Feng, X. Huang, and H. Reisler, J. Chem. Phys. **117**, 4820 (2002).

[55]J. A. Blush, D. W. Minsek, and P. Chen, J. Phys. Chem. **96**, 10150 (1992).

Chapter 5

The 1-Methylallyl Radical

I. Introduction

The dissociation dynamics of hydrogen atom loss from small hydrocarbon radicals following electronic excitation are currently not fully understood. Several experimental studies of highly energized 2-propyl,[1] ethyl,[2] and *tert*-butyl[3] radicals found unimolecular dissociation rates that are much slower than predicted by Rice-Ramsperger-Kassel-Marcus (RRKM) theory. In contrast, the dissociation rate of jet-cooled allyl radicals also prepared by initial optical excitation agree well with predications from statistical rate theories.[4,5] We seek to find a structural motif in hydrocarbon radicals or topological features of the potential energy surfaces that leads to non-statistical behavior in unimolecular dissociation. In this report, we focus on the methyl group as a structural element and probe for non-statistical effects in a combined experimental and computational study of the photodissociation dynamics of the 1-methylallyl (C_4H_7) radical.

There are only a few spectroscopic studies of the 1-methylallyl radical using absorption,[6] photoelectron,[7] electron spin resonance,[8,9] and resonance Raman spectroscopy.[10] Callear and Lee[6] observed a series of broad and diffuse absorption bands of 1-methylallyl produced through flash photolysis in the ultraviolet (UV) between 226 and 238 nm that have remained unassigned since 1968. Hudgens reported several poorly resolved and unassigned bands of 1-methylallyl in a multiphoton photoionization experiment with at least three photons using visible light near 480 nm.[11] More recently, Lau *et al.* performed a photodissociation study at 234 nm to characterize potential photolytic precursors for different C_4H_7 isomers, including 1-methylallyl, using

velocity map imaging.[12] Miller presented an extensive theoretical study of the complex C_4H_7 potential energy surface in the ground electronic state,[13] but to the best of our knowledge, no *ab initio* predictions of the electronic excited states of the 1-methylallyl radical have been reported so far.

In this report, we use resonance-enhanced multi-photon photoionization (REMPI) spectroscopy to reveal the vibronic structure of the $\widetilde{A} \leftarrow \widetilde{X}$ band system of jet-cooled 1-methylallyl radicals for the first time. Time- and frequency resolved photoionization of the hydrogen atom photoproduct following excitation to the $\widetilde{A}$-state of the 1-methylallyl radical provides information on the dissociation dynamics.

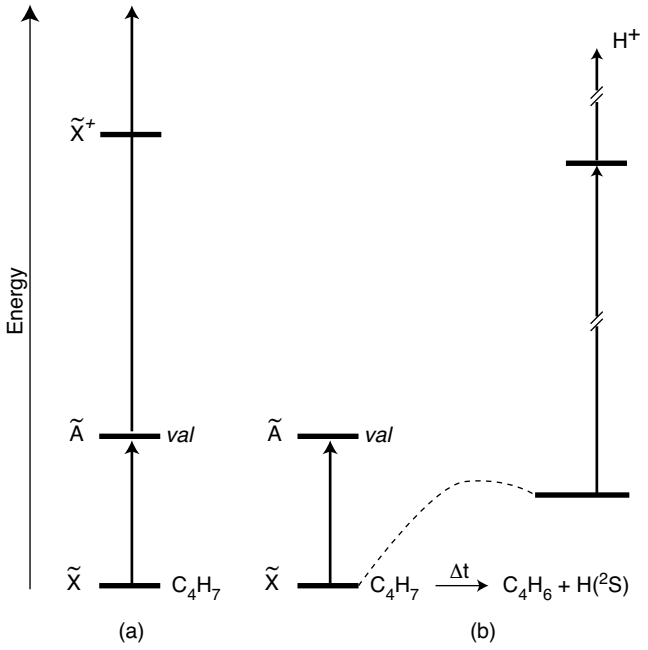

Figure 5.1: Schematic energy level diagram (a) for the 1+1′ REMPI detection of the 1-methylallyl radical, C_4H_7, and (b) time-delayed photoionization of the H-atom photoproduct *via* the Lyman-α transition after photoexcitation of 1-methylallyl.

II. Experimental

The experimental apparatus is a modified version of one described previously.[4] We produce jet-cooled 1-methylallyl radicals by photolysis of either pent-3-enyl nitrite or 1-iodobut-2-ene seeded in 3 bars of helium at 266 nm inside a quartz capillary tube[14] (internal diameter: 0.9 mm, length: 22 mm) attached to the 0.8 mm orifice of a pulsed valve operating at 20 Hz (General Valve Series 9). Both radical precursors gave comparable ion signal intensities in the resonance-enhanced multi-photon photoionization experiments. In a comparable experiment on the allyl radical we used allyl iodide

as a photolytic radical precursor and have shown[15] that rotational temperatures $T_{rot} < 10$ K can be achieved with our radical source with no evidence for hot-bands that arise from insufficient cooling in the supersonic expansion. For the allyl radical produced with our photolytic radical source,[15] we obtained similar ion signal intensities as for allyl radicals produced by the tubular reactor in flash pyrolysis.[16] We also attempted to produce 1-methylallyl radical by flash pyrolysis of 1-iodobut-2-ene, but in this case the resulting signal-to-noise ratio in the REMPI spectrum was poor compared to that obtained from photolytically generated radicals. The same observation also holds true for 2-methylallyl radicals produced using a range of precursors, including 3-iodo-2-methylprop-1-ene, 3-bromo-2-methylprop-1-ene and 3-methylbut-3-enyl nitrite.[17]

We used the fourth harmonic output (266 nm) of a Nd:YAG laser (Spectra Physics, GCR series) to provide UV light for photolysis with typical pulse energies of 8 mJ/pulse loosely focused onto the quartz capillary tube approximatively 2 mm from its exit. The output of two Nd:YAG-pumped dye lasers (Radiant Dyes Narrowscan) provided UV or visible light needed for recording the $1+1'$ REMPI spectra that we calibrated by monitoring the laser wavelength during each scan with a pulsed wavelength meter (Toptica Photonics WS-6). We used collimated laser beams aligned anti-collinearly that intersect the skimmed radical beam in the source of a linear time-of-flight mass-spectrometer for the $1+1'$ REMPI process. The resulting ions were detected using double microchannel plates.

Nonresonant frequency tripling in a cell filled with krypton of the 365 nm output of a Nd:YAG pumped dye laser provides 121.6 nm vacuum ultraviolet (VUV) light for $1+1'$ REMPI detection of the hydrogen atoms. Figure 5.1(b) shows the energetics of the pump-probe experiments. We integrate the hydrogen ion signal for typically 40 laser shots as a function of the excitation laser wavelength at a fixed time delay Δt, which results in a photofragment action spectrum. In a second experiment, we prepare electronically excited state 1-methylallyl radicals and obtain Doppler profiles by scanning the probe laser while detecting the total H-atom photofragment flux using $1+1'$ REMPI at a fixed time delay of 70 ns controlled by a digital delay generator (Stanford Research DG 535) between excitation and probe laser pulses. In a third experiment, monitoring the total flux of hydrogen atoms as a function of the time delay between excitation and probe pulses provides information about the dissociation rate. Both radical precursors gave identical results in the

pump-probe experiments.

III. Results and Discussion

We calculated the geometries and energetics of *E*- and *Z*-1-methylallyl radicals in their ground and first electronically excited states at the MCSCF(3,3)/DZP++ level of theory to guide our experimental search for the $\widetilde{A} \leftarrow \widetilde{X}$ transition in 1-methylallyl. The active space included the highest doubly occupied orbital (HOMO), the singly occupied orbital (SOMO) and the lowest unoccupied π^*-orbital (LUMO). The *E*-isomer is calculated to be slightly more stable by 0.6 kcal/mol than *Z*-1-methylallyl in the electronic ground state with a calculated barrier of only 14.8 kcal/mol for *E*/*Z*-isomerization.[18] Figure 5.2 shows the calculated equilibrium geometries for both the ground and first electronically excited state. While the ground state has a planar geometry for both isomers, the first valence excited state structures are twisted around the central C–C bond resulting in out-of-plane distortions with a CCCC dihedral angle of 50.3° for the *E*-isomer and 11.6° for the *Z*-isomer. Our *ab initio* calculations predict adiabatic excitation energies of 24 284 cm^{-1} for *E*-1-methylallyl and 24 191 cm^{-1} for *Z*-1-methylallyl, respectively.

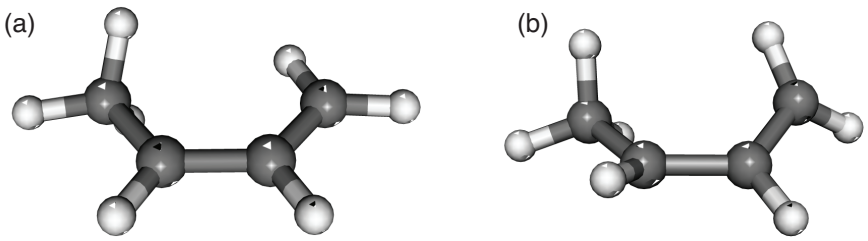

Figure 5.2: The calculated geometries at the MCSCF(3,3)/DZP++ level of theory for (a) the ground electronic state and (b) the non-planar first valence excited state of the *Z*-1-methylallyl radical.

Figure 5.3(a) shows the 1+1′ REMPI spectrum of the 1-methylallyl radical in the spectral range from 23 900 to 24 600 cm^{-1} obtained with a fixed ionization laser wavelength of 250 nm. The first band visible in the spectrum appears at 23 980 cm^{-1} that we tentatively assign to the electronic origin of the $\widetilde{A} \leftarrow \widetilde{X}$ transition of one of the isomers of the 1-methyallyl radical, based

on the excellent agreement with our *ab initio* predictions. The weak intensity of this band can be rationalized by the large changes in geometry following electronic excitation, which should lead to unfavorable Franck-Condon factors for the transition to the 0^0 state. Alternatively, this band could also be assigned as a hot-band with the more intense band at 24 080 cm^{-1} as the origin. However, our previous experiments of allyl have shown that our radical source produces cold radicals with no evidence for hot bands.[15] In principle, these two bands could also be attributed to the electronic origins for *Z*- and *E*-1-methylallyl given that the experimental wave number difference is 100 cm^{-1}, which is nearly the same as the 93 cm^{-1} predicted *ab initio*. Compared to the excitation energy these energy differences are very small and are not expected to affect the dissociation rate and dynamics of the 1-methylallyl radical, see below. A more detailed discussion of the vibronic structure of $\widetilde{A}$-state 1-methylallyl will be presented elsewhere.

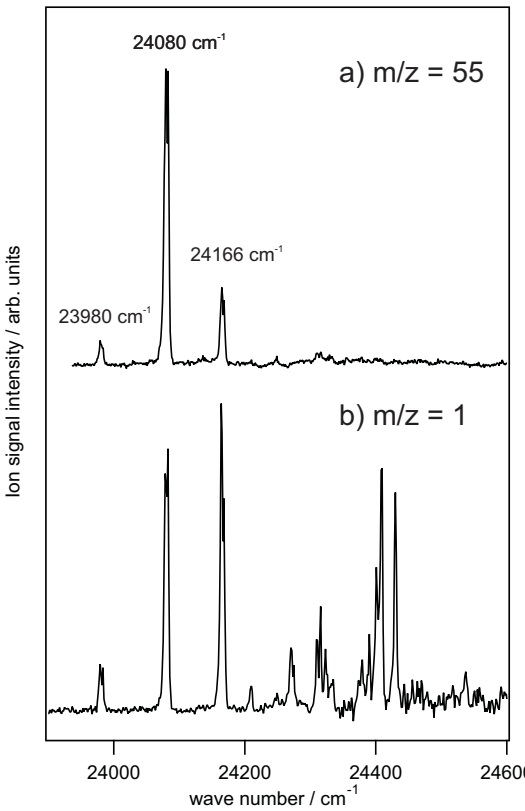

Figure 5.3: (a) 1+1′ REMPI spectrum of the 1-methylallyl radical (b) H-atom photofragment action spectrum recorded 100 ns after photoexcitation.

Following electronic excitation to its $\widetilde{A}$-state, 1-methylallyl loses hydrogen as visible in the photofragment action spectrum displayed in Figure 5.3(b). For each resonance in the REMPI spectrum we find a corresponding resonance in the action spectrum, confirming that hydrogen is lost from neutral 1-methylallyl. The band intensities, however, are different in the REMPI

spectrum compared to the action spectrum with rapidly decreasing band intensities in the REMPI spectrum with increasing excitation energy. The 1+1′ REMPI ion signal intensity strongly depended on the temporal overlap of the excitation and ionization laser pulses and was sensitive to the nanosecond, which indicates that the decreasing band intensities in the REMPI spectrum most likely arises from short excited state lifetimes.

We also probed the dynamics of photoinduced hydrogen abstraction of the 1-methylallyl radical. Figure 5.4 shows the appearance time of the hydrogen atom photoproduct following excitation of 1-methylallyl at 24 080 cm^{-1}. The signal intensity rises slowly and reaches a maximum at a time delay $\Delta t \sim 100$ ns followed by a slow decay as the hydrogen atoms leave the detection volume in the source of our linear time-of-flight spectrometer. The solid line shown in Fig. 5.4 results from a fit of the experimental data to two exponentials convoluted with a 6 ns FWHM Gaussian corresponding to the cross-correlation of the two laser pulses. We obtain a rate constant k_H of $3.2(12) \times 10^7$ s^{-1} for the appearance of the H-atom photoproduct. The slow appearance rate of the photoproduct together with the presumably short excited state lifetimes inferred from the REMPI and action spectra suggests a nonradiative decay of 1-methylallyl radical after photoexcitation followed by dissociation in the ground electronic state, a mechanism similar to that observed for the allyl radical.[5,19]

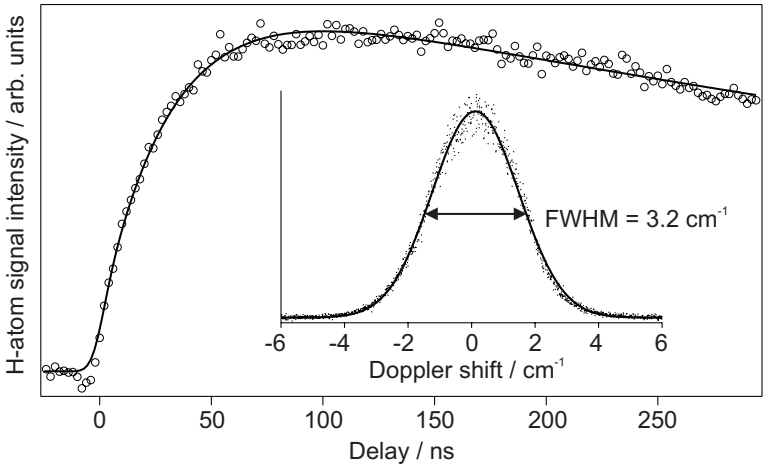

Figure 5.4: Appearance time of the H-atom signal following excitation of the 1-methylallyl radical at 24 080 cm^{-1}. The inset shows the Doppler profile recorded at a 70 ns pump-probe delay.

To gain insight into the dissociation dynamics, we calculated a part of the complex ground state potential energy surface[13] for the C_4H_7 to C_4H_6+H reaction at the CCSD(T)/CBS level of theory. The calculated low energy reaction pathways for C–H bond fission and isomerization of the 1-methylallyl radical appear in Fig. 5.5. In our photodissociation experiment we excite

the 1-methylallyl radical at 24 080 cm^{-1}, which corresponds to an excitation energy of 68.8 kcal/mol. At this low excitation energy the pathway for isomerization via TS 5 to the 2-methylallyl radical is not yet accessible. The most favorable pathway for C–H bond fission from 1-methylallyl is the formation of buta-1,3-diene over a barrier of only 46.6 kcal/mol at TS 1. In principle, dissociation to methyl-allene and H is also possible, but TS 2 leading to these products is more than 15 kcal/mol higher than TS 1 and we therefore expect primarily buta-1,3-diene and H as photoproducts.

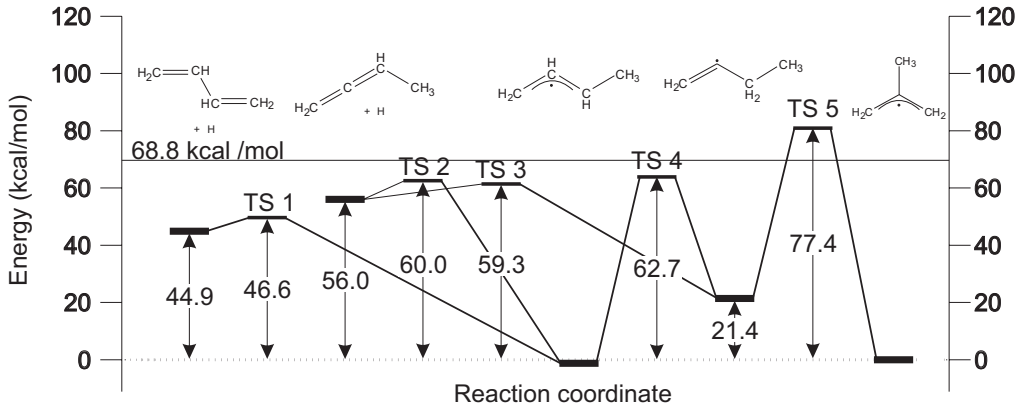

Figure 5.5: Calculated reaction pathways for the *E*-1-methylallyl radical C–H bond fission and isomerization to 2-methylallyl. The energetics for *Z*-1-methylallyl are very similar and omitted in this scheme for clarity.

Assuming buta-1,3-diene and H as the primary photofragments and unimolecular decomposition in the ground electronic state of C_4H_7, we can predict the dissociation rate using Rice-Rampsperger-Kassel-Marcus (RRKM) theory. The calculated RRKM rate constant for dissociation of *Z*-1-methylallyl at an excitation energy of 68.8 kcal/mol is 5.10×10^7 s^{-1}, while the corresponding rate for the *E*-isomer is slightly faster. The energized ground state 1-methylallyl radicals are expected to undergo fast *E*/*Z* isomerization with a RRKM rate of $\sim 3 \times 10^{10}$ s^{-1} prior to dissociation and therefore from the point of view of the dissociation dynamics it does not matter which stereoisomer we selectively excited at 24 080 cm^{-1}. We can now compare the experimental dissociation rate to the predictions made using RRKM theory and we find that they agree within a factor of 2 when using the CCSD(T) energetics and anharmonic vibrational frequencies obtained at the HCTH147/TZ2P level of theory.

We also measured Doppler profiles following excitation of 1-methylallyl at 24 080 cm^{-1} by scanning the probe laser over the broadened Lyman-α transition. The full-width half-maximum (FWHM) for a Gaussian fit to the experimental Doppler profile shown in the inset in Fig. 5.4 is 3.20 cm^{-1}, deconvoluted for the VUV laser-bandwidth. This corresponds to an average kinetic energy release of 8.58 kcal/mol or 37% of the available energy using the calculated reaction energies for dissociation to buta-1,3-diene and H. This is somewhat less than the 42% we found in the analogous photodissociation experiments of the allyl radical[5] following excitation to its $\widetilde{A}$-state where the nature of the dissociation dynamics agrees with a statistical mechanism.

IV. Conclusion

Resonance-enhanced multi-photon ionization combined with photofragment action spectroscopy of jet-cooled 1-methylallyl radicals provides information on the vibronic structure and the dissociation dynamics. We observed a previously unknown band system in the 1+1′ REMPI spectrum that we attribute to the $\widetilde{A} \leftarrow \widetilde{X}$ transition of 1-methylallyl starting with a weak band at 23 980 cm^{-1}. *Ab initio* calculations at the MCSCF level of theory reveal that the $\widetilde{A}$-state of 1-methylallyl is a non-planar valence excited state, but the predicted adiabatic excitation energies do not allow us to identify which stereoisomer contributes most to the observed 1+1′ REMPI spectrum. Comparing the band intensities in the 1+1′ REMPI spectrum to those in the H-atom photofragment action spectrum suggests that the excited state lifetimes rapidly decreases with increasing excitation energy in the $\widetilde{A}$-state of 1-methylallyl, most likely because of nonradiative decay to the ground electronic state.

Time- and frequency resolved 1+1′ photoionization of the hydrogen atom photoproduct provides information on the dissociation dynamics of 1-methylallyl following excitation to its $\widetilde{A}$-state. The measured dissociation rate constant obtained from the appearance time of the hydrogen atoms following photoexciation is $3.2(12)\times10^7$ s^{-1} and agrees within a factor of two to the RRKM predictions for C–H bond fission to form buta-1,3-diene and H, the most favorable dissociation pathway in the electronic ground state identified at the CCSD(T) level of theory. The fraction of the available energy to the photoproducts that appears in translational energy is nearly the same as in photodissociation of the $\widetilde{A}$-state allyl radical,[5] which together

with the good agreement of the measured dissociation rate with our RRKM predictions supports a picture of statistical dissociation in the 1-methylallyl radical.

Bibliography

[1]B. Noller and I. Fischer, J. Chem. Phys. **126**, 144302 (2007).

[2]T. Gilbert, T. L. Grebner, I. Fischer, and P. Chen, J. Chem. Phys. **110**, 5485 (1999).

[3]M. Zierhut, W. Roth, and I. Fischer, J. Phys. Chem. A **108**, 8125 (2004).

[4]H. Deyerl, I. Fischer, and P. Chen, J. Chem. Phys. **110**, 1450 (1999).

[5]L. Castiglioni, A. Bach, and P. Chen, Phys. Chem. Chem. Phys. **8**, 2591 (2006).

[6]A. B. Callear and H. K. Lee, Trans. Faraday Soc. **64**, 308 (1968).

[7]J. C. Schultz, F. A. Houle, and J. L. Beauchamp, J. Am. Chem. Soc. **106**, 7336 (1984).

[8]J. K. Kochi and P. J. Krusic, J. Am. Chem. Soc. **90**, 7157 (1968).

[9]D. J. Driscroll, W. Martir, and J. H. Lunsford, J. Phys. Chem. **91**, 3585 (1987).

[10]D. H. Tarrant, J. D. Getty, X. Liu, and P. B. Kelly, J. Phys. Chem. **100**, 7772 (1996).

[11]J. W. Hudgens, in *Advances in Multi-Photon Processes and Spectroscopy*, edited by S. H. Lin, World Scientific, Singapore, 1984.

[12]K.-C. Lau, Y. Liu, and L. J. Butler, J. Chem. Phys. **125**, 144312 (2006).

[13]J. L. Miller, J. Phys. Chem. A **108**, 2268 (2004).

[14]J. M. Dyke, S. Willitsch, and F. Merkt, Helv. Chim. Acta **86**, 1152 (2003).

[15]M. Gasser, J. A. Frey, J. M. Hostettler, A. Bach, and P. Chen, J. Phys. Chem. A **114**, 4704 (2010).

[16]D. W. Kohn, H. Clauberg, and P. Chen, Rev. Sci. Instrum. **63**, 4003 (1992).

[17]M. Gasser, J. A. Frey, J. M. Hostettler, and A. Bach, (unpublished, 2010).

[18]P. J. Gorton and R. Walsh, J. C. S. Chem. Comm. **13**, 783 (1972).

[19]J. Hostettler, L. Castiglioni, A. Bach, and P. Chen, Phys. Chem. Chem. Phys. **11**, 8262 (2009).

Chapter 6

Discussion and Conclusion

We report a combined experimental and computational study of the photodissociation dynamics and spectroscopy of small hydrocarbon radicals in the gas-phase. This approach allows to follow the dissociation dynamics after photoexcitation on multiple timescales from ultrafast electronically nonadiabatic processes to competing isomerization and unimolecular dissociation pathways on the electronic ground state potential energy surface. I will first briefly summarize the dissociation dynamics of the allyl and the ethyl radical and then discuss the nature of their dissociation dynamics as well as the different types of non-statistical effects that can occur in dissociation.

For the allyl radical, C_3H_5, the primary photophysical and photochemical processes upon electronic excitation are very intricate. We have studied the competing ultrafast photochemical deactivation pathways of the $\widetilde{A}$-state allyl radical, mediated by conical intersections using *ab initio* molecular dynamics, which allowed us to determine the branching ratios for the different pathways and gain insight into the nuclear motions that govern them.[1] The electronically nonadiabatic dynamics predict a near equal probability for conrotatory and disrotatory excited state deactivation with 92% of all trajectories producing hot ground state allyl radicals within less than one picosecond. The highly energized allyl radicals subsequently dissociate on the ground state surface to allene and hydrogen, which is consistent with the selective C–D bond fission observed in 2-deuterioallyl. The measured dissociation rate constant obtained from time-resolved photoionization of the hydrogen atom product is $k_{diss} = 1.75 \times 10^7 \mathrm{s}^{-1}$, which is about four orders of magnitude slower than the electronically nonadiabatic process that populates the ground state parent radicals, but agrees to within experimental error to the

dissociation rate predicted using Rice-Rampsperger-Kassel-Marcus (RRKM) theory.[2] Increasing the total energy in allyl from 70 kcal/mol for the $\widetilde{A}$-state photodissociation experiments to 115 kcal/mol following selective excitation to both high- and low-J allyl radicals in the $\widetilde{B}$-state does not change the nature of the unimolecular dissociation dynamics.[3] The rate constant for dissociation is still well described by *statistical* theories (RRKM).

For the ethyl radical – a key intermediate in cracking and combustion – we studied the mechanism for C–H bond fission and nonradiative decay from the lowest-lying excited state using *ab initio* molecular dynamics motivated by experimental reports in the literature describing *non-statistical* behavior in the dissociation to the photoproducts ethylene and hydrogen.[4,5] From an ensemble of trajectories we obtain a calculated excited state lifetime of $\sim$ 20 fs in excellent agreement with experiment. The simulated energy disposal in the photofragments is consistent with previous experiments and we propose that a strictly nonadiabatic mechanism accounts for nonradiative decay in ethyl radical, which followed by C–H bond fission is the dominant dissociation channel accounting for 68% of all trajectories.[6] This dissociation channel is in competition with adiabatic dissociation resulting in electronically excited state ethylene and H, a dissociation channel that has not yet been experimentally observed. Surface hopping also produces highly energized hot ground state ethyl radicals far above the threshold to dissociation to ethylene and hydrogen. Our simulations confirmed that a population of highly energized ground state ethyl radicals can survive much longer than the $\sim$1 ps RRKM lifetime.[7,8] The analysis of the long-lived trajectories using new methods based on a wavelet-based decomposition of the trajectories in the time-frequency domain revealed episodes of near quasiperiodic behavior associated with resonance trappings displaying large-amplitude low-frequency excursions of the atoms, predominantly a counter-rotation of the methyl and methylene group. Those resonance trappings in the reactant phase space region are in general believed to play an important role in the understanding of non-statistical unimolecular dissociation and isomerization processes.[9–11]

The nature of the dissociation dynamics of highly energized allyl radicals and ethyl radicals differ strongly with ethyl showing several different types of *non-statistical* effects in dissociation. Dynamical non-statistical effects in unimolecular reactions have been suggested quite often for chemical reactions proceeding at the boundary of a concerted versus a stepwise mechanism involving many types of reactive intermediates including carbocations and

carbenes.[12–19] The underlying physics and origin of those dynamical non-statistical effects, however, is often not fully understood, despite remarkable recent progress in the theory of unimolecular reactions.[9–11,20]

The first type of non-statistical effect occurs quiet often in photoinduced reactions, where interactions between excited electronic states and also the ground electronic state determines the competition between different dissociation pathways.[21–26] A key signature of those ultrafast dissociation dynamics enabled by conical intersections[27] between two states occurring often on a femtosecond time scale is a non-statistical vibrational energy distribution in the photofragments where certain quantum states are populated preferentially. Recent studies of the photodissociation dynamics of aromatic and heteroaromatic molecules[21–23,25] as well as of small biomolecules have caused a paradigm shift in the understanding of organic photochemistry driven both by experimental and theoretical studies of ultrafast dynamics enabled by conical intersections. This type of non-statistical effect also occurs in small hydrocarbon radicals,[6,28–31] including the ethyl radical described in Chapter 3 in which ultrafast nonadiabatic and adiabatic dissociation are in competition producing hydrogen atoms with an anisotropic angular distribution. In contrast, in the allyl radical a nonadiabatic mechanism can also account for nonradiative decay, at least following excitation to the $\widetilde{A}$-state, but subsequent dissociation on the ground state surface is well described by statistical theories.

The second type of non-statistical effect[11,12,20,32] occurs both in thermal and photoinduced chemical reactions where the reaction pathway bypasses the conventional saddle-point transition state on the ground state potential energy surface or does not follow the minimum energy pathway from reactants to products. In those type of reactions, the widely used statistical models of kinetics, most notably transition-state theory and its microcanonical analogue RRKM theory are inadequate to describe the experimentally observed behavior. During chemical reactions the molecules sample a complex multi-dimensional potential energy landscape and even subtle topological features such as submerged barriers or "reefs" can greatly affect the reaction rates.[33–35] A recent example highlighting the interplay between theory and experiment in the understanding of non-statistical reaction mechanisms where the current transition state theories cannot predict the reaction products and kinetics is the photoinduced decomposition of formaldehyde and acetaldehyde.[36–39] Highly energized acetaldehyde decomposes in the ground

state in a pathway in which methyl orbits or "roams" around the HCO fragment at very large interfragment distances to return and abstract a hydrogen to form methane and CO. This "roaming" mechanism may be relatively common and could have important consequences for the modeling of combustion reactions.

The picture that emerges form the analysis of the unusually long-lived classical trajectories for ethyl radical with lifetimes far exceeding the ~ 1 ps RRKM lifetime on the ground state surface, however, is quiet different and suggests another type of non-statistical effect. These trajectories on the ground state surface of the ethyl radical *do* eventually pass in the vicinity of the transition state just prior to dissociation to ethylene and hydrogen as revealed by the nuclear motions in the classical trajectories. The value of the normalized instantaneous orbital complexity and the largest local Lyapunov exponent for those trajectories rapidly increases just prior to passing the transition state, which indicates chaotic motion and sufficiently rapid energy randomization just shortly before dissociation as described in Chapter 3. This conclusion is also supported by the calculated recoil energy distributions for the energy disposal of the excess energy in the photofragments that do not differ at all for ensembles of trajectories run on potential energy surfaces that yield a fraction of unusually long-lived trajectories and those that do not. This indicates that the non-statistical effect in the ethyl radical affects only the *dissociation rate*, but not the final energy distribution in the photofragments, which is well described by a statistical distribution. Time-frequency analysis of the long-lived trajectories revealed episodes of near quasiperiodic behavior associated with resonance trappings[40–43] in the *reactant phase space* region,[9–11] which can explain the experimentally observed unusually long lifetime with respect to dissociation of highly energized ethyl radicals.

The observed dissociation rates of other alkyl radicals[44,45] are also significantly slower than predicted by RRKM theory, but for those alkyl radicals the mechanism producing unusually long-lived radicals is not yet clear. In stark contrast, the dissociation mechanism for the allyl radical agrees well with predications from statistical rate theories. This leads to the question of what triggers non-statistical dissociation dynamics. One of the obvious structural differences between the alkyl radicals that showed non-statistical behavior and the allyl radical that displays statistical behavior in dissociation are the methyl groups. Intriguingly, the two components of nuclear motions associated with the resonance trappings in the ethyl radical that we

postulate to be the origin of the non-statistical dynamics are best described as large amplitude motions involving an internal rotation about the C_α–C_β bond, and an inversion motion at the radical center with some C–C bond stretch character. We recently studied the photodissociation dynamics of the 2-methylallyl radical probing for any putative non-statistical behavior in dissociation arising from the structural change induced by the methyl rotor.[46] The complex dynamics with many competing dissociation channels unfortunately precluded an assignment of the measured dissociation rates to a specific dissociation channel and no conclusions could be drawn about the nature of the dissociation dynamics. To our surprise, the unpublished results presented in Chapter 5 of a photodissociation experiment on a selected stereoisomer of the 1-methylallyl radical under carefully controlled conditions following excitation to its $\widetilde{A}$-state supports a picture of statistical dissociation dynamics for C–H bond fission to produce buta-1,3-diene and hydrogen.

This combined experimental and computational study provides a comprehensive picture of the nature of the dissociation dynamics of small hydrocarbon radicals. Unexpected rates of dissociation not predictable by statistical rate theories on time scales that may fall into the range of collisional timescales can greatly affect the fall-off behavior in combustion environments and it is therefore important to understand the extent and origin of such non-statistical effects as the kinetics have important consequences in the modeling of crackers and reformers in the petrochemical industry. Much of the recent advances in understanding of non-statistical effects in chemical reactions comes from a fruitful interplay between experiments and theory in a way that animates both future studies and strengthens the conclusions and insights gained from both experimental and theoretical studies. Using this approach, we have shown that small hydrocarbon radicals are an ideal testbed to explore non-statistical effects in unimolecular decomposition. Further studies are a potential key complement to this work and may provide a more comprehensive overview of the extent of non-statistical effects in chemical reactions.

Bibliography

[1]J. Hostettler, L. Castiglioni, A. Bach, and P. Chen, Phys. Chem. Chem. Phys. **11**, 8262 (2009).

[2]L. Castiglioni, A. Bach, and P. Chen, Phys. Chem. Chem. Phys. **8**, 2591 (2006).

[3]L. Castiglioni, A. Bach, and P. Chen, J. Phys. Chem. A **109**, 962 (2005).

[4]T. Gilbert, T. L. Grebner, I. Fischer, and P. Chen, J. Chem. Phys. **110**, 5485 (1999).

[5]G. Amaral, K. Xu, and J. Zhang, J. Chem. Phys. **114**, 5164 (2001).

[6]J. Hostettler, A. Bach, and P. Chen, J. Chem. Phys. **130**, 034303 (2009).

[7]A. Bach, J. Hostettler, and P. Chen, J. Chem. Phys. **123**, 021101 (2005).

[8]A. Bach, J. Hostettler, and P. Chen, J. Chem. Phys. **125**, 024304 (2006).

[9]G. S. Ezra, H. Waalkens, and S. Wiggins, J. Chem. Phys. **130**, 164118 (2009).

[10]P. Manikandan, A. Semparithi, and S. Keshavamurthy, J. Phys. Chem. A **113**, 1717 (2009).

[11]U. Lourderaj and W. L. Hase, J. Phys. Chem. A **113**, 2236 (2009).

[12]B. K. Carpenter, Annu. Rev. Phys. Chem. **56**, 57 (2005).

[13]S. C. Ammal, H. Yamatake, M. Aida, and M. Dupuis, Science **299**, 1555 (2003).

[14]D. A. Singleton, C. Hang, M. J. Szymanski, M. P. Meyer, A. G. Leach, K. T. Kuwata, J. S. Chen, A. Greer, C. S. Foote, and K. N. Houk, J. Am. Chem. Soc. **125**, 1319 (2003).

[15]B. R. Ussing and D. A. Singleton, J. Am. Chem. Soc. **127**, 2888 (2005).

[16]M. Hamaguchi, M. Nakaishi, T. Nagai, T. Nakamura, and M. Abe, J. Am. Chem. Soc. **129**, 12981 (2007).

[17]M. Schmittel, C. Vavilala, and R. Jaquet, Angew. Chem. Int. Ed. **46**, 6911 (2007).

[18]A. E. Litovitz, I. Keresztes, and B. K. Carpenter, J. Am. Chem. Soc. **130**, 12085 (2008).

[19]B. K. Carpenter, Angew. Chem. Int. Ed. **37**, 3340 (1998).

[20]U. Lourderaj, K. Park, and W. L. Hase, Int. Rev. Phys. Chem. **27**, 361 (2008).

[21]A. L. Sobolewski, W. Domcke, and C. Dedonder-Lardeux, Phys. Chem. Chem. Phys. **4**, 1093 (2002).

[22]M. N. R. Ashfold, B. Cronin, A. L. Devine, R. N. Dixon, and M. G. D. Nix, Science **312**, 1637 (2006).

[23]M. N. R. Ashfold, A. L. Devine, R. N. Dixon, G. A. King, , M. G. D. Nix, and T. A. A. Oliver, PNAS **105**, 12701 (2008).

[24]M. L. Hause, Y. Yoon, A. S. Case, and F. F. Crim, J. Chem. Phys. **128**, 104307 (2008).

[25]A. Iqbal, M. S. Y. Cheung, M. G. D. Nix, and V. G. Starvos, J. Phys. Chem. A **113**, 8157 (2009).

[26]A. Bach, J. M. Hutchison, R. J. Holiday, and F. F. Crim, J. Phys. Chem. A **107**, 10490 (2003).

[27]D. R. Yarkony, Rev. Mod. Phys. **68**, 985 (1996).

[28]S. Matsika and D. R. Yarkony, J. Chem. Phys. **117**, 6907 (2002).

[29]S. Matsika and D. R. Yarkony, J. Am. Chem. Soc. **125**, 10672 (2003).

[30]S. Wilson, M. Ashfold, and R. Dixon, Chem. Phys. Lett. **222**, 457 (1994).

[31]R. Quandt, X. Wang, Z. Min, H. Kim, and R. Bersohn, J. Chem. Phys. A. **102**, 6063 (1998).

[32]I. Oref and B. S. Rabinovitch, Acc. Chem. Res. **12**, 166 (1979).

[33]J. Troe and V. G. Ushakov, J. Chem. Phys. **128**, 204307 (2008).

[34]E. Vöringer-Martinez, B. Hansmann, H. Hernandez, J. S. Francisco, J. Troe, and B. Abel, Science **315**, 497 (2007).

[35]E. P. A. Couzijn, E. Zocher, A. Bach, and P. Chen, Chem. Eur. J. , DOI:10.1002/chem.200902929 (2010).

[36]D. Townsend, S. A. Lahankar, S. K. Lee, S. D. Chambreau, A. G. Suits, X. Zhang, J. Rheinecker, L. B. Harding, and J. M. Bowman, Science **306**, 1158 (2004).

[37]P. L. Houston and S. H. Kable, PNAS **103**, 16079 (2006).

[38]B. C. Shepler, B. J. Braams, and J. M. Bowman, J. Phys. Chem. A **112**, 9344 (2008).

[39]B. R. Heazlewood, M. J. T. Jordan, S. H. Kable, T. M. Selby, D. L. Osborn, B. C. Shepler, B. J. Bramms, and J. M. Bowman, PNAS **105**, 12719 (2008).

[40]M. Toda, T. Komatsuzaki, T. Konishi, R. Berry, and S. Rice, *Geometrical Structures of Phase Space in Multidimensional Chaos: Applications to Chemical Reaction Dynamics in Complex Systems*, volume 130 of *Advances in Chemical Physics*, John Wiley & Sons, Hoboken, New Jersey, 2005.

[41]T. Uzer, C. Jaffé, J. Palacián, P. Yanguas, and S. Wiggins, Nonlinearity **15**, 957 (2002).

[42]H. Waalkens, A. Burbanks, and S. Wiggins, Phys. Rev. Lett. **95**, 084301 (2005).

[43]R. Skodje and X. Yang, Int. Rev. Phys. Chem. **23**, 253 (2004).

[44]M. Zierhut, W. Roth, and I. Fischer, J. Phys. Chem. A **108**, 8125 (2004).

[45]B. Noller and I. Fischer, J. Chem. Phys. **126**, 144302 (2007).

[46]M. Gasser, A. Bach, and P. Chen, Phys. Chem. Chem. Phys. **10**, 1133 (2008).

Acknowledgments

First and foremost I thank Prof. Peter Chen for his generous support.

I had the pleasure to interact with many talented undergraduates during the past years. I appreciated assistance both in the laboratory and for the computational work by Karla de Bruin, Didier Zurwerra, Daniel Meier, Giorgio Zambrino and Christian Seiler.

I am especially grateful for the many contributions and discussions that led to the successful completion of the work on allyl and ethyl radicals described in this work by Michael Gasser, Dr. Luca Castiglioni, Dr. Jonas M. Hostettler and Dr. Jann A. Frey.

I also enjoyed many discussions about the spectroscopy of the intermediate states of the allyl radical used in the PFI–ZEKE experiments with Prof. Frédéric Merkt and Dr. Anna M. Schulenburg.

Last but not least, I express my gratitude to René Dreier and Heinz Benz for their ideas and help in keeping the machines and electronics running in the laboratory.

The Chen group provided a most stimulating and pleasant atmosphere both at work and during numerous superbly organized group events – from skiing, hiking and cave exploring – to annual Christmas dinners and Monday Movie Nights.